2018

Fundamental Aspects Of A Novel Technology For Abatement Of Indoor Allergens

Odell Lendor Glenn Jr.
University of South Carolina

Recommended Citation

Glenn, O. L.(2018). *Fundamental Aspects Of A Novel Technology For Abatement Of Indoor Allergens.* (Doctoral dissertation). Retrieved from https://scholarcommons.sc.edu/etd/4575

FUNDAMENTAL ASPECTS OF A NOVEL TECHNOLOGY FOR ABATEMENT OF INDOOR ALLERGENS

by

Odell Lendor Glenn Jr.

Bachelor of Science
State University of New York at Stony Brook, 1991

Master of Science
New Jersey Institute of Technology, 1993

Master of Science
New Jersey Institute of Technology, 2003

Submitted in Partial Fulfillment of the Requirements

For the Degree of Doctor of Philosophy in

Chemical Engineering

College of Engineering and Computing

University of South Carolina

2018

Accepted by:

Michael A. Matthews, Major Professor

Melissa A. Moss, Committee Member

Sean R. Norman, Committee Member

Sirivatch Shimpalee, Committee Member

Mark J. Uline, Committee Member

Cheryl L. Addy, Vice Provost and Dean of the Graduate School

DEDICATION

This dissertation is dedicated to allergy sufferers, their families and caregivers. My prayers are continual for each of you.

ACKNOWLEDGMENTS

"I will instruct thee and teach thee in the way which thou shalt go: I will guide thee with mine eye." Psalms 32:8 (KJV)

I am overwhelmingly thankful to my Lord and Savior Jesus Christ for directing my career path as well as providing me with a measure of faith to keep focused on a path less taken. Words cannot express how thankful I am to have had the opportunity to embark upon research as a non-traditional graduate student while at the same time serve as primary caregiver for two aged parents and provide ministry to parishioners. Thank You for giving me the grace to persevere and to complete the process. Thank You for providing an opportunity through research to potentially touch the lives of asthma sufferers. I love what You do through me. If I had 1000 tongues, I could not thank You enough.

To my loving parents, Odell Lendor Glenn Sr., and Sara Vermae Ables-Glenn, I love you dearly. Both of you have always encouraged me in every endeavor of my life. Thank you for understanding my uniqueness and always believing in me. I sincerely thank you for entrusting me with your care in your latter years. You are both an inspiration and a joy and are loved dearly.

To my advisor, Dr. Michael A. Matthews, I am especially thankful to you for allowing me to work in your laboratory and work alongside CarboNix. It has been a wonderful experience. You have expanded my technical knowledge base in ways unimaginable through chemical, biomedical, public health, thermodynamics, fluid mechanics, biochemistry, statistics, Computational Fluid Dynamics (CFD) and ENDNOTE software which has made me a more versatile educator. As I prepare myself to teach the next generation of S.T.E.M students, skill sets gathered from research will simultaneously transfer and I hope to become a much more effective educator. I came into the department with an educational focus but left with so much more! My passion for essential oil research has only heightened itself. It has also been a pleasure serving as your teaching assistant with you for "ECHE 311" for 2 years as well as the many students I have mentored as a graduate student along the way. I am honored to have met you, your family as well as the CarboNix team. Thank you for introducing as well as allowing room for me to network with some of the top researchers in supercritical fluids and engineering education across the country.

Special thanks to Dr. Milo Koretzky. The one-year graduate experience with you has literally changed my entire perspective on teaching and learning. Our research meetings regarding education as well as conceptual exams incorporated in the class will be implemented into my classroom.

Special thanks to each of my committee members. Dr. Melissa Moss for your advice on biochemistry, assays and allergenic proteins. Thanks for personally showing up at my poster session at the AIChE meeting in 2016. It meant a lot. Dr. Mark Uline, I appreciate your mentorship and concern regarding my progress. It spoke volumes. Dr. Sean Norman, I enjoyed your graduate level course in Microbiology and your public health perspective into the research. Dr. Sirivatch Shimpalee, thank you for mentoring me and affording the opportunity to learn 4 different versions of STAR CCM+. I hope to utilize the software again in the future. Dr. Erik R. Svendsen, thank you for serving as the outside advisor on the committee. Your words of encouragement gave me hope. Special thanks to Diane Gooding (and the cats), for providing your home as a source to gather research data. A special thanks to Carol Stork for your expertise with analytical chemistry as well as being a friend in person and through social media. Special thanks to the Mass Spectrometer Center in the Department of Chemistry and Biochemistry. To Dr. Ed Gatzke, serving along with you as a Gamecock toastmaster president for two years has been amazing. My confidence as a public speaker has matured in so many ways. This group has literally inspired me to write a book on "caregiving". The radio interviews and the public speaking opportunities that I now get speaks volumes about our Gamecocks toastmaster club on campus. I have been inspired beyond words.

To Dr. Johnnie McFadden, I have truly admired your many achievements and accomplishments. Thank you for selecting me as one of the Carolina Diversity Professors Program (CDPP) scholars. Each workshop, social event, conference and opportunity to network provided a springboard upon which to cultivate my career. Thank you for providing opportunities and funding to complete my degree. It was indeed an honor to serve as the community outreach representative for the last 2 years of my tenure as a graduate student.

To. Dr. Wayne Carver, thank you for providing funding from the South Carolina INBRE grant. Each conference that I attended was well worth the trip. Thank you for consistently checking up on me to track progress during the journey.

To Dr. Lauren Clark, thank you for providing opportunities for me to serve at local colleges, speak on panel discussions and to guide me along the process as a SPARC fellowship recipient. Our lunches during semesters were enlightening. Thank you also for your friendship.

To Dr. John Weidner, Dr. Jed Lyons, Dr. Jamil Khan and Dr. Mohammad Hailat, special thanks to each of you all for your guidance, networks, and mentorship towards becoming an instructor at The University of South Carolina with future aspirations in engineering education research. Thank you all for providing me the opportunity to teach undergraduate courses during my last year of graduate school with anticipated employment afterwards. Special thanks to the entire staff in the department of chemical engineering at the university and all of your support.

Special thanks to additional funding provided by The National Institute of Health (NIH), The Alfred P. Sloan Foundation Fellowship and the GEM Fellowship. I am grateful and honored to have been funded through these national organizations as well as the SPARC grant from the university. Special thanks also to STAR CCM+ version 9.06.011 for extended licensing service provided by CD-Adapco. Special thanks to Indoor Biotechnologies, in Charlottesville, Virginia for MARIA analysis.

Last, but certainly not least, special thanks family, friends, churches, non-profit organizations, social media friends and acquaintances for words of encouragements and/or congratulations. I am sincerely thankful for each one of you.

ABSTRACT

The overall goal of this research was to develop a novel approach to reduce the potency of certain asthma triggers, namely, proteins produced by pests or pets in indoor environments. The broad hypothesis of the research was that naturally occurring essential oils will demonstrate enhanced denaturing ability. In any indoor environment, allergens are bound to dry dust particles. In this work, the effectiveness of using dry ice and CO$_2$ with potential for essential oils on dry allergenic proteins through CFD modeling and ELISA methods were evaluated.

There are three objectives central to this work. The first objective was to apply engineering principles through computational fluid dynamic (CFD) modeling on a Coanda spray nozzle. A Coanda nozzle can be used to produce a high velocity mixture of air, gaseous CO$_2$, and dry ice particles from a supply of liquid CO$_2$. Such a process is effective (for instance) for residue-free rapid cooling or precision cleaning. A thermodynamic and computational fluid dynamics analysis of this flow is presented for the purposes of optimizing and modeling the process parameters, which includes the temperature of the liquid CO$_2$ supply, the flow rate, and the pressure, nozzle, and air configurations. The proposed design will result in a new intervention strategy for asthma sufferers and their doctors, in the form of a home allergen abatement service. The allergen abatement process is based on current technology. The abatement uses a concurrent spray nozzle composed of both air and dry ice (carbon dioxide). The nozzle that forms the air/dry ice spray is

mounted inside a specially-designed vacuum clear head, which instantly collects both the dislodged particles as well as the CO_2 as it sublimes from solid to gas. Upon vacuuming via the concurrent spray of air and dry ice, higher levels of dust are dislodged over conventional vacuuming. The research presented in this dissertation employs CFD simulations that model the spray geometry and process characteristics of a Coanda nozzle. The CFD model generates microscopic details of the fluid including the velocity, direction, flow rate, pressure, nozzle diameter and temperature as a function of air and CO_2.

The second objective was to determine solubility data over a range of temperature and density for the most dominant components in three essential oils as a function of temperature and density in both liquid and supercritical $CO_{2.}$ As a continuation from the first objective, we employed essential oils within the “dry-clean” process to prevent re-infestation. We have every reason to believe that essential oils and CO_2 are soluble to do them being nonpolar however, there are some data suggesting that the solubility of the most abundant component of essential oils in supercritical $CO_{2,}$ there are no known data available on the solubility of the most abundant component in tea tree oil, cedar wood oil and hinoki oil at temperature ranges from 25°C to 60°C and density ranges from 0.2 g/mL to 0.7 g/mL. These oils are each a mixture of several chemical species, which greatly complicates the measurement of solubility. To address this, gas chromatography/mass spectrometry were employed to identify the major component on each oil.

The last objective of this work tested an essential oil’s ability to inactivate allergenic proteins on two well-known indoor allergens, *Fel d 1* (cat) and *Der f 1* (dust mite). This research addresses whether essential oils alone are able to deactivate the proteins on dry dust and quantifies it in µg of allergen per total grams of dry house dust.

Mutliplex Array for Indoor Allergens (MARIA) is the primary analytical tool for evaluating the activity on each protein.

TABLE OF CONTENTS

LIST OF TABLES

LIST OF FIGURES

LIST OF SYMBOLS

A_p	Projected area of a particle
C	Concentration = $\frac{\boldsymbol{M_i}}{\boldsymbol{V}} = \frac{\boldsymbol{mf_iM}}{\boldsymbol{V}} = \boldsymbol{mf_i\rho}$
C_{am}	Virtual mass coefficient
C_D	Standard drag coefficient for spherical particles
$C_{1\epsilon}$	1.44 (k-ε model constant)
$C_{2\epsilon}$	1.92 (k-ε model constant)
Cμ	0.09 (k-ε model constant)
$\boldsymbol{\bar{c}_p}$	mean constant-pressure specific heat at temperature T
$\boldsymbol{c_p^o}$	reference specific heat at temperature T_o
P	density
ρ_s	density of the solid state
ρ_v	density of the vapor state
D	Hydraulic Diameterm
d_p	Particle Diameterum
D_{im}	Molecular diffusivity
$\boldsymbol{\nabla}$	Partial derivative of quantity with respect to all directions
$\boldsymbol{\nabla}$p	Pressure gradient in the carrier fluid
ϵ	turbulent dissipation rate

E	Energy kJ
F_b	Resultant of body forces N
F_d	Drag Force N
F_g	Gravitational Force N
$F_{h,I}$	Diffusional thermal energy flux N
F_p	Pressure gradient forceN
F_{vm}	Virtual mass force N
f	Darcy friction factor
g	Gravitation acceleration vector m/s^2
h	thermal enthalpy
h_t	thermal enthalpy
H_1	Enthalpy at the inlet stream kJ/kg
H_2	Enthalpy at the outlet stream kJ/kg
$\mathbf{H_2^{vapor}}$	Enthalpy of vapor at the outlet kJ/kg
$\mathbf{H_2^{dry\ ice}}$	Enthalpy of dry ice at the outlet kJ/kg
J_j	Diffusion heat flux W/m˚C
k	turbulent kinetic energy
L	Length of tube m
m	mixture of CO_2 and air gas phase
$\dot{\mathbf{m}}$	Mass flow rate kg/s
M	total mass of the mixture
M_i	mass of each constituent of the mixture
m_f	Mass of flow kg

m_p	Mass of particle kg
mf_m	Ratio of the mass of species *m* to the total mass of the mixture
M_i	Inter-phase momentum exchange per unit volume
p	Hydrostatic pressure
P_1	Initial Pressure MPa
P_2	Final Pressure MPa
$P_{saturation}$	CO_2 Saturation Pressure MPa
ΔP	Pressure drop MPa
Re	Reynolds number
Re_p	Particle Reynolds number
s_m	Mass source
S_m	Rate of mass production or consumption
r	Radius of particle m
t	times
T	temperature
T_1	Inlet Temperature K
T_o	Initial Temperature K
T_w	Wall temperature K
μ	Molecular dynmaic viscosity
$\boldsymbol{\mu_t}$	Turbulent viscosity
V	Velocity gradient 1/s
v	Mean flow velocity m/s
v_1	Velocity at the inlet m/s

v_2	Velocity at the outlet m/s
υ	kinematic viscosity
x_2	Mass fraction of CO_2 vapor
$1-x_2$	Mass fraction of dry ice
V_d	Droplet velocity
v_s	Particle slip velocity
y^+	normal distance from the wall to the wall-cell centroid

LIST OF ABBREVIATIONS

CFD	Computational Fluid Dynamics
DERP 1	Dermatophagoides pteronyssinus 1
ELISA	Enyzme-Linked Immunosorbent Assay
FELD 1	Felis Domesticus 1
IgE	Immunoglobin
MARIA	Multiplex Array for Indoor Allergens
PR-EOS	Peng-Robinson Equation of State
RANS	Reynolds-Averaged Navier-Stokes
RTD	Residence Time Distribution
SFX	Supercritical Fluid Extractor
TDE	Turbulence Energy Dissipation
TKE	Turbulence Kinetic Energy

CHAPTER 1: INTRODUCTION

1.1 ASTHMA STATISTICS

Every day in America, 44,000 people experience an asthma attack and 9 die. More than fifty million Americans suffer from allergies, making this the sixth leading cause of chronic disease in the United States. The percentage of individuals with asthma in the United States is currently 8.2% which has been steadily on the rise until a recent leveling off in the past decade (1). Currently the prevalence of doctor-diagnosed childhood asthma in the United States is approximately 7% (2). Children living in poor neighborhoods bear the highest burden of disease and are four times more likely to be hospitalized for asthma as children who live in wealthy neighborhoods.

Additionally, asthma is a health disparity problem. Asthma is slightly more prevalent amongst African Americans than Caucasians. African Americans are three times more likely to die from asthma (3) and African American women have the highest asthma mortality rate of all groups, more than 2.5 times higher than Caucasian women (3). The current prevalence of doctor-diagnosed childhood asthma in the United States is estimated at 7% with African American children having a slightly higher national prevalence of 8% (4). However, in New York City 17% of children experience asthma like symptoms at some point in their lives (4). The cost of asthma in 2007 was estimated to reach $19.7 billion ($14.7 billion direct, $5 billion indirect) with the single largest cost being for medications.

The National Survey of Lead and Allergens in Housing, conducted by the National Institute of Environmental Health Sciences (NIEHS) and the US Department of Housing and Urban Development revealed that 84% of US homes have detectable levels of mite allergens, half have levels sufficient to trigger allergic reactions, and a quarter have high enough allergen levels to trigger asthma attacks (5). The highest levels of mite allergens are found in bedding and carpets (6).

Asthma can be trigged by numerous factors. Of specific interest for this research is the inhalation of bioaerosols. Bioaerosols are biological triggers which include allergenic proteins found in airborne household dust. Bioaerosols first accumulate, and then are released from indoor reservoirs such as carpets and bedding. Common indoor allergen generators include dust mites, cockroaches, pets, and pests such as rodents. Data from the National Survey of Lead and Allergens in Homes (6) show that over 50% of homes have detectable levels of at least six indoor allergens, and nearly 46% had three allergens at levels capable of triggering asthma.

1.2 CAUSES OF AN ASTHMA ATTACK

Asthma is a common chronic disorder of the lung airways that involves a complex interaction of airflow obstruction, bronchial hyper responsiveness and underlying inflammation. This interaction can be highly variable among and within patients over time (7). An asthma attack occurs when airways in the lung become swollen and inflamed. The muscles around the airways contract, causing the bronchial tubes to narrow. During an asthma attack, individuals cough, wheeze and have trouble breathing. An asthma attack may be minor or a life-threatening emergency.

Dust mite allergen, *Dermatophagoides pteronyssinus group 1*(*Der p 1*) and cat allergen *Felis domesticus allergen 1* (*Fel d 1*) are two common indoor allergenic proteins. In some individuals, asthma can be triggered by medications, such as aspirin and other non-steroid anti-inflammatory drugs. Urbanization has also been associated with an increase in asthma incidence, however the exact nature of this relationship is unclear (8).

Once the human body detects an allergen as foreign, it initiates a cascade of events which stimulate several types of immune cells. T cells, activated by antigen presenting cells, rapidly stimulate B cells. These B cells transform into plasma cells which produce Immunoglobin (IgE) antibodies specific to the allergen. Finally, the allergenic proteins invoke an excessive activation of certain white blood cells called mast cells and basophils by IgE. The IgE antibodies bind to these mast cells. At this point, the allergen has triggered the immune response cascade (7). This reaction results in an inflammatory response that can range from uncomfortable to dangerous in humans. Common allergic reactions include asthma attacks, eczema, hives, hay fever and food allergies.

1.3 ASTHMA PREVENTION

Common methods of allergy prevention include reducing the allergen load in the home environment. This includes vacuuming, cleaning surfaces, denaturing allergens via chemical sprays, such as tannic acid, and laundering with hot water detergents. Recent research evaluated the optimal conditions of mechanical laundry for the removal of house dust mites. Four washing modes were compared 30°C, 40°C, 60°C and steam water (SW) with detergent. Allergen removal performance was assayed using an Enzyme-linked immunosorbent assay (ELISA). The 30°C and 40°C washing modes were only 6.5% and 9.6% successful at killing *Dermatophagoides farina* (*Der f 1*). However, using the 60°C and SW washing modes, nearly all house dust mites were killed. The amounts of *Der f 1* remaining after the 30°C, 40°C, 60°C, and steam washing modes were 26.8%, 2.4%, 1.3%, and 0.6%, respectively (9). As the temperature of the wash mode increased the level of allergen deactivation increased as well.

1.4 ROLE AND STRUCTURE OF ALLERGENIC PROTEINS THAT TRIGGER ASTHMA

1.4.1 *FELIS DOMESTICUS D 1* ALLERGEN

Domestic cats (*Felis domesticus)* are a popular pet in United Stated homes. 99.9% of homes have measurable levels of cat allergens, even though only 49.1% of homes have either a dog or a cat (6). Nevertheless, cat allergens are one of the major triggers of asthma worldwide. Cat allergens are adhesive so that they stick to clothes and very small particles of these allergens can become aerosolized. The highest levels of cat allergens are found in living rooms (10).

The dominant cat allergen, *Fel d 1*, is produced largely in cat saliva and sebaceous glands (11). This protein is of an unknown function in the animal, but causes an IgG or IgE reaction in sensitive humans. A cartoon of the *Fel d 1* protein is shown in Figure 1.1. *Fel d 1* is composed of eight α-helices. *Fel d 1* is a four subunit tetramer composed of two 18 kDa heterodimers (10), which have a similar three-dimensional structure. A dimer is a complex of two macromolecules and a hetero-dimer is formed when two dimers bond.. The *Fel d 1* heterodimers are disulfide-linked. The structure of *Fel d 1* is remarkably similar to that of uteroglobin, a molecule with anti-inflammatory properties found in humans.

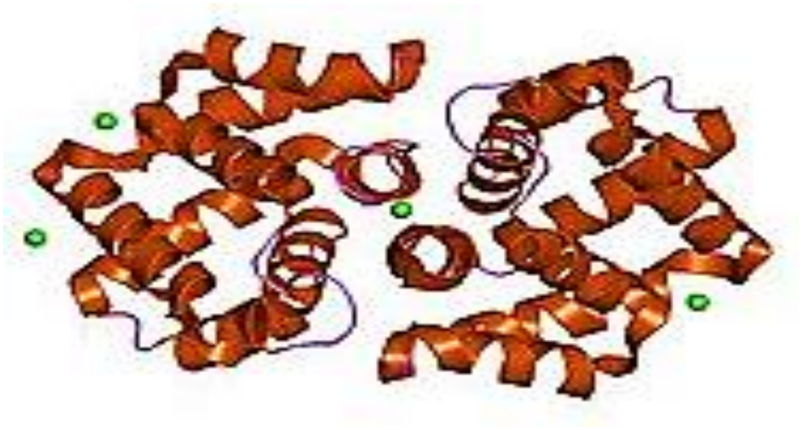

Figure 1.1: **Structural characterization of the cat allergen, *Felis domesticus 1* tetramer (10)**

1.4.2 *DERMATOPHAGOIDES PTERONYSSINUS GROUP 1* ALLERGEN

Dermatophagoides pteronyssinus group 1 is a potent allergen derived from dust mites. Dust mites are ubiquitous in most humid and warm areas and are often found in bedding or underneath carpeted floors. Exposure to dust mite allergens is a known risk factor which may trigger an asthma attack (11). Dust mites range in size from 0.3 to 0.4 mm. Dust mites do not bite, allergenic exposure occurs through contact with the allergenic proteins in the mite feces and corpses (12).

The density and species prevalence of dust mites (13) was determined at various times over a 5-year-period in 252 homes of dust mite sensitive asthma patients living in eight geographic areas of the United States (Cincinnati, Ohio; New Orleans, La.; Memphis, Tenn.; Galveston, Texas; Greenville, N.C.; Delray Beach, Fla.; San Diego and Los Angeles, Calif.). The most common dust mites found in the homes were *Dermatophagoides farinae* (*Der f 1*), *Dermatophagoides pteronyssinus* (*Der p 1*), *Euroglyphus maynei* (EM), and *Blomia tropicalis*. All homes studied contained *Dermatophagoides* mites, but few homes were populated exclusively by either *Der f 1* or *Der p 1* alone. Most homes (81.7%)

were cohabitated by both *Der f 1* and *Der p 1*. In cohabited homes, one species was predominant and usually made up at least 75% of the total mite population. Prevalence of species varied between homes within a geographic area. EM occurred in significant numbers in 35.7% of homes in New Orleans, Memphis, Galveston, Delray Beach, and San Diego. *Blomia tropicalis* occurred in the same cities but in low densities. For all dust samples, only 13 homes of the 252 sampled had 100 or fewer mites/gm dust, which is considered to be the threshold for sensitivity. Most homes had average mite densities of 500 or more mites/gm dust. The results of the study suggest a significant and widespread occurrence of both *Der f 1* and *Der p 1* (13).

The allergen most prevalent in mite feces is *Der 1* (*Der f 1*+*Der p 1*). This class of allergens are unstable in heat and denatures easily. The role of *Der 1* in mites is thought to be that of a digestive enzyme, called cysteine protease. *Der p 1* (Figure 1.2) has a molecular weight of 25 kDa. The proteolytic activity of *Der p 1* has been proposed to enhance the capacity of the molecule to sensitize humans (14). Its secondary structure is a combination of both α-helices and β-sheets.

Figure 1.2: **Structure of *Der p 1* allergen. Combination of both alpha helices and β-sheets (14)**

Der 2 (*Der f 2* + *Der p 2*) is an allergen that is prevalent in the corpses of mites. It has a molecular weight of 14 kDa and is relatively stable in heat. The role of *Der f 2* is not known (12). Most of the studies that have been done in the US report mite allergens results as *belonging to the Der 1* family (*Der p 1* + *Der f 1*), there is not much information to date comparing the two groups.

1.5 STRUCTURAL CHARACTERIZATION OF PROTEINS

There are four levels of protein structure, as illustrated in Figure 1.3. The primary structure is a linear sequence of amino acids that is comprised of one polypeptide chain. The secondary protein structure arises when the amino acids of the polypeptide chain are linked by hydrogen bonds between the carbonyl oxygen and the amide hydrogen of the peptide bond. This bonding generates specific structures in the primary chain, α-helices or β-pleated sheets (15). α-helices are rod-shaped peptide chains coiled to form a helix structure and β-pleated sheets are two peptide strands aligned in the same direction or opposite directions stabilized by hydrogen bonds.

Tertiary protein structure is the three-dimensional arrangement of the amino acids in a polypeptide chain. This structure is usually the active, conformation and is held together by multiple noncovalent bonds (15). Quaternary structure is an arrangement of multiple folded protein or coiling protein molecules in a multi-subunit complex. It is the next level of complexity from the tertiary structure. Quaternary structure is the combination of two or more chains, to form a complete unit. The interactions between the chains are not different from those in tertiary structure, but are distinguished only by being interchain rather than intrachain (15).

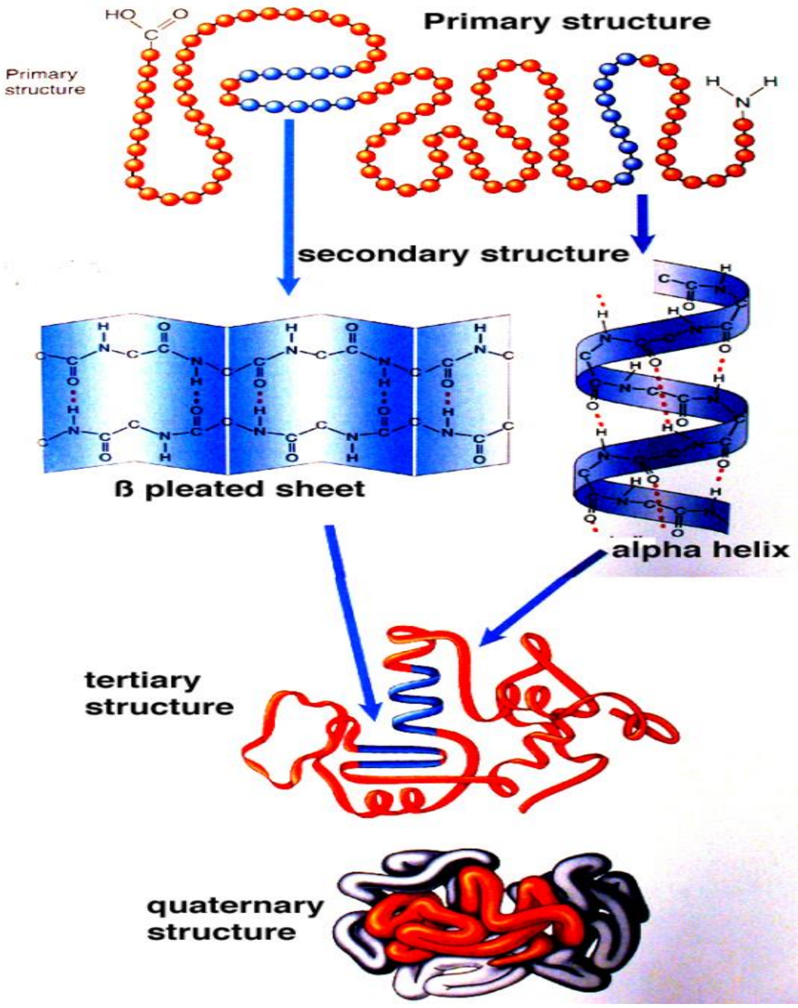

Figure 1.3: **Structure Characterization of Proteins (15)**

1.6 ESSENTIAL OILS

1.6.1 SOURCES AND CHARACTERISTICS

Essential oils are volatile, natural, complex compounds characterized by a strong odor and formed by aromatic plants as secondary metabolites (16). There are several methods for extracting essential oils. These may include the use of liquid carbon dioxide, microwaves, or low or high pressure distillation via boiling water or hot steam (16). Essential oils are known for their potent fragrance as well as their antiseptic, bactericidal, viricidal, fungicidal, and medicinal properties. They are used in embalmment, preservation of foods, and as antimicrobial, analgesic, sedative, anti-inflammatory, spasmolytic and locally anesthetic remedies (16). In nature, essential oils play a crucial role in the protection of the plants as anti-bacterial, antivirals, antifungals, insecticides and as protection against herbivores by reducing their appetite for such plants. They also may attract some insects to favor the dispersion of pollens and seeds(16).

Essential oils are very complex natural mixtures. They are characterized by two or three major components at fairly high concentrations (20–70%) while other components may be present in trace amounts. Generally, the major components are found to reflect the biophysical and biological features of the essential oils. The main group is composed of terpenes and terpenoids while secondary components are more aromatic and aliphatic constituents. All components are characterized by low molecular weight. The components include two groups of distinct biosynthetic origin (16).

The mechanism of action of essential oils *in vivo* is still not well characterized (17). Scientific literature supporting the efficacy of herbal therapies is still incomplete. There are few well-controlled studies that support the efficacy of herbal therapies in the treatment and clinical improvement of patients with asthma. Available scientific evidence has not yet confirmed the validity of essential oil use in the treatment of asthma (18). There is, however, some evidence that essential oils may act as in an antimicrobial or antioxidant manner or have a pharmacological effect on various tissue (17). McDonald and Tovey reported that several essential oils could be emulsified in low concentrations using Tween to form effective acaricides. However, Tween detergent is not available to the general public (19). In a follow-up study, Tovey and McDonald showed it possible to make a simple, effective, inexpensive laundry acaricidal wash that simplifies the process using hot water. This simple formula allows for maintenance of low allergen levels in bedding for longer than normal laundering alone (20). Combining eucalyptus oil, a widely available essential oil, with a specific kitchen detergent concentrate can create an inexpensive acaricidal wash. They also demonstrated the ability of this was to reduce the recovery of live mites found in blankets by more than 95% during normal machine washing.

1.6.2 TEA TREE OIL

Tea tree oil is the essential oil that is steam distilled from the Australian native plant, Melaleuca alternifolia (21). Gas chromatography has identified one hundred twenty-nine components (22). Terpinen-4-ol is responsible for majority of tea tree oil's antimicrobial activity (21). Tea tree oil is composed primarily of the following terpene hydrocarbons, mono-terpenes, sesquiterpenes and their associated alcohols. Terpenes are volatile, aromatic hydrocarbons that may be considered polymers of isoprene, C_5H_8. Tea tree oil has a relative density of 0.885 to 0.906 g/mL is only slightly soluble in water, and is miscible with nonpolar solvents (23).

Tea tree oil is commonly used in Australia as a topical therapeutic agent (24). The medicinal uses of tea tree oil relate primarily to its anti-inflammatory and antimicrobial properties. The use of tea tree oil as a topical antimicrobial agent is supported by a growing body of clinical data indicating that it is effective in treatment of infections or medical conditions such as herpes labialis, acne, and tinea, as well as in the clearance of methicillin-resistant *Staphylococcus auereus* (24).

In a recent study (21), Tranchida, et al examined the anti-inflammatory properties of tea tree oil using an *in vitro* assay where human peripheral blood monocytes (PBMCs) were used as a model for tissue macrophages. Upon activation with differentiating molecules, such as LPS, PBMCs will derived towards a macrophage lineage. Upon differentiation these cells produce many mediators of inflammation including , TNFα and IL-1β. Other important monocyte/macrophage derived mediators of inflammation include IL-8, IL-10 and PGE_2. These molecules, and others generated in an inflammatory response cascade, can damage tissue or activate other cells to produce further downstream pro-inflammatory mediators (21). Tea tree oil was shown to function as an anti-inflammatory agent that reduced the production of TNFα, IL-1β, IL-8, IL-10 and PGE_2 by LPS-activated monocytes. At concentrations equivalent to 0.125% tea tree oil significantly suppressed LPS-induced production of TNFα, IL-1β and IL-10 by approximately 50% and PGE_2 by approximately 30% after 40 hours (21).

1.6.3 CEDAR WOOD OIL

The type of cedar wood essential oil used in this study is extracted from the Eastern red cedar (ERC), also known as the *Juniperus virginiana L.* Other cedar trees which produce the essential oil include the Western Juniper *(Juniperus occidentalis Hook)* and Ashe Juniper *(Juniperus ashei)* (25). *Juniperus virginiana L*. is the most widely distributed in the Northern Hemisphere and has about 68 species throughout the world. The leaves, berries, and essential oils from *Juniperus* species are used for cosmetic and medicinal purposes. In traditional medicine, the coniferous parts and leaves of *Juniperus* are utilized as antihelmintic, diuretic, stimulant, antiseptic, carminative, stomachic, antirheumatic, and antifungal agents. These derivatives are also used for wound healing. Juniper essential oils are composed monoterpenes, sesquiterpenes, and other volatile compounds (25).

One recent study (25) assessed the wound healing and anti-inflammatory potential of sub extracts of essential oils obtained from the Eastern Red Cedar, Western Juniper and Ashe Juniper on male Sprague-Dawley rats and Swiss albino mice. A circular wound was created and left open on the dorsal interscapular region of each animal by excising the skin with a 5-mm biopsy punch. Test samples, the reference drug, Madecassol, and essential oil ointments were applied topically, daily, until the wound was completely healed. Progressive changes in the wound area were monitored by a camera (Fuji, S20Pro) every other day. The essential oil of *J. occidentalis* showed the highest activity on the *in vivo* biological activity models. Additionally, the oil of *J. virginiana* was found highly effective as an anti-inflammatory compound. The experimental data demonstrated that essential oil of *J. occidentalis* displayed significant wound-healing and anti-inflammatory activities (25).

1.6.4 HINOKI OIL

The *Chamaecyparis obtusa,* or hinoki cypress, is a conifer of the cypress family (Cupressaceae), and it is rich in a variety of active pharmaceutical ingredients such as flavonoids and other essential components (26). It is planted widely in western parts of Japan, (26) and has shown to have both antifungal and insecticide activities (26). *Chamaecyparis obtusa* is also native to Northeast Asia. The oil extracted from the leaves and twigs of *C. obtuse* have been commercially used as a functional additive in the production of soap, toothpaste and cosmetics due to its strong fragrance. The essential oil derived from the *C. obtuse* leaf has an antimicrobial activity against various fungal pathogens and pathogenic bacteria as well as allelopathic and insecticidal properties (26).

1.7 PATENTS AND OTHER RESEARCH ON ESSENTIAL OILS

As a basis for the work proposed in this dissertation, a patent has been published that supports evidence that cedar wood oil and hinoki oil are of potential value in deactivating some allergens. Hinoki oil and cedar wood essential oils are used against one or both of *Der p 1* and *Der f 1* allergens (27).

Priestley et al, 1998 used three essential oils (tea tree oil, lavender oil and lemon oil) to study the effect of the oils inducing immobility and mortality on the house dust mite. The sides and bottom of a 9cm petri dish were covered with 3 layers of masking tape. A 3 mm layer of mite colony/substrate mixture was added to the dish. The mixture included finely ground desiccated liver and brewer's yeast as mite food (28). Due to the fact that dust mites are extremely small and highly mobile, mite food was given to encourage the mites to be mobile and easy to observe. The dish was then sealed and incubated at 25°C and 75% relative humidity. To expose the mites to the essential oils, a 3 cm diameter portion of filter paper was suspended in the center of a short length of plastic tubing. The filter paper was then saturated with 0.1 mL of one of the three oils at 10% v/v concentrations in ethanol. All papers were then allowed to dry for 5 minutes (28).

Figure 1.4 shows the chamber used for testing acaricidal activity. Ten dust mites were removed from the colony and placed on the test papers. At 30 minutes, the mites were observed for mobility and at 2 hours for mortality with forceps. Each experiment was replicated three times. Tea tree oil was the most effective acaricide causing 100% immobility at 30 minutes and 100% mortality at 2 hours. Lavender oil was acaricidial to a lesser extent, giving 87% immobility at 30 minutes and 87% mortality at 2 hours. Lemon oil gave 63% immobility at 30 minutes and 80% mobility at 2 hours. The control condition with no essential oil added showed 0% immobility at 30 minutes and 0% mortality at 2 hours (28).

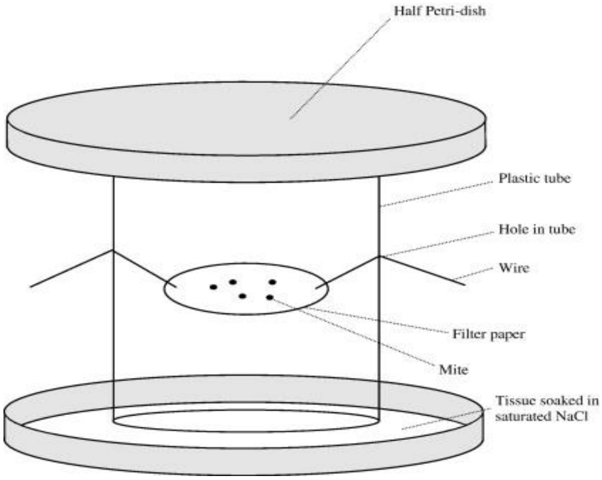

Figure 1.4: **A mite-chamber for testing acaricidal (29)**

Another recent study (30) investigated the anti-inflammatory effect of fingered citron essential oil (*FCEO*) in *LPS*-stimulated mouse macrophage (*RAW 264.7*) cells. Fingered citron oil originates in India and has been used worldwide. Its peel, leaves and root have been used as folk medicine for the treatment of stomach ache, edema, headache, rheumatism, infectious hepatitis and arthritis (30). Fingered citron has been reported to possess anti-oxidant, anti-inflammatory and anti-microbial activities. The *RAW 264.7* cells were cultured in Dulbecco's modified Eagle's medium (DMEM) and treated with *LPS* to generate a pro-inflammatory status. The cells were incubated in an atmosphere of 5% CO_2 at 37°C and were sub cultured every 3 days. *FCEO* was diluted with DMEM prior to treatment. The inhibitory effect of *FCEO* on the production of pro-inflammatory cytokines (*IL-1β, IL-6 and TNF-α*) from *LPS* treated *RAW 264.7* cells was determined using a mouse enzyme-linked immunosorbent assay (ELISA) kit (30). These three cytokines are known to act as pro-inflammatory mediators both *in vitro* and *in vivo*. The results (Table 1.1) reveal that *LPS* stimulation significantly increases levels of pro-inflammatory cytokines in the culture media of *RAW 264.7* cells. However, cytokine levels were significantly decreased by pre-treatment of *RAW* cells with *FCEO*. The cytokine levels decreased with increased levels of *FCEO* treatment (30).

Table 1.1: **Inhibitory effect of *FCEO* on the pro-inflammatory cytokine production in RAW 264.7 cells**

Cytokine	**LPS treated cells with no FCEO**	**LPS treated cells with 0.005% FCEO**	**LPS treated cells with 0.01% FCEO**	**LPS treated cells with 0.02% FCEO**
TNF-α	100%	60%	45%	40%
IL-6	100%	65%	40%	15%
IL-β	100%	60%	35%	30%

CHAPTER 2: MULTI-PHASE MATHEMATICAL MODELING OF COMPRESSED CO2 EXPANSION THROUGH A COANDA NOZZLE

2.1 MOTIVATION

The motivation behind this work is based from a project provided by a university-based startup company called “Carbonix” funded by the National Institute of Health (NIH) through a Small Business Innovation Research (SBIR) grant and founded by advisors, Dr. Michael Matthews and Mr. Allan Quick. The technology described below removes particulate matter from textile surfaces in an indoor environment. These particles contain biological triggers that cause asthma. The technology utilizes a concurrent spray of dry ice particles with air, produced through a Coanda nozzle.

This technology, known as the “CarboNix Triple Phase Process” comes from patented research at the University of South Carolina. Carbonix applies its patented technology for allergy abatement to home owners, office buildings, public housing and other public spaces. The technology addresses the use of compressed carbon dioxide for deactivating and removing allergenic proteins that trigger asthma.

The equipment and materials are incorporated on a CarboNix truck, as shown in Figure 2.1 that service a home for eradication of allergens from carpets and bedding in homes. As shown in Figure 2.1, liquid CO_2 is supplied at 904.7 psia via the black hose, while the red hose is for air. The green hose is for vacuum.

Figure 2.1:**CarboNix truck**

A continual flow of compressed carbon dioxide to a Coanda nozzle is used to produce dry ice and a high velocity gas stream. The cold temperature kills dust mites and the high velocity gas dislodges particulates that contain the allergens from carpets and beds in a home. This approach is both clean and dry. Figure 2.1 shows a schematic of the CO_2 on board the van which then enters a Coanda nozzle as liquid CO_2. The liquid then thermodynamically exits as a mixture of dry ice and gaseous CO_2. Compressed air also flows through the nozzle providing added velocity via the “Coanda effect”. The Conada effect is when, similar to the wings of an airplane, the air moves along the contour of the Coanda nozzle. A jet of air accelerates around the nozzle and then mixes with the CO_2. This propels the dry ice deep into a carpet or mattress. The dry ice impacts the surface and then sublimes in a matter of minutes, producing the very cold temperatures necessary to freeze the dust mites.

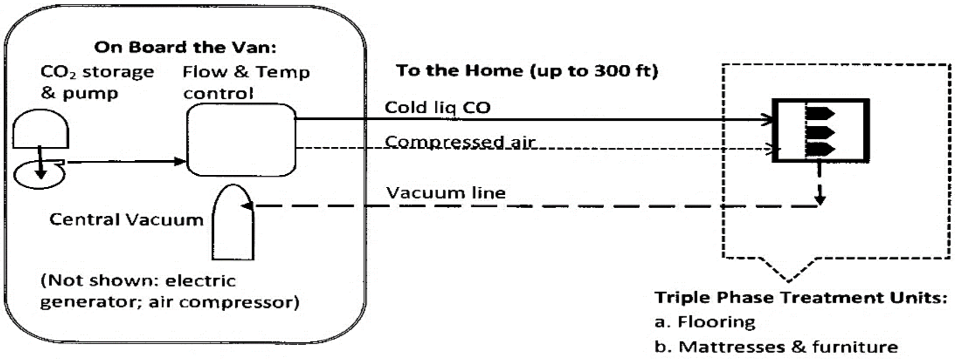

Figure 2.2: **Technology for Allergen Abatement**

This research project specifically focuses on the Coanda nozzle. A capillary tube extends through, and just beyond, the tip of the nozzle. Liquid CO_2 expands rapidly at the tip to 1.01 MPa (nominally 1 standard atmosphere pressure (atm)), producing a two-phase flow of dry ice particles mixed with gaseous CO_2. The high velocity air accelerates the two-phase CO_2 stream, producing a cold jet of gas and particles. The two-phase solid/gas mixture state is a consequence of the thermodynamics of the CO_2 phase diagram (31). At 1atm solid and gas can only coexist at the sublimation temperature of -77^{o}C while the liquid state is not possible, as shown on the CO_2 phase diagram in Figure 2.3.

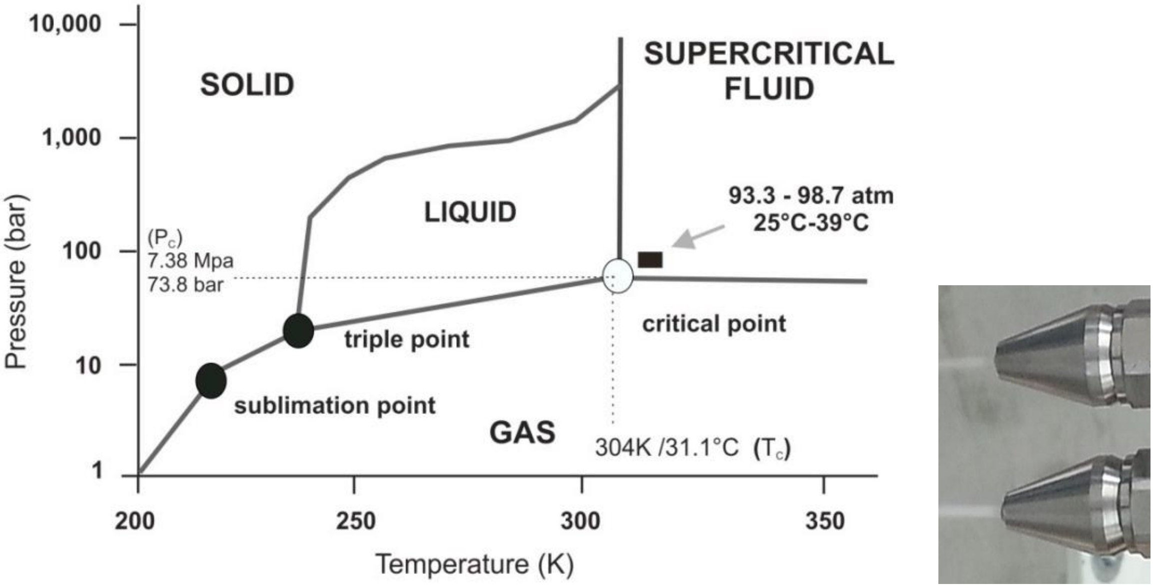

Figure 2.3: **CO_2 Phase Diagram (4) with Coanda spray nozzle**

At the outlet state, only solid and gas can exist. The goal is to have the CO_2 as cold as possible so as to form as much dry ice is possible. The first research question pursued in this work was to query what CO_2 supply temperature was needed to produce a given amount of dry ice from the nozzle. In order to determine the amount of dry ice which could be produced, an energy balance was done on the Coanda nozzle. Shown in Figure 2.4 on the left are process variables for generating subcooled liquid CO_2. Everything for this experiment was fixed except the inlet temperature, T. A constant mass flow rate of 10 lbm/s was used in this work. At the outlet, the temperature and pressure are the sublimation state as shown on the CO_2 phase diagram (Figure 2.3), at -78.5 C and 1 atm. *1-x2* represents the mass fraction of dry ice and *x2* represents the mass fraction of vapor.

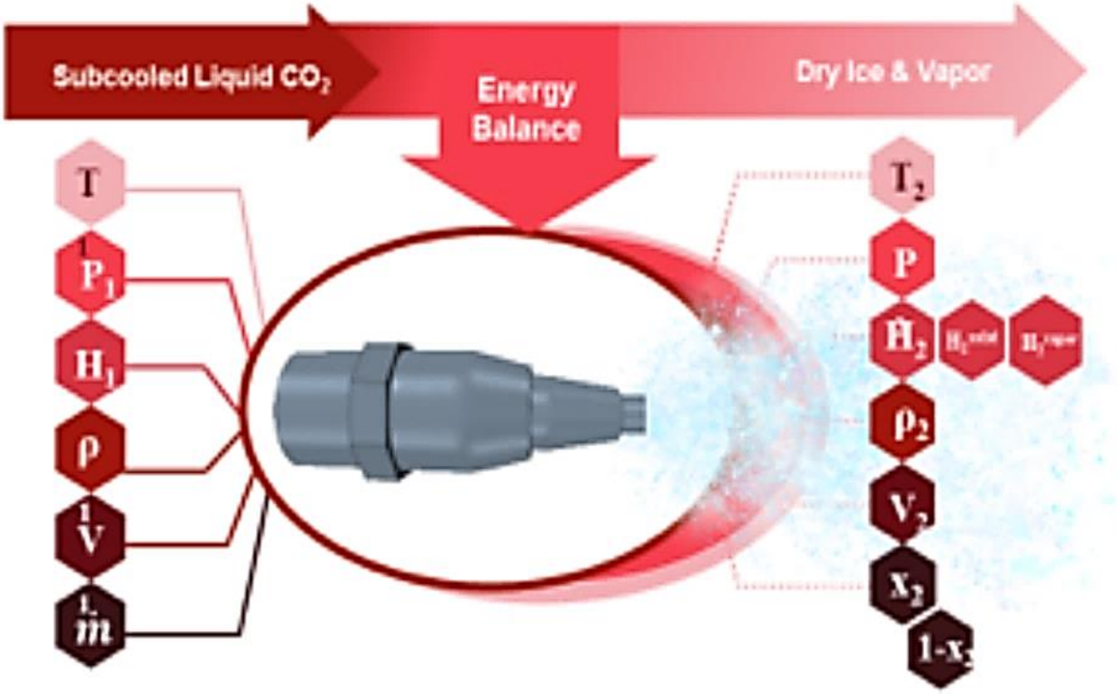

Figure 2.4: **Coanda Nozzle and Operating Conditions**

The mass fraction of dry ice, ($1-x_2$) and the outlet velocity (v_2) were determined using the energy balance equation. These values were then used as inputs into the computational fluid dynamics (CFD) simulation which led us to the two other research questions pursued in this work. An open and closed nozzle boundary were simulated via CFD. Temperature, pressure, mass fraction of air and CO_2 vapor, dry ice particles, and disperse angle characteristics were observed. In addition, the fluid dynamics of the dry ice particles in turbulent flow were recorded. The CFD simulations were used as a tool to improve the overall freeze spray operation for CarboNix.

2.2 LITERATURE REVIEW ON CFD MODELING

Computational Fluid Dynamics (CFD) is a well-known field in fluid science that uses mathematical models and powerful 3-D computer simulation to predict the properties of fluid flow. The Navies-Stoke equation, mass conservation law and equation of state are the building blocks of the mathematical models used in CFD simulation (32). The finite volume method and finite differences scheme are used in the CFD simulation for transforming differential equations into a set of linear equations. This is done to provide an improved understanding, both qualitatively and quantitatively, of physical phenomena present in diverse flow systems. An efficient iterative linear equation solver is used for the solution (33). Using CFD, a computational model can be built to represent a system or device being studied. In-built numerical models are employed for the representation of flow physics and related phenomenon. Boundary conditions at the inlet and outlet are required for the simulation. The simulations predict flow dynamics and related phenomenon for the entire computational domain (34).

The objective of this work was to analyze a novel process that utilizes a high velocity stream of air, produced in a modified Coanda nozzle, to accelerate a flow of dry ice particles. The modified nozzle creates a stream of dry ice powder that is directed onto a substrate for the purpose of rapid and dry cooling and cleaning. This "CO_2 spray cooling" process quickly decreases the substrate temperature to -30°C or lower. The dimensions of the non-adjustable Coanda nozzle is shown in Figure 2.5. One application of such a process is as a means for achieving precision cleaning without the use of liquid solvents (35). Another application is to achieve rapid cooling of a substrate, as an alternative to using liquid coolants.

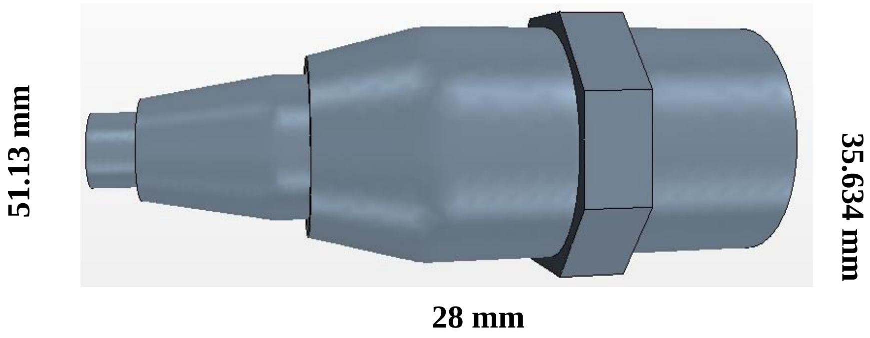

Figure 2.5: **Dimensions of non-adjustable Coanda nozzle**

A related process, the freeze-drying of liquid water with cold liquid nitrogen, was conducted by Ananharamakrishman et al [48]. They experimentally studied water droplet size and axial velocity at various distances below a cone spray pressure nozzle atomizer. CFD simulations were used to predict temperature profiles at various axial positions below the nozzle. Axial velocities at particle sizes of 17, 50, 100 and 150µm were measured in the spray at a chamber temperature of 231.15 K and at a gas inlet temperature at 203 K. The particle residence time distribution (RTD) was then calculated. CFD simulations were used as a tool to improve the spray-freeze operation for both a solid-cone spray and hollow-cone spray process design. A comparison study was done between experimental and predicted CFD variables on these two designs.

Lee et al. (36) studied the effect of a Coanda nozzle on flow characteristics of an air amplifier. Various values of Coanda nozzle clearances were considered along with three diffuser angles and four pressure conditions. Quantitative analysis was performed on each variable and the optimal configuration of the air amplifier was studied. Lee et al. concluded that the air amplifier has a 20° diffuser angle, and they subsequently showed that the most effective nozzle had a 20% higher discharge flow rate than the other models. Additionally, this work showed disperse angle and maximum velocity measurements on a spray nozzle for three sizes of dry ice particles. This analysis showed that a 20º diffuser angle allowed for the optimal spread on a substrate based on disperse angle, particle size and maximum velocity.

Compressed air enters the nozzle and is directed through the annular region around the exterior surface of the nozzle (36). The high velocity jet stream adheres to the curved exterior surface and entrains additional air from the surroundings, producing a high volume, high velocity flow downstream of the nozzle, as illustrated in the computational mesh diagram shown in Figure 2.6. The modification under consideration is an installation of a supply of liquid CO_2, delivered through a capillary tube coaxially within the air supply tube (35). To date, no articles have been reported in open literature on the CFD modeling of the spray-freeze non-adjustable Coanda nozzle on an open and closed boundary.

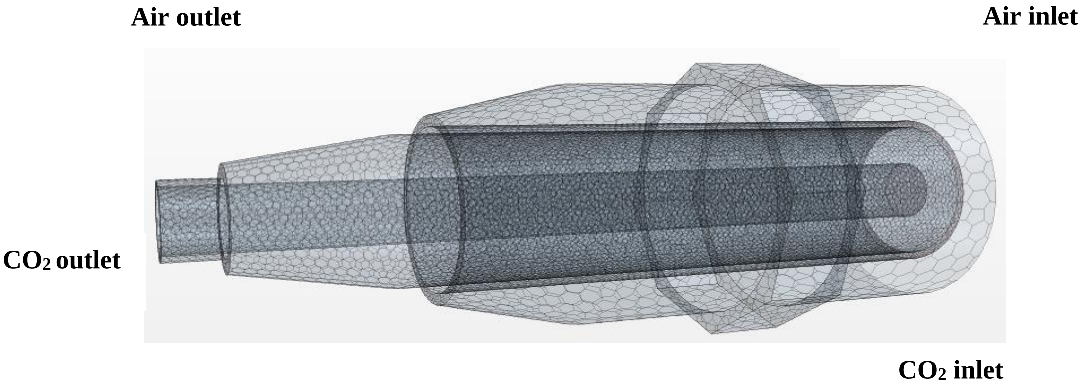

Figure 2.6: **Computational Domain and Meshing**

2.3 NOVEL TECHNOLOGY ON THE “SPRAY FREEZE PROCESS”

Wherein ordinary vacuuming and steam carpet cleaning are current technologies used to kill dust mites, dust mites must be exposed at a temperature greater than 60°C for a reasonable period to ensure death. The negative aspect of steam cleaning is that the items must remain wet for a significant period after cleaning. Dust mites thrive in damp environments and this moisture provides the remaining mites a jump-start on re-infestation. In addition, damp carpets or mattresses provide a compounding issue of mold spore formation and growth.

The technology behind this work focuses on a non-adjustable Coanda nozzle that delivers high speed dry ice spray to a carpet surface. The process uses a spray nozzle to create a spray of dry ice that jets both air and dry ice particles onto a carpet or mattress containing allergenic protein. The spray quickly drops the surface being treated to -30°C or lower. The turbulence and extreme temperature transition of the technology (to -30°C) kills dust mites with a high-suction vacuum to remove the mites, eggs, larva, nymphs and mite feces from carpets. This equipment simultaneously collects both the dislodged particles as well as the CO_2 as it sublimes from solid to gas. The surfaces return to room temperature in a matter of minutes, and the surface is then completely dry.

The spray penetrates the carpet, freezing dust mites deep into a carpet or mattress. A vacuum head then removes the dust, dust mites and other debris dislodged by the high-speed spray. The dry ice rapidly sublimes, leaving the carpet dry. Wherein most dry-cleaning companies use perchloroethylene as a solvent, the technology used in this work is CO_2 which is non-toxic and odorless.

The modification under consideration is the installation of a supply of liquid CO_2, delivered through a capillary tube coaxially inside the air supply tube (35). To this date, no articles have been reported in open literature on the CFD modeling of the spray-freeze non-adjustable Coanda nozzle on an open and closed boundary.

Two boundary specifications are analyzed in this work, a closed nozzle boundary and one open to the environment. The spray nozzle was modeled at 194.65 K and 101.325 kPa, respectively. The geometry used in this simulation was constructed with a CO_2 gas inlet area of 4.96 E-6 m^2 and an air flow area of 5.96 E-6 m^2. Air flow around the nozzle is designed for a velocity of 173.5 m/s. The system was designed for a total mass flow rate for air of 0.00126 kg/s (10lb_m/hour). CFD is simulated through STAR CCM+ version 9.06.011. The simulations are used as a tool to improve the freeze spray operation by determining maximum velocities and disperse angles on dry ice particles. Figure 2.7 shows a simulation for a Coanda nozzle enclosed in a square shaped channel. This model configuration is not exposed to the environment.

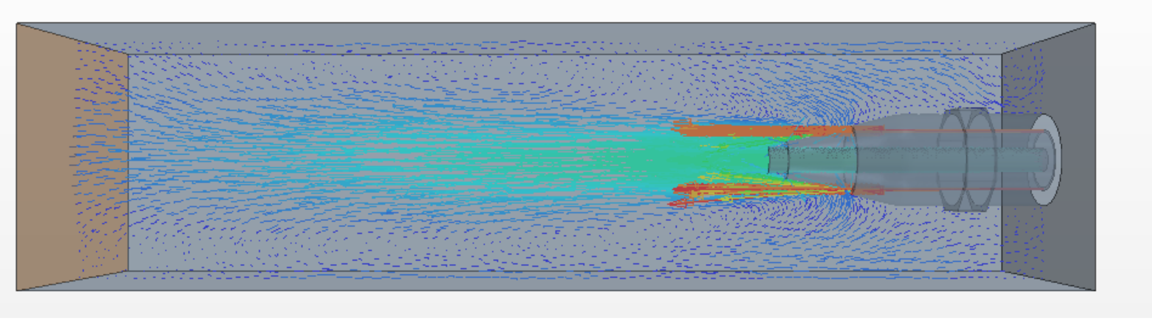

Figure 2.7: **Closed Nozzle Boundary**

In the closed nozzle boundary flow configuration, the air accelerating down the channel is reduced. CFD allowed for a comparison between these two boundaries.

The performance of this CO_2 spray cooling process, whether in dry ice cleaning, rapid cooling, or both, depends on both the nature of the solid/gaseous CO_2 mixture exiting the capillary, and on the hydrodynamics of both the CO_2 flow as well as the accelerating air stream produced by the Coanda effect.

The independent variables are CO_2 flow rate and temperature in the capillary supply, as well as the particle size of the dry ice. The process output variables are the velocity and residence time distributions of the particles as well as the CO_2/air mixture and the temperature distributions of the resultant flow.

2.4 MATHEMATICAL MODELLING ON THE SPRAY-FREEZE PROCESS

2.4.1 ENERGY BALANCE ON STEADY STATE FLOW

Table 3.1 shows the ΔP_{max} at each inlet temperature. The calculations show that as T_1 decreases, ΔP_{max} increases. In addition, as temperature increases, viscosity decreases and the Reynolds number increases. As Reynolds number increases, the friction factor decreases. As the friction factor decreases, both the velocity and the mass flow rate also decrease.

Table 2.1: $\mathbf{\Delta P_{maximum}=P_1-P_{CO2}^{sat}(T)}$

Inlet T (°C)	$\boldsymbol{\rho_1^{Liquid}}$**(kg/m^3)**	$\mathbf{P_1^{sat}}$**(MPa)**	$\mathbf{\Delta P_{maximum}}$**(MPa)**
0	929.4	3.485	2.75
10	836.6	4.500	1.74
20	775.2	5.727	0.51
30	593.1	7.211	0.28

The Reynolds number was determined at each temperature with a consistent turbulent flow. For turbulent flow, both Reynolds number and the wall roughness influence the friction factor. At high Reynolds number, the friction factor of rough pipes becomes constant, dependent only on the pipe roughness. For smooth pipes, Blasius (37), has shown that the friction factor (in a range of 3,000 < Re < 100,000) may be approximated by:

$$f = \frac{0.079}{Re^{0.25}} \qquad (2.1)$$

The Darcy-Weisbach equation (Equation 2.2) was used to determine the pressure drop (38). The Darcy-Weisbach equation is valid for fully developed, steady state and incompressible flow. The pressure drop can be calculated as a function of the density, velocity, friction factor and diameter.

$$\underline{\Delta} P = f \, \frac{L}{D} \, \frac{\rho \, v^2}{2} \qquad (2.2)$$

A capillary tube with an inside diameter of 2.5 mm was analyzed. The area of the tube was 4.96e-6 m^2. The nominal process pressure was at 904.7 psia and inlet temperatures ranging from 30°C down to 0°C. The density at the inlet was 0.775 g/cm^3. The viscosity at the inlet was 6.6 x $^{10-5}$Pa-s. It has been determined that the fluid under the listed conditions is a single phase in the form of liquid CO_2 flow due to small pressure drops through the capillary tube.

2.5 CFD MODEL DESCRIPTION

The CFD package STAR-CCM+ from Siemens was used to import the system geometry of the Coanda nozzle **.** The workflow in STAR-CCM CFD modeling is much the same as in other packages, such as ANSYS-FLUENT, FloTHERM, NX-Space Systems Thermal, COMSOL, etc. First the geometry is imported, then materials are assigned to components, boundary conditions are assigned, mesh is generated, solvers/models are selection, the equations of motion are then solved and results are post-processed.(39)

2.5.1 NUMERICAL MODEL

The Coanda nozzle has been developed as a detailed transport phenomena model, solved using the Finite Volume StarCCM+ software. The model includes mass, energy and momentum balance equation under multiphase, multicomponent, and turbulence phenomena. Multiphase flow is defined as one thermodynamic phase, be it a solid, a liquid, or a gas, interacting with another distinct phase. In this work, multicomponent gases (i.e., air and CO_2) are deemed as “continuous flow” and solid ice particles are allocated as the “dispersed phase” (40). Below are the governing equations for the model.

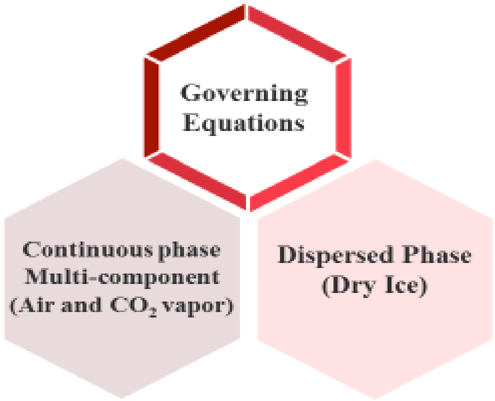

Figure 2.8: **Multi-Phase Mathematical Modeling**

Conservation of Mass

The two multicomponent gases used in the model are CO_2 and air. Multicomponent gases are modeled on the transport of one component within a mixture of both species. That phenomena occurs as a direct result of a concentration gradient. It is independent of a pressure gradient. The total mass of the mixture (M) is the sum of the mass of each constituent of the mixture (M_i), where i identifies the component. The mass fraction of species m (mf_m) is the ratio of the mass of species m to the total mass of the mixture. The concentration is the amount of the component present per unit volume and expressed as ρmf_m.

The general equation for the multicomponent conservation of mass is described by

$$\frac{\partial \rho}{\partial t} + \frac{\partial}{\partial x_i}(\rho u_i) = s_m (1)$$

Where *m* is the mixture of CO_2 and air gas phase and u_i represents the fluid velocity of the mixture in the horizontal *x*-direction and ρ the density. s_m is mass source or sink if applicable.

Momentum Transport Equation

Due to the high velocity coming out of the nozzle, a turbulent model was used in the model. The Reynolds Average Navier-Stokes equation (RANS), a set of time averaged equations for the fluid motion, was used in the CFD. In RANS, the averaged version of the Navier-Stokes equation along with k-ε turbulence equations represent all the turbulent scales. The k-ε is one version of a two-equation model that includes turbulent kinetic energy (k) and turbulent dissipation rate (ε) for predicting the behavior of turbulent flow. The three equations are shown below.

$$\rho\frac{\partial \bar{u}_i}{\partial t} + \rho\frac{\partial \bar{u}_i\bar{u}_j}{\partial x_i} = \rho\bar{f}_i + \frac{\partial}{\partial x_i}\left[-\bar{p}\delta_{ji} + 2\mu\bar{S}_{ji} - \rho\overline{\acute{u}_j\acute{u}_i}\right] \qquad (2)$$

where $\bar{S}_{ji} = \frac{1}{2}\left(\frac{\partial \bar{u}_j}{\partial z_i}\right) + \left(\frac{\partial \bar{u}_i}{\partial x_j}\right)$

The k-ε model used in this model is governed by the following equations.

$$\frac{\partial k}{\partial t} + U_i\frac{\partial k}{\partial x_i} = \frac{u_t}{\rho}S^2 - \varepsilon + \frac{\partial}{\partial x_i}\left[\frac{1}{\rho}\left(\mu + \frac{\mu_t}{\sigma_k}\right]\frac{\partial k}{\partial x_i}\right] \qquad (3)$$

$$\frac{\partial \varepsilon}{\partial t} + U_i\frac{\partial \varepsilon}{\partial x_i} = \frac{\varepsilon}{k}\left(C_{1\varepsilon}\frac{\mu_t}{\rho}S^2 - C_{2\varepsilon}\varepsilon\right) + \frac{\partial}{\partial x_i}\left[\frac{1}{\rho}\left(\mu + \frac{\mu_t}{\sigma_\varepsilon}\right]\frac{\partial \varepsilon}{\partial x_i}\right] \quad (4)$$

where $\mu_t = \rho C_\mu \frac{k^2}{\varepsilon}$

Walls have a significant effect on turbulent flow related to the no-slip boundary condition. High y+ is a non-dimensional distance similar to local Reynolds number, often used in CFD to describe how coarse or fine a mesh is for a particular flow. y+ is the ratio between the turbulent and laminar influences in a cell (41). For turbulent modeling with very high Reynolds numbers, it is suitable for coarse meshes where the wall cell y+ values are typically 30 and above. In this research the wall cell y+ value was 50 (41).

Species Transport Equation

In terms of each multicomponent, the conservation of mass equation that accounts for each species can also be written as

$$\frac{\partial}{\partial t}(\rho m f_m) + \nabla(\rho u m f_m) = \nabla\left(\frac{\mu_t}{\sigma_t}\frac{\partial m f_m}{\partial x_i}\right) + S_m \qquad (5)$$

Where σ_t represents the turbulent Schmidt number and S_m represents the rate of mass production or consumption.

Energy Transport Equation

The general equation for the conservation of energy is modeled as:

$$\frac{\partial \rho h}{\partial t} + \frac{\partial}{\partial x_i}(\rho h u_i + F_{h,i}) = \frac{\partial p}{\partial t} + u_i\frac{\partial p}{\partial x_i} + \tau_{ji}\frac{\partial u_j}{\partial x_i} + s_h (6)$$

Here, *h* is the thermal enthalpy, defined by:

$$h = \bar{c}_p T - \bar{c}_p^o T_o$$

$F_{h,i}$ is diffusional thermal energy flux in direction i, defined by:

$$F_{h,i} = -k\frac{\partial T}{\partial x_i} + \bar{\rho}\,\overline{u_i' h_\iota} + \sum\nolimits_m h_m \rho V_{m,i} (7)$$

2.5.2 DISPERSED PHASE MODEL

Dispersed multi-phase flows are found in a wide variety of industrial plant processes. Dispersed phases are in the form of solid particles, such as dry ice, presented in this research. The Lagrangian multiphase model solves the equation of motion for material particles as they pass through the system. Material particles are the most general

Lagrangian multiphase dispersed phase that have both mass and volume and are governed by Lagrangian conversation laws of mass, momentum, and energy. The conservation equation of momentum for a solid particle is written within the Lagrangian framework, in which the conservation of mass, momentum and energy for the dispersed phase are written for each individual element (40). The change in momentum is balanced by surface and body forces that act on a particle.

The particle conservation equation of momentum is also known as the particle equation of motion (42). The change in momentum is balanced by surface and body forces that act on a particle.

$$m_p \frac{dV_d}{dt} = F_s + F_b \ (8)$$

Where v_p denotes the instantaneous particle velocity, F_s is the resultant of the forces that act on the surface of the particle, F_b is the resultant of the body forces and m_p represents the particle mass. These forces are decomposed into:

$$F_s = F_d + F_p + F_{vm} \text{ and } F_b = F_g \ (9)$$

Where F_d represents the drag force, F_p represents the pressure gradient force, F_{vm} represents the virtual mass force, and F_g represents the effects of gravity and acceleration.

Drag force is defined as:

$$F_d = \frac{1}{2} C_d \rho A_p |v_s| v_s \ (10)$$

Where C_d represents the drag coefficient of a particle. ρ is the density and $v_s = v - v_p$, representing the particle slip velocity with v being the instantaneous velocity and A_p representing the projected area of the particle.

The Schiller-Naumann correlation (43) is suitable for spherical solid particles. This equation is formulated as:

$$C_d = \begin{cases} \frac{24}{Re_p}\left(1 + 0.15 Re_p^{0.687}\right) & Re_p \leq 10^3 \\ 0.44 & Re_p > 10^3 \end{cases} \quad (11)$$

Where Re_p is the particle Reynolds number that is defined as:

$$Re_p = \frac{\rho[v_s]D_p}{\mu}$$

Where D_p is the particle diameter and μ is the dynamic viscosity.

F_p is defined as the pressure force given by

$$F_p = V_d \nabla p \quad (12)$$

Where V_d is the droplet volume and ∇p is the pressure gradient in the carrier fluid, p is inclusive of any hydrostatic components.

F_{vm} is the "virtual mass" force required to accelerate the fluid entrained by the droplet. The expression for this is

$$F_{vm} = - C_{am} \rho V_d \frac{d(u_d - u)}{dt} \quad (13)$$

Where C_{am} is the virtual mass coefficient set to 0.5.

F_b is the general body force which represents the effects of gravity and accelerations present in a non-inertial coordinate frame given as

$$F_b = m_p g \quad (14)$$

2.6 NUMERICAL PROCEDURE

CO_2 exits the nozzle at the sublimation point, the point where a mixture of dry ice particles and vapor coexist, of 195 K and atmospheric pressure. Both vapor and solid particles are accelerated by the air flow from the Coanda nozzle. Prior to initiating CFD calculations, it was essential to compute the fraction of CO_2 that is solid, represented by the expression, $1-x_2$, at the nozzle outlet. This fraction is determined by a steady state energy balance, assuming adiabatic flow of liquid CO_2 through the nozzle and allowing for kinetic energy of the flowing CO_2. The expression x_2 represents the mass fraction of vapor. The resulting equation representing energy balance is:

$$H_{2=}\ H_1 + \frac{1}{2} v_{1^2} - \frac{1}{2}\left[\left(\frac{\dot{m}}{A}\right) * \left(\frac{x_2}{\rho_v} + \frac{1-x_2}{\rho_s}\right)\right]^2$$

$$H_2 = x_2 H_2^v + (1-x_2) H_2^s \mathbf{(15)}$$

The outlet properties are fixed by virtue of the CO_2 being at sublimation conditions, where the enthalpy of dry ice, denoted as H_2^s is 152.1 kJ/kg and the enthalpy of vapor state, denoted as H_2^v is 723.1 kJ/kg. The density of the solid state, denoted as ρ_s is 1,562 kg/m^3 and the vapor density, denoted as ρ_v is 2.82 kg/m^3.(44)

The inlet enthalpy, H_1, of liquid CO_2 depends on temperature T_1. For instance, at 30°C (45) H_1 is 602.5 kJ/kg. By specifying T_1, equation 15 has only one remaining unknown variable, x_2. We can then determine H_2 of the dry ice and gaseous CO_2 from the energy balance equation (38). Prior to simulation, the energy balance equation was used to determine the mass fraction of dry ice ($1-x_2$). These values along with the outlet velocities (v_2) were then used as inputs into the CFD simulation.

In addition, three particle sizes were selected as inputs into the CFD simulation to illustrate closed and open nozzle behavior. Since we were unsure as to what an exact dry ice particle size coming out of the nozzle would be, we selected particle sizes at 10µm, 100µm and 1000µm for observation purposes. The full set of CFD input and boundary values are shown in Table 2.2.

Table 2.2:**Operating conditions and parameters**

Process Variables	Value
Density of CO_2 vapor	2.819 kg/m^3
Density of CO_2 solid	1,562 kg/m^3
Air flow velocity	173.5 m/s

Temperature	194.65 K
Pressure	101.325 kPa
Fraction of CO_2 vapor at an inlet temperature of 0°C	0.598
Fraction of CO_2 solid at an inlet temperature of 0°C	0.402
Mass flow rate of CO_2 vapor at an inlet temperature of 0°C	0.00075 kg/s
Mass flow rate of CO_2 solid at an inlet temperature of 0°C	0.00051 kg/s
Velocity of CO_2 vapor at an inlet temperature of 0°C	53.9 m/s
Velocity of CO_2 solid at an inlet temperature of 0°C	0.066 m/s
Fraction of CO_2 vapor at an inlet temperature of 10°C	0.642
Fraction of CO_2 solid at an inlet temperature of 10°C	0.358
Mass flow rate of CO_2 vapor at an inlet temperature of 10°C	0.00081 kg/s
Mass flow rate of CO_2 solid at an inlet temperature of 10°C	0.00045 kg/s
Velocity of CO_2 vapor at an inlet temperature of 10°C	57.9 m/s
Velocity of CO_2 solid at an inlet temperature of 10°C	0.058 m/s
Fraction of CO_2 vapor at an inlet temperature of 20°C	0.694
Fraction of CO_2 solid at an inlet temperature of 20°C	0.306
Mass flow rate of CO_2 vapor at an inlet temperature of 20°C	0.00087 kg/s
Mass flow rate of CO_2 solid at an inlet temperature of 20°C	0.00039 kg/s
Velocity of CO_2 vapor at an inlet temperature of 20°C	62.6 m/s
Velocity of CO_2 solid at an inlet temperature of 20°C	0.050 m/s
Fraction of CO_2 vapor at an inlet temperature of 30°C	0.784
Fraction of CO_2 solid at an inlet temperature of 30°C	0.216
Mass flow rate of CO_2 vapor at an inlet temperature of 30°C	0.000987 kg/s
Mass flow rate of CO_2 solid at an inlet temperature of 30°C	0.00027 kg/s
Velocity of CO_2 vapor at an inlet temperature of 30° C	71.0 m/s
Velocity of CO_2 solid at an inlet temperature of 30° C	0.035 m/s
Particle size diameters	10μm, 100μm, 1000μm
Air-CO_2 diffusivity	0.000016 m^2/s
Fluid 1 inlet species mass fraction	(Air = 0; CO_2 = 1)
Fluid 2 inlet species mass fraction	(Air = 1; CO_2 = 0)

The two cases examined are as follows.

Case A - Pressure outlet: A pressure is specified at the outlet. This refers to the case where the nozzle is open to the environment.

Case B - Wall: An adiabatic wall has been modeled at constant temperature.

Simulated dry ice particle velocities with varying sizes were compared for both open and closed boundary nozzles at each inlet temperature

A polyhedral mesh and surface re-mesher were used for the spray-nozzle, as shown in the grid geometry in Figure 2.6. The surface re-mesher was chosen to improve the overall quality of surface mesh and to optimize the surface mesh for generating volume mesh. The polyhedral mesher was chosen to fill the volume inside the surface mesh for which the solver equations work through. Particle data were extracted from the simulation post-processing. Three particle sizes (10µm, 100µm, and 1000µm) were selected to illustrate behavior. For convergence, the residual was set to 1 x 10^{-4}m.

The following model assumptions were made in this work. 1. the flow through the Coanda nozzle is representative of only one phase, namely, dry ice. There is no phase change through the nozzle itself, 2. we assumed and modeled the dry ice particle sizes coming out of the nozzle to be 10µm, 100µm and 1000µm respectively without any variations of size.

2.7 THE EFFECT OF INLET NOZZLE TEMPERATUE ON *1-X_2*

Liquid CO_2 expands rapidly at the tip of the capillary tube before expending CO_2 vapor and solid. A fixed mass flow rate, $\dot{m}_{co2}$ of 0.00126 kg/s was observed as analogous to field environment. This constant provided the mass fraction of dry ice and vapor. Table 2.3 shows the effect that at a given nozzle inlet temperature had on the mass fraction of dry ice.

Table 2.3: **Energy balance on adiabatic nozzle at stead state at p_1=6237.7 kpa (904.7 psia)**

Outlet Conditions: T_2= -78.5˚C; P_2=101.325 kPa (14.7 psia); ρ_2^{solid}=1,562 kg/m^3 = 1.56200 g/cc; H_2^{solid}=152.1 kJ/kg; H_2^{vapor}=723.1 kJ/kg; Inlet Pressure = 6237.7 kPa (904.7 psia); mass flow rate = 0.00126 kg/s = 10 lb$_m$/hour

Inlet T (°C)	ρ2(kg/m3)	ρ_2(kg/m^3)	V_1(m/s)	V_2(m/s)	$1-x_2$
0	924.4	4.71	0.28	53.9	0.402
10	863.6	4.38	0.30	57.9	0.358
20	775.2	4.05	0.33	62.6	0.306
30	593.1	3.59	0.43	71.0	0.216

The mixture density (ρ_2) of the dry ice and vapor as well as the outlet velocity (v_2) were determined from the energy balance equation. The density mixture (ρ_2) decreases while the velocity of the mixture (v_2) steadily increases. This phenomenon provides evidence suggesting the speed velocity and mixture density for both dry ice and vapor as they exit a Coanda nozzle tip. Figure 2.9 shows that as the inlet nozzle temperature increases, the mass fraction of dry ice decreases.

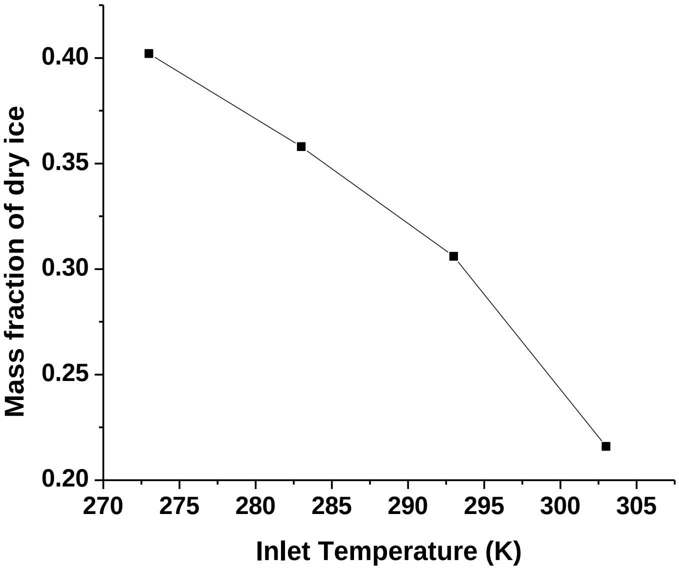

Figure 2.9: **The effect of T_1 on $1-x_2$**

This phenomenon gives insight on how the inlet nozzle temperature can affect the output of the system. The ability to cool the substrate is dependent upon the inlet temperature. The graph provides an indication as to what the inlet temperature would need to be in order to lay down the dry ice. On very hot days, not much dry ice is produced at the nozzle inlet temperature. Insulating the CO_2 line or adding refrigeration could indeed produce a fair amount more dry ice. Refrigeration would almost double the amount of dry ice produced between an inlet nozzle temperature of 273 K and 303 K.

2.8 THE EFFECT OF *1-X₂* ON MAXIMUM VELOCITY

The maximum velocity was analyzed for each scenario as a function of three dry ice particle sizes, 10µm, 100µm, and 1000µm. Simulation results for each particle size are shown individually for both the open and closed boundaries in Figure 2.10.

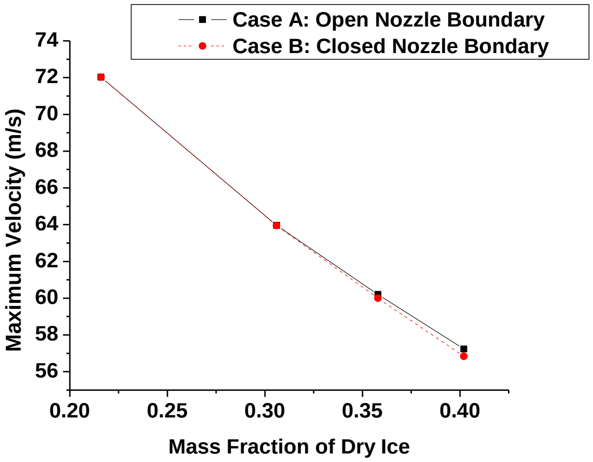

(a)

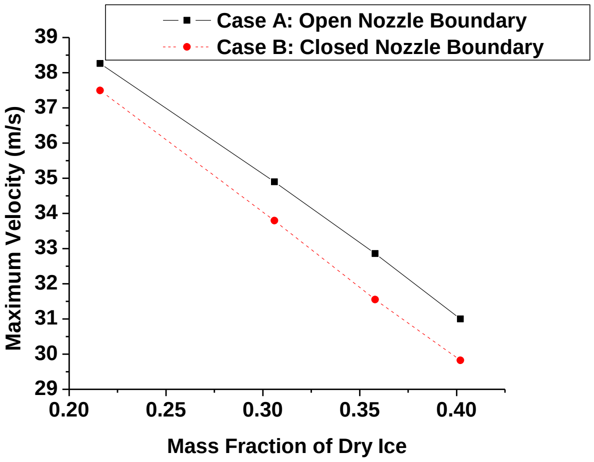

(b)

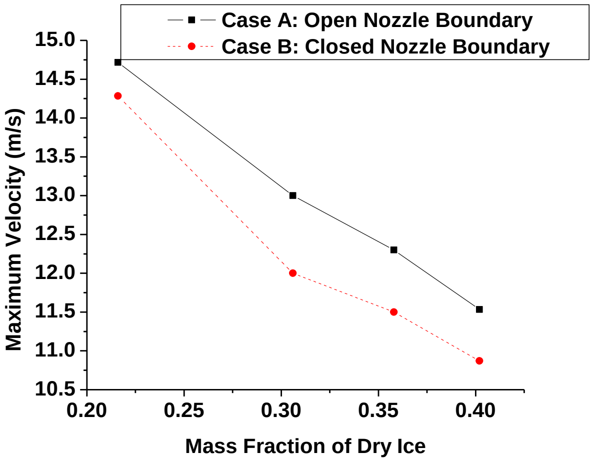

(c)

Figure 2.10: **The Effect of Dry Ice Mass Fraction on Maximum Velocity at Particle Size a) 10µm b) 100µm and c) 1000µm**

The maximum velocity for a dry ice particle at the smallest particle size of 10µm as a function of dry ice mass fraction is shown in Figure 2.10a. The maximum velocity ranged from 57.2 m/s to 72.0 m/s for a nozzle exposed to the environment and from 56.8 m/s to 72.0 m/s for a nozzle designed under closed condition. Open and closed boundaries for 10µm dry ice particle sizes were similar. Both have higher maximum velocities relative to larger particle sizes.

Table 2.4**: Track particle velocity at 10μm on open and closed nozzle boundary**

Mass Fraction	**Open Nozzle Boundary Velocity (m/s)**	**Closed Nozzle Boundary Velocity (m/s)**
0.216	72.0	72.0
0.306	63.9	63.9
0.358	60.2	60.0
0.402	57.2	56.8

The behavior for the maximum velocity for a dry ice particle size at 100μm as a function of dry ice mass fraction for both closed and opens nozzle boundaries is shown in Figure 2.10b. The maximum velocity ranges from 31.1 m/s to 38.3 m/s for a nozzle exposed to the environment and 30.0 m/s to 37.5 m/s for a nozzle within a closed boundary. Compared to the dry ice particle size at 10μm, dry ice particles at 100μm have a lower velocity. The smaller the particle size, the faster the dry ice particle moves out of the nozzle on both boundaries.

Table 2.5: **Track particle velocity at 100μm on open and closed nozzle boundary**

Mass Fraction	**Open Nozzle Boundary Velocity (m/s)**	**Closed Nozzle Boundary Velocity (m/s)**
0.216	38.3	37.5
0.306	34.9	33.8
0.358	32.9	31.6
0.402	31.0	29.8

The maximum velocity of dry ice particles at the largest dry ice particle size of 1000μm as a function of dry ice mass fraction is shown in Figure 2.10c. The velocities range from 11.5 m/s to 14.7 m /s for a nozzle open to the environment and 10.9 m/s to 14.2 m/s for a closed boundary nozzle. The results show the lower inlet nozzle temperatures have the slowest velocities. Since temperature is proportional to velocity, we would expect that the higher inlet temperatures correlate to faster velocities.

Table 2.6: **Track particle velocity at 1000µm on open and closed nozzle boundary**

Mass Fraction	**Open Nozzle Boundary Velocity (m/s)**	**Closed Nozzle Boundary Velocity (m/s)**
0.216	14.7	14.3
0.306	13.0	12.0
0.358	12.3	11.5
0.402	11.5	10.9

Results also indicate that heavier dry ice particles (100µm and 1000µm) have greater dispersion angles than smaller dry ice particles at 10µm. In each particle size case study, simulations of the closed boundary maximum velocity was lower than when the Coanda nozzle was exposed to the environment, with the exception of the 10µm size which correlated the closest at higher temperatures. This would be the case in an open boundary where there is more drag force due to the surrounding environment. This analytical model provides us with an idea on the speed of dry ice particles at various particle sizes for rapid dry cooling and cleaning processes.

2.9 THE EFFECT OF 1-X_2 ON DISPERSE ANGLE

The disperse angle for each of the three particle sizes on both open and closed nozzle boundaries at various mass fractions is shown in Figure 2.11. Dry ice particles exit the nozzle differently for each of the three particle sizes. The angle at which they spread and hit the substrate is critical for effective treatment.

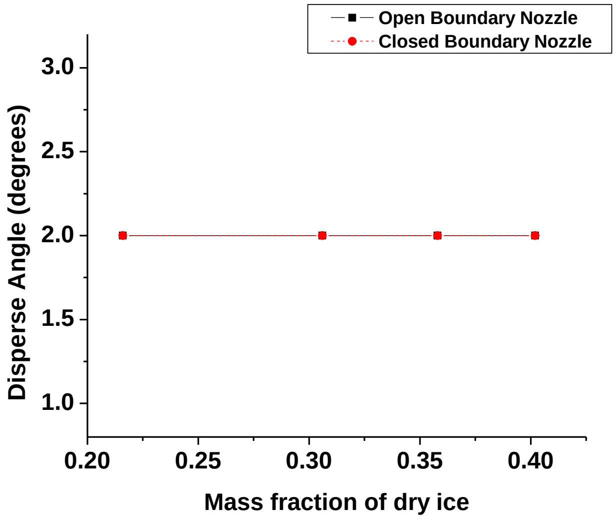
Open Boundary Nozzle
Closed Boundary Nozzle
Disperse Angle (degrees)
3.0
2.5
2.0
1.5
1.0
0.20
0.25
0.30
0.35
0.40
Mass fraction of dry ice

(a)

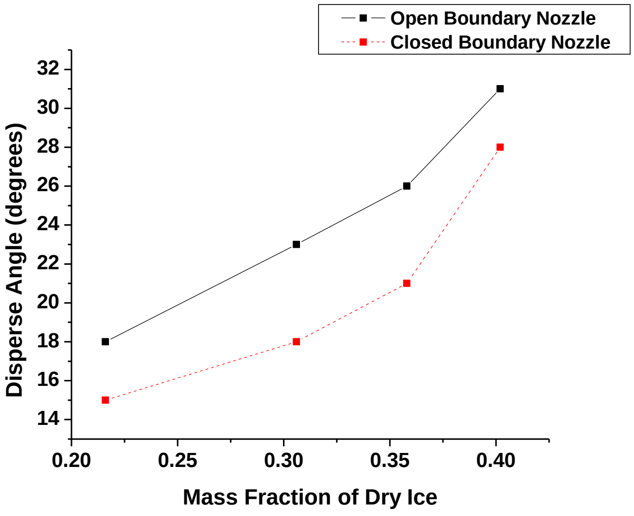
Open Boundary Nozzle
Closed Boundary Nozzle
Disperse Angle (degrees)
32
30
28
26
24
22
20
18
16
14
0.20
0.25
0.30
0.35
0.40
Mass Fraction of Dry Ice

(b)

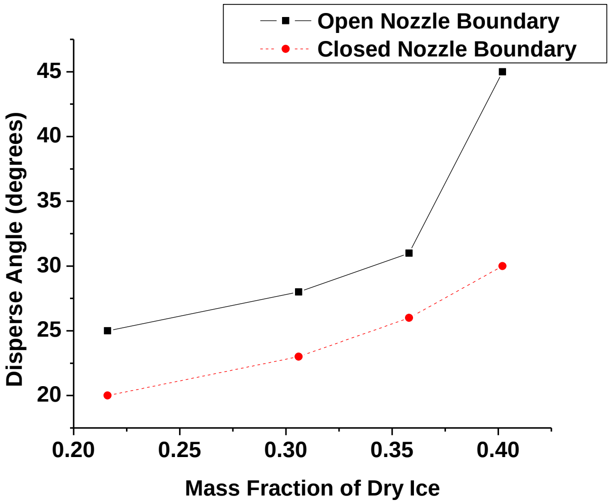

(c)

Figure 2.11: **The Effect of Dry Ice Fraction on Disperse Angle at Particle Size a) 10µm b) 100µm and c) 1000µm**

The effect of dry ice mass fraction on the 10µm particle size is shown in Figure 2.11a. Particles exit the nozzle horizontally and have a very small dispersion angle of 2° for both open and closed nozzle boundary. However, as particle size increases, the dispersion angle increases.

The effect of dry ice mass fraction on the 100µm particle size is shown in Figure 2.11b. Table 2.7 identifies the disperse angle on open and closed nozzle boundaries at a variety of mass fraction scenarios for 100µm particles. On the open nozzle boundary, the angle disperses dry ice at 18° while the closed boundary disperses at 15° for a mass fraction of 0.216. At the mass fraction of 0.306, the open boundary dispersion angle increased to 23° while the closed boundary dispersion angle increased to only 18°. For mass fraction of 0.358, the open boundary dispersion angle increased to 26°, while the closed nozzle boundary increased to 21°. At the highest mass fraction at 0.402, the open boundary disperses at 31°, while the closed boundary disperses at 28°.

Table 2.7: **Disperse Angle at 100μm on Open and Closed Nozzle Boundary**

Mass Fraction	Open Nozzle Boundary Disperse Angle (degrees)	Closed Nozzle Boundary Disperse Angle (degrees)
0.216	18	15
0.306	23	18
0.358	26	21
0.402	31	28

The effect of dry ice mass fraction for the 1000μm particle size is shown in Figure 2.11c. Table 2.8 shows the dispersion angles at the 1000μm particle size for open and closed nozzle boundary scenarios. At the lowest mass fraction of 0.216, the open nozzle boundary dispersed at an angle of 25°, while the closed nozzle boundary dispersed at 20°. At the mass fraction of 0.306, the open nozzle boundary dispersion angle increased to 28°, while the closed nozzle boundary increased to 23°. At the mass fraction of 0.358, the open nozzle boundary increased to 31°, while the closed nozzle boundary increased to 26°. At the highest mass fraction of 0.402, the open nozzle boundary dispersed at 45°, while the closed nozzle boundary dispersed at 30°.

Table 2.8: **Disperse Angle at 1000μm on Open and Closed Nozzle Boundary**

Mass Fraction	Open Nozzle Boundary Disperse Angle (degrees)	Closed Nozzle Boundary Disperse Angle (degrees)
0.216	25	20
0.306	28	23
0.358	31	26
0.402	45	30

These results taken together reveal that as the mass fraction of dry ice increases the dispersion angle increases on both open and closed nozzle boundaries. Open boundaries have higher dispersion angles due to atmospheric air and surroundings. This model gives a rapid and cool cleaning entity an idea on what the size of a dry ice particle might be in order to get the maximum spread onto a potential substrate.

2.10 DRY ICE PARTICLES EXITING THE COANDA NOZZLE AT *$1-X_2=0.216$* AT THE INLET NOZZLE TEMPERATURE AT 30°C ON OPEN AND CLOSED NOZZLE BOUNDARY

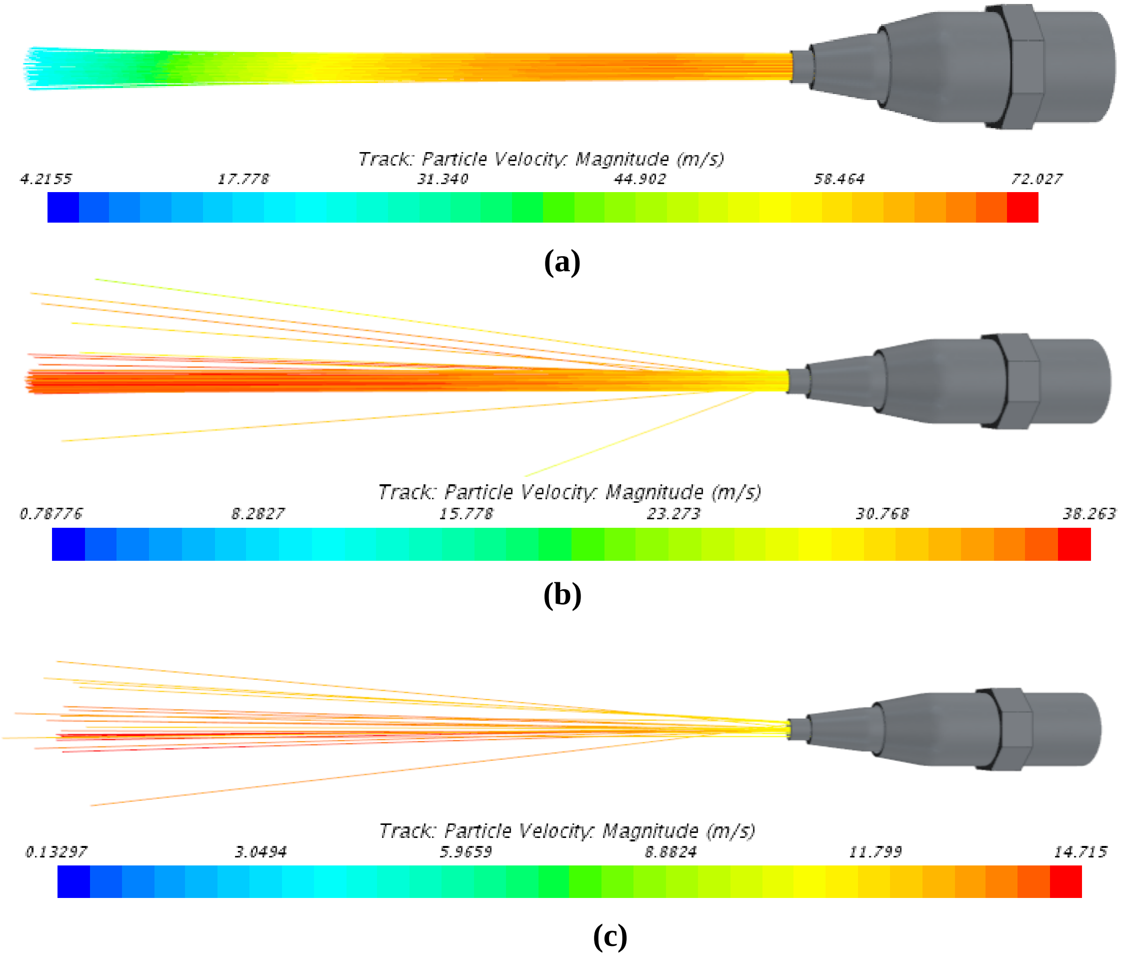

Figure 2.12: **Dry Ice Fraction = 0.216: Open Boundary maximum velocity on dry ice particles at a)10µm b)100µm c)1000µm**

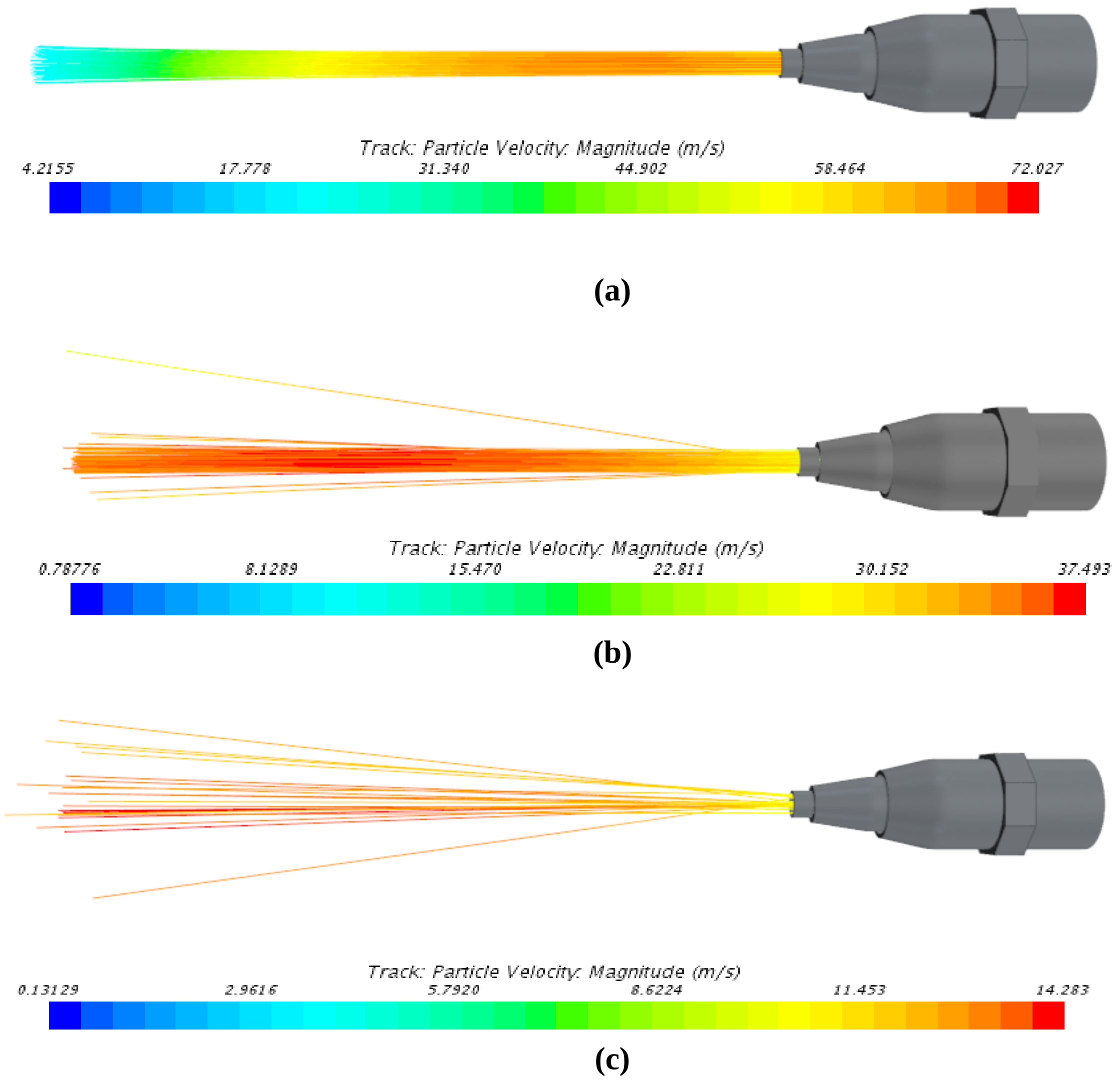

Figure 2.13: **Dry Ice Fraction = 0.216: Closed Boundary maximum velocity on dry ice particles at a)10µm b)100µm c)1000µm**

2.11 DRY ICE PARTICLES EXITING THE COANDA NOZZLE AT $1\text{-}X_2=0.306$ AT THE INLET NOZZLE TEMPERATURE AT 20°C ON OPEN AND CLOSED NOZZLE BOUNDARY

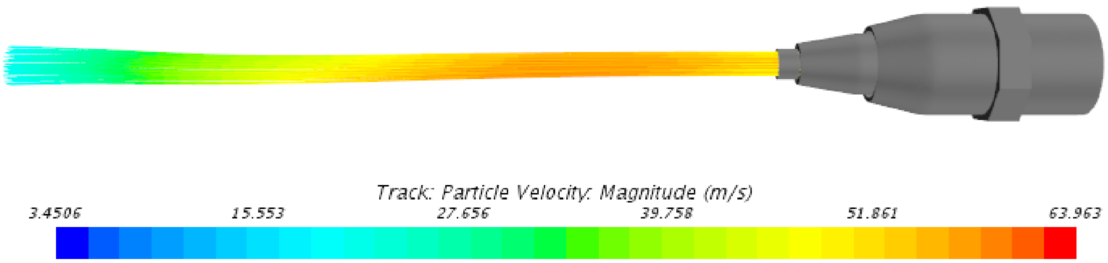

(a)10 µm

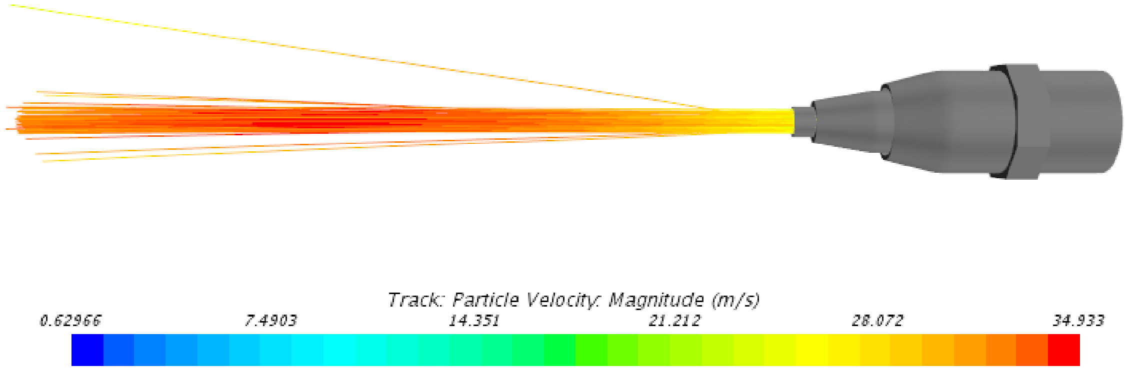

(b)100 µm

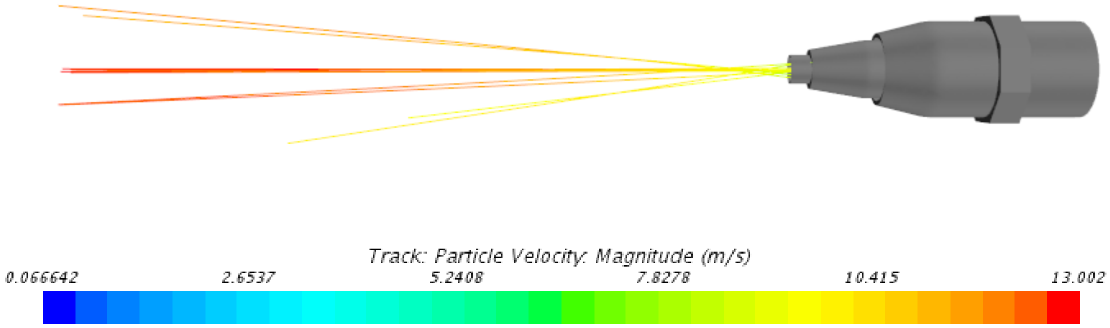

(c)1000 µm

Figure 2.14: **Dry Ice Fraction = 0.306: Open Boundary maximum velocity on dry ice particles at a)10µm b) 100µm c) 1000µm**

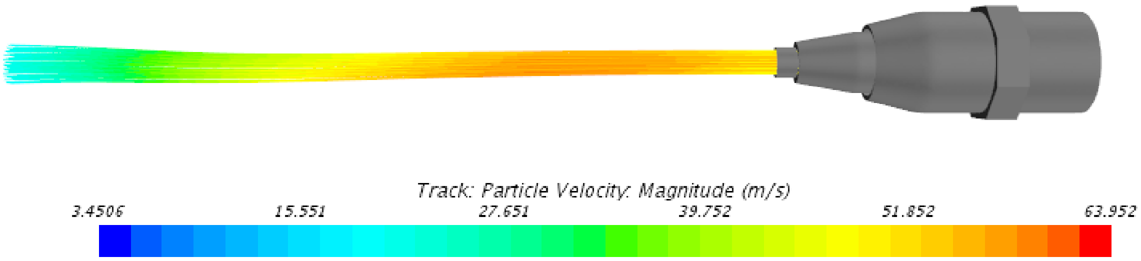

(a)10 μm

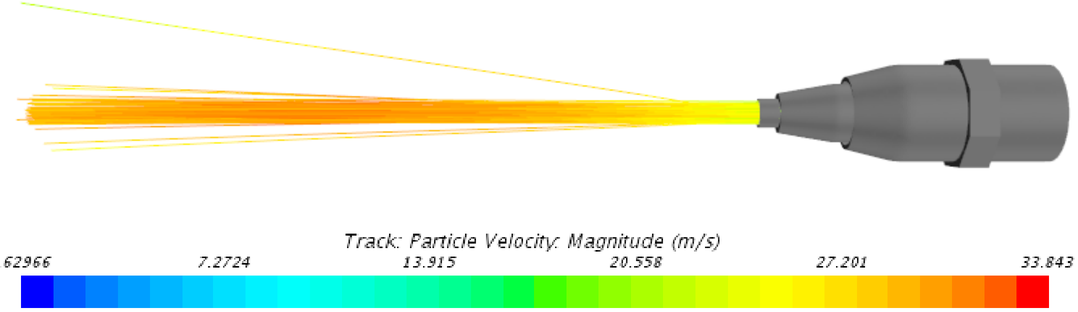

(b)100 μm

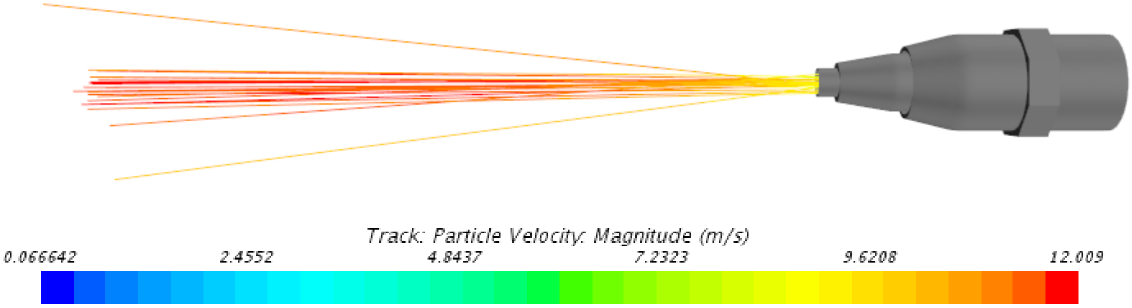

(c)1000 μm

Figure 2.15: **Dry Ice Fraction = 0.306: Closed wall maximum velocity on dry ice particles at a)10μm b) 100μm c) 1000μm**

2.12 DRY ICE PARTICLES EXITING THE COANDA NOZZLE AT *$1\text{-}X_2=0.358$* AT THE INLET NOZZLE TEMPERATURE AT 10°C ON OPEN AND CLOSED NOZZLE BOUNDARY

Figure 2.16 shows the availability of more or less dry ice coming out of the Coanda nozzle with respect to the disperse angle for an open nozzle boundary.

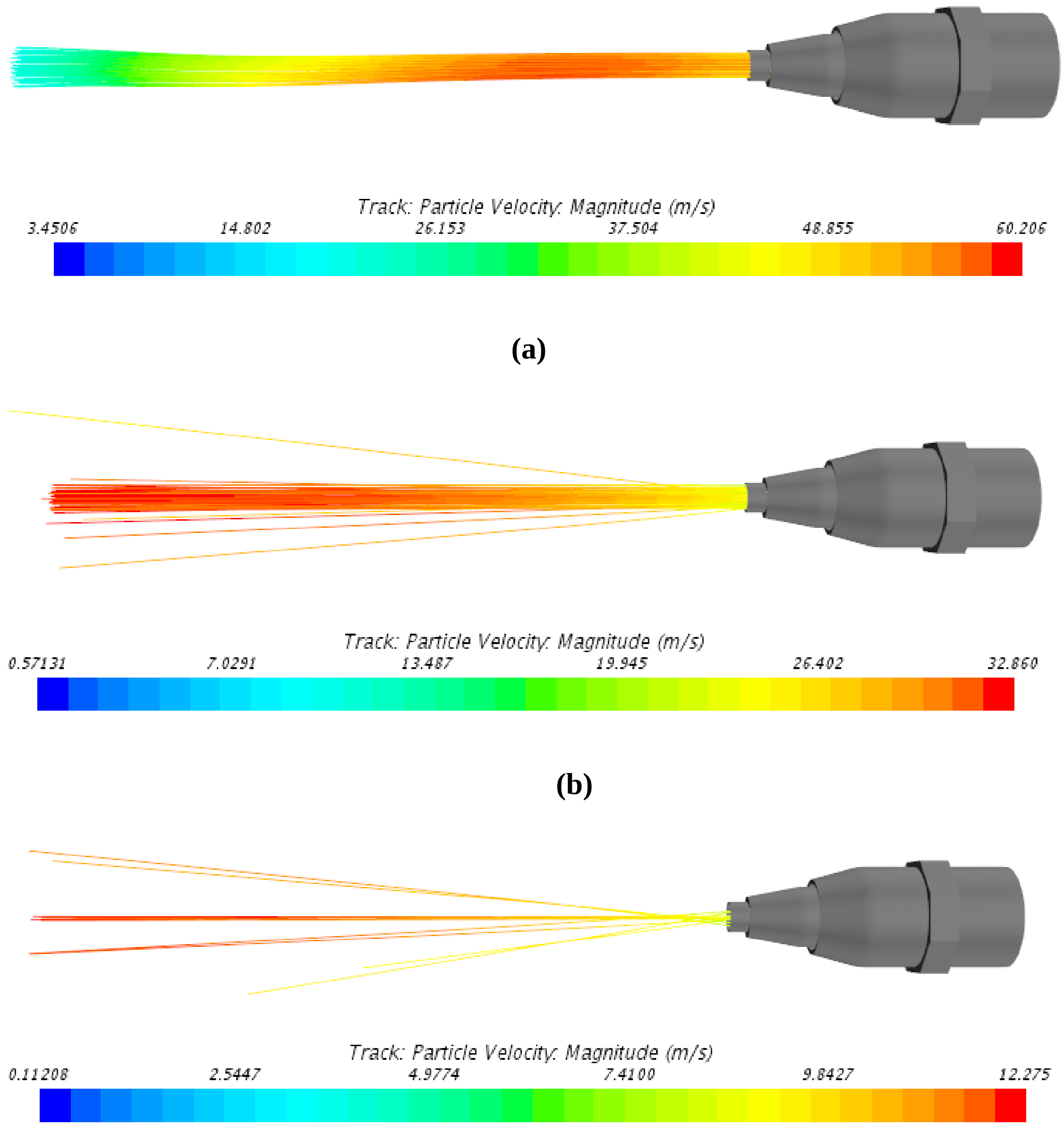

(a)

(b)

(c)

Figure 2.16: **Dry Ice Fraction = 0.358: Open Boundary Maximum Velocity on Dry Ice Particles at a)10µm b)100µm c)1000µm**

The maximum track velocities on an open nozzle boundary have already been recorded, in Figure 2.13, and dispersion angles have been recorded in Figure 2.14.

Figure 2.16a shows the track particle velocity for the 10 µm particle size on an open nozzle boundary. The dispersion angle was constant at 2° and the dry ice particles come out of the nozzle in a relatively linear manner. The maximum track velocity for this size particle was shown in Figure 2.13a. The dispersion angle remains constant for each mass fraction of dry ice as illustrated in Figure 2.14a.

Figure 2.14b shows the track particle velocity for the 100 µm particle on an open nozzle boundary. The dry ice particles coming out of the nozzle scatter at various angles as they come out of the nozzle, compared to the 10µm particle size. The dispersion angles increase as illustrated in Figure 2.15b. The maximum velocity also decreases as shown in Figure 2.14b.

Figure 2.16c shows the track particle velocity for the 1000 µm particle size on an open nozzle boundary. Dry ice particles coming out of the nozzle have a higher dispersion angle as compared to the 10 and 100 µm particle sizes. The maximum velocity also decreases as shown in Figure 2.13c.

Figure 2.17 shows the availability of more or less dry ice coming out of the Coanda nozzle for a closed nozzle boundary.

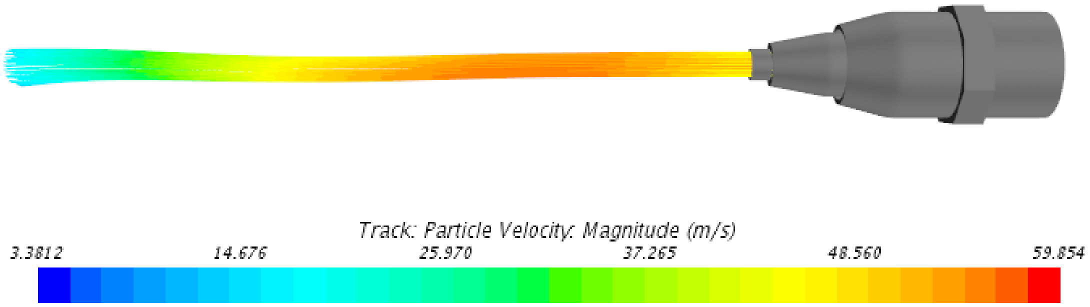

(a)

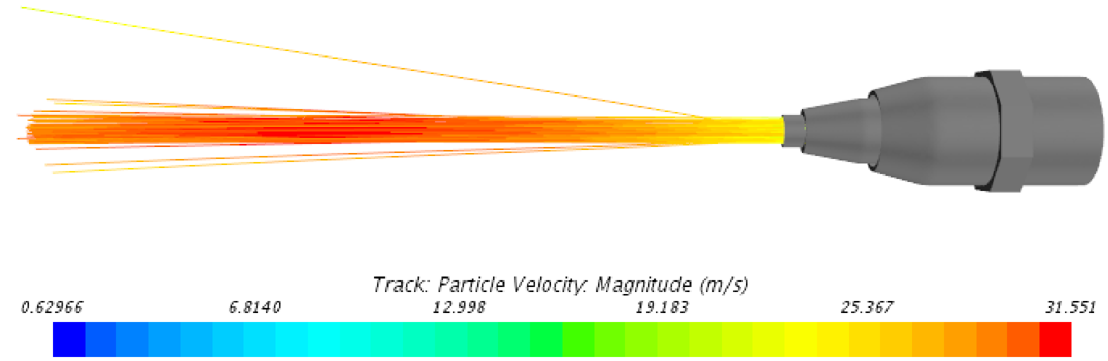

(b)

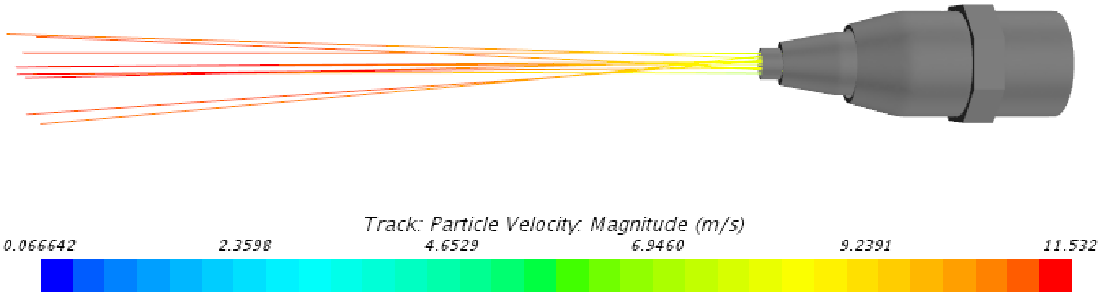

(c)

Figure 2.17: **Dry Ice Fraction = 0.358: Closed boundary Maximum Velocity on Dry Ice Particles at a) 10µm b) 100µm c) 1000µm**

The maximum track velocities on closed nozzle boundaries have already been illustrated in Figure 2.14 along with dispersion angles in Figure 2.15.

Figure 2.17a shows the track particle velocity for the 10µm particle size on a closed nozzle boundary. Similar to the open nozzle boundary, the dispersion angle was constant at 2°. The distribution shows a linear profile for dry ice particles as they leave the nozzle.

Figure 2.17b shows the track particle velocity for the 100µm particle size on a closed nozzle boundary. There is a higher scatter profile of dry ice particles that come out of the nozzle boundary as compared to the 10µm particle size. Relative to the open nozzle boundary, the maximum velocity is lower as shown in Figure 2.17b and the disperse angle is lower as shown in Figure 2.16b.

Figure 2.17c shows the maximum particle velocity for the 1000µm particle size on a closed nozzle boundary. Similar to the open nozzle boundary, the amount of scatter is at its greatest with 1000µm sized particles as compared to the 10 and 100µm particle sizes. Again, the maximum particle size is lower than the open nozzle boundary, shown in Figure 2.14c, as well as the dispersion angles are lower than its open nozzle boundary counterpart as shown in Figure 2.15c.

The open and closed nozzle boundary results are essential for optimizing potential spread of dry ice particles coming out of a nozzle. Due to atmospheric air, the maximum velocities as well as the dispersion angles are greater than when the nozzle boundary in enclosed. This phenomenon is critical based on the amount of surface serviced, the model gives us an idea on how much spread is involved when dry ice exits a Coanda nozzle.

2.13 DRY ICE PARTICLES EXITING THE COANDA NOZZLE AT $1-X_2=0.402$ AT THE INLET NOZZLE TEMPERATURE AT 0°C ON OPEN AND CLOSED NOZZLE BOUNDARY

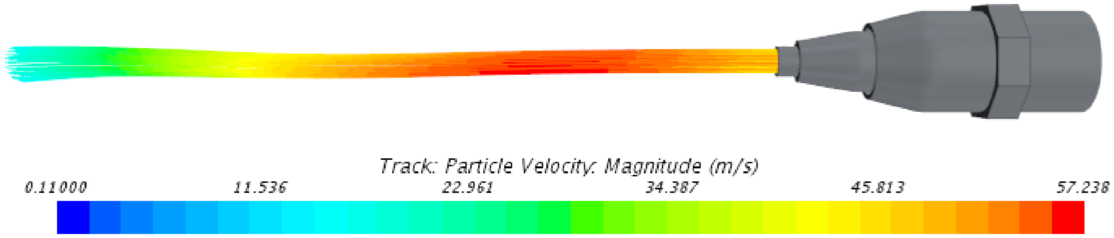

(a)

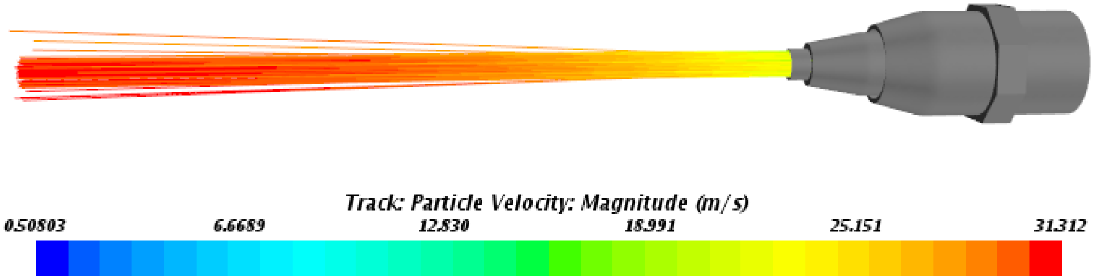

(b)

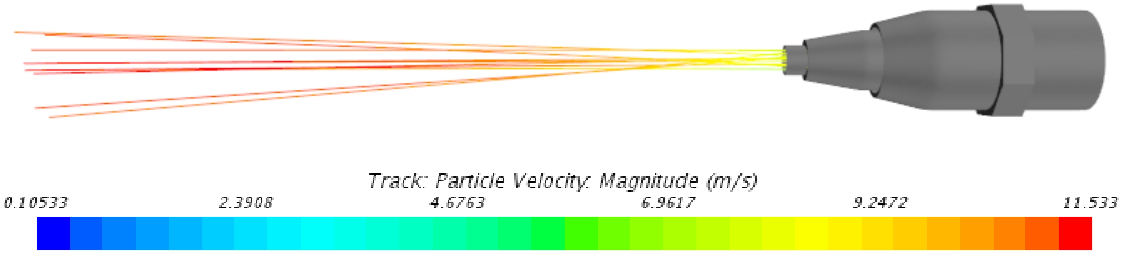

(c)

Figure 2.18: **Dry Ice Fraction =0.402: Open Boundary Maximum Velocity on Dry Ice Particles at a) 10µm b)100µm c)1000 µm**

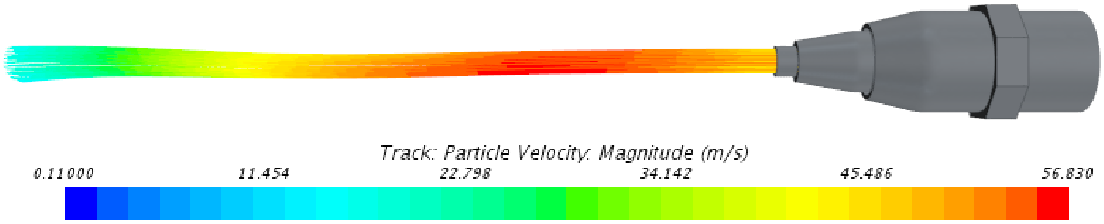

(a)

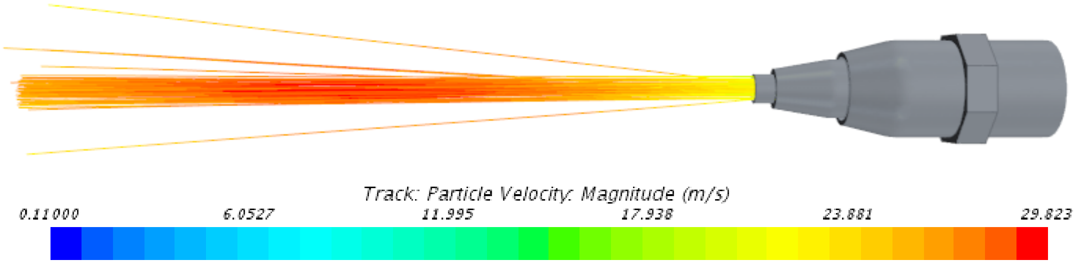

(b)

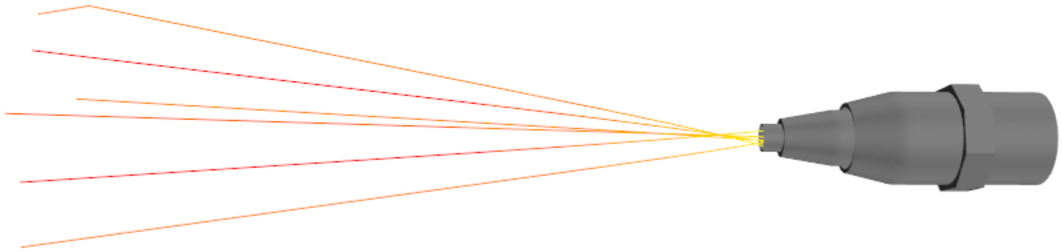

(c)

Figure 2.19: **Dry Ice Fraction =0.402: Closed Boundary Maximum Velocity on Dry Ice Particles at a) 10µm b)100µm c)1000 µm**

2.14 TRACK PARTICLE VELOCITY AND DISPERSE ANGLE PROFILE FOR a)10µm b)100µm and c)1000µm

Analysis of the 10µm particle size shows that the constant 2° disperse angle for each mass fraction of dry ice. The dry ice that comes out of the non-adjustable Coanda nozzle shows a linear pattern.

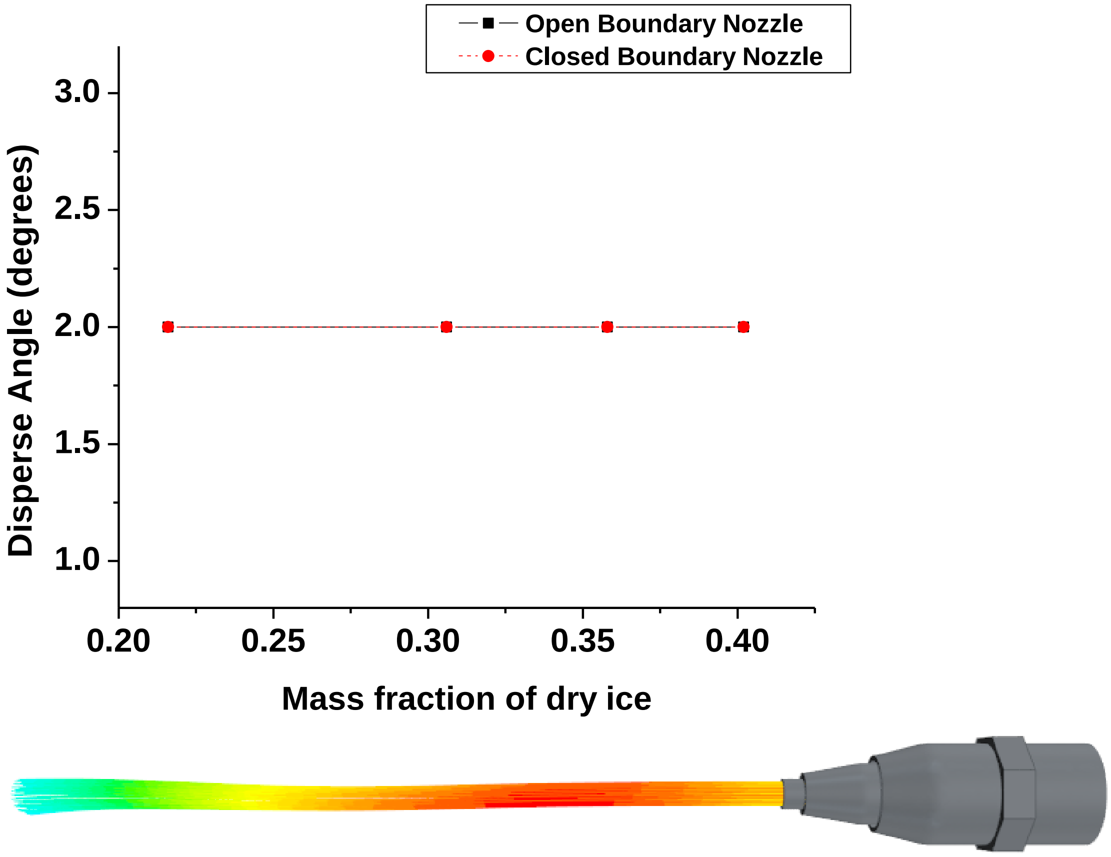

Figure 2.20: 10µm Disperse Angle and Particle Track Velocity

The 100μm particle size shows an angle increase proportional to each increase in mass fraction, with the open nozzle boundary dispersion angle slightly higher than the closed boundary. Compared to the 10μm particle size, there is a noticeable spread that allows for the dry ice to hit the surface.

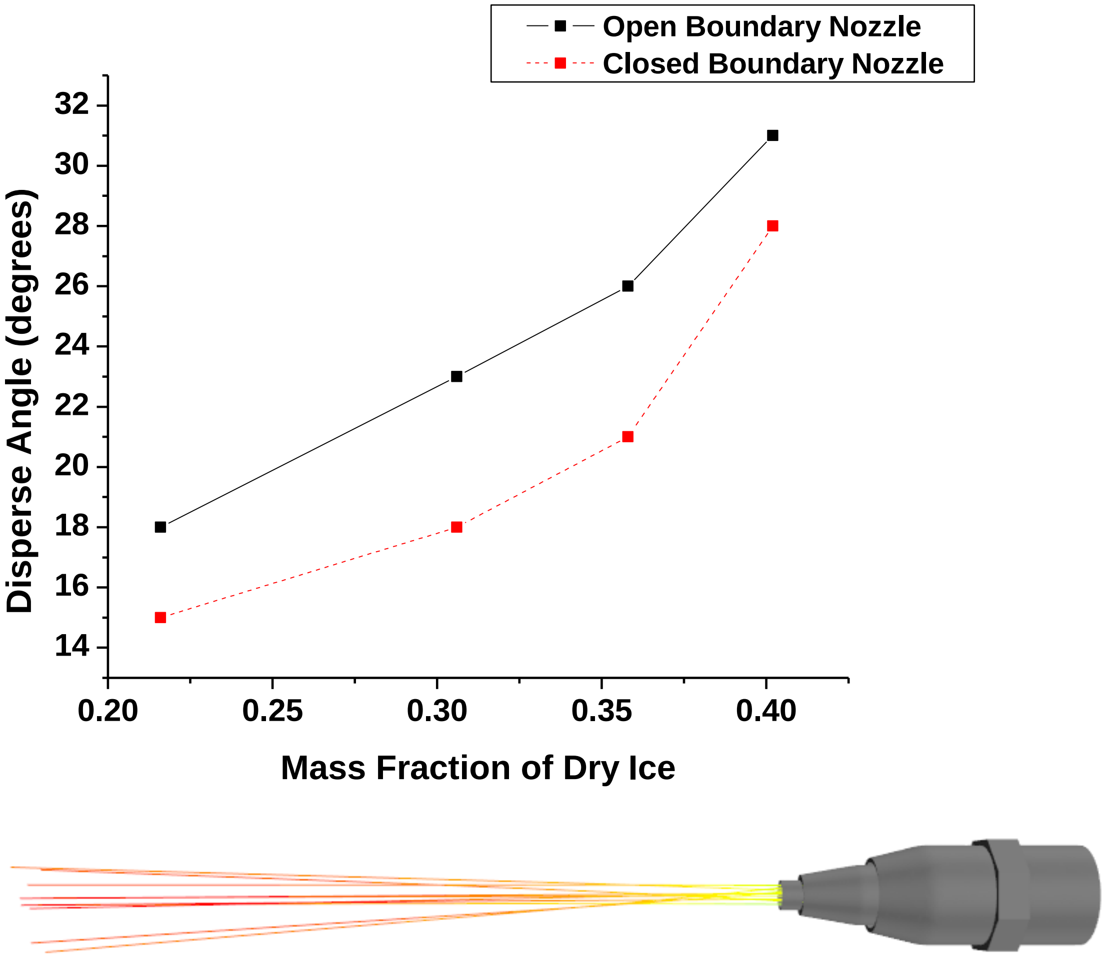

Figure 2.21: 100μm Disperse Angle and Particle Track Velocity

Analysis of the 1000μm particle size shows the largest dispersion angle and has a larger spread onto a surface. The dispersion angles increase as the mass fraction increases with open nozzle boundaries having higher dispersion angles.

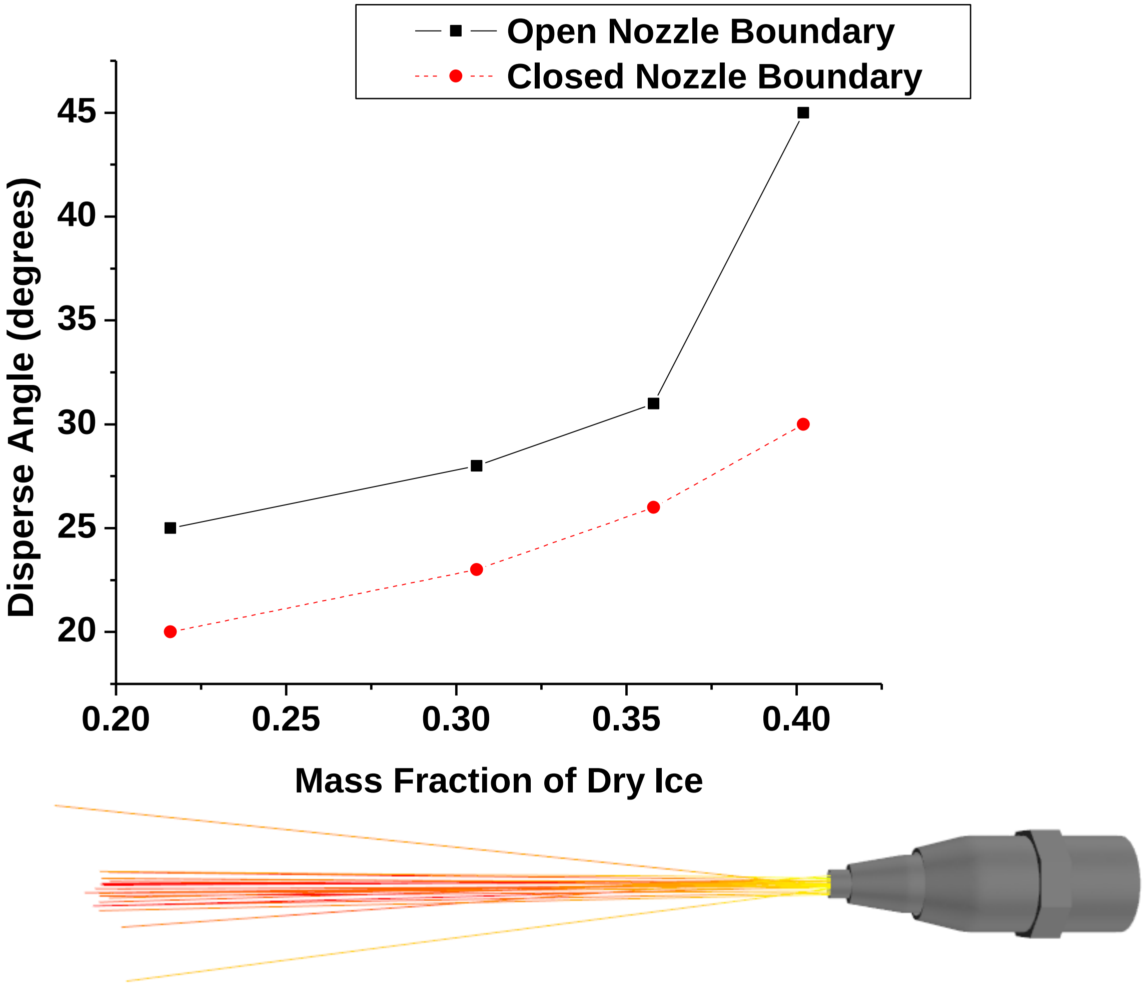

Figure 2.22: 1000µm Disperse Angle and Particle Track Velocity

2.15 TEMPERATURE DISTRIBUTION ON CLOSED AND OPEN NOZZLE BOUNDARIES AT $1\text{-}X_2=0.358$

For illustrative purposes, the temperature distribution on both the closed and open nozzle boundaries for a mass fraction of 0.358 is shown in Figure 2.23. As CO_2 vapor and air mix the overall temperature distribution decreases. Figures 2.20-22 show the temperature distribution of dry ice particles for 10, 100 and 1000 µm on the open nozzle boundary at $(1\text{-}x_2) = 0.358$. The CO_2 vapor and air distribution patterns flow in random motion within the confines of the nozzle boundary. The warmer portions are in the center which tend to decrease in temperature as it moves out. The distributions for each of the particle sizes are symmetrical in an open nozzle boundary. This occurs because the nozzle is exposed to the environment and the outer edges are in agreement with the temperature of its environment. Shown in Figure 2.23 is an environmental temperature at 283.15 K.

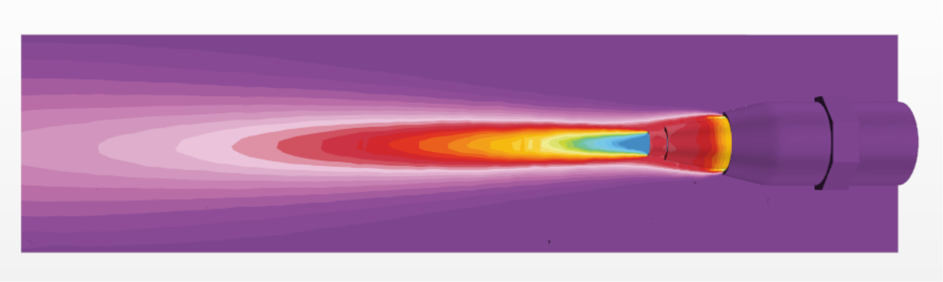

(a) 10 µm

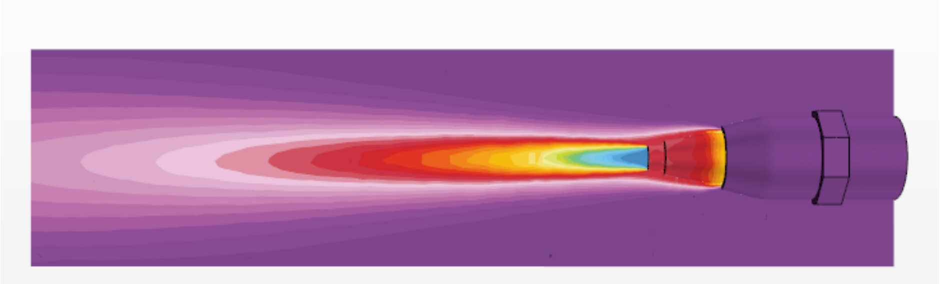

(b) 100 µm

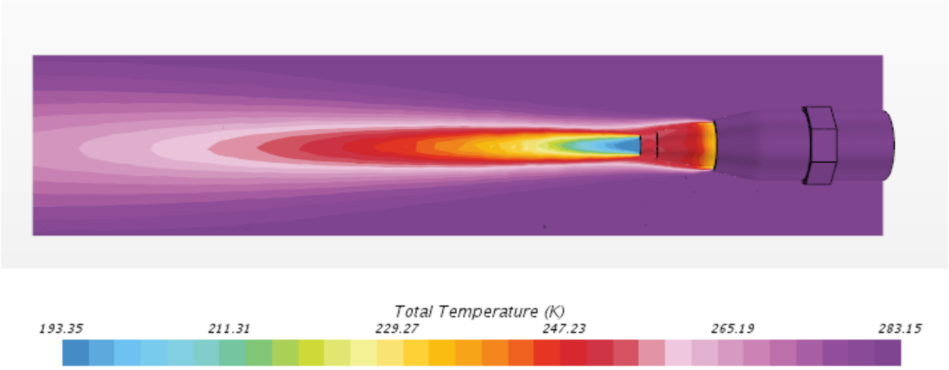

(c) 1000 µm

Figure 2.23: **Dry Ice Fraction = 0.358: Open Nozzle Boundary Temperature Distribution at a) 10µm b) 100µm c) 1000µm Particle Size**

Figure 2.24 models the temperature distribution of dry ice particles for 10, 100 and 1000µm sizes based on the closed nozzle boundary at $(1\text{-}x_2) = 0.358$ modeled at a constant temperature of 283.15 K.

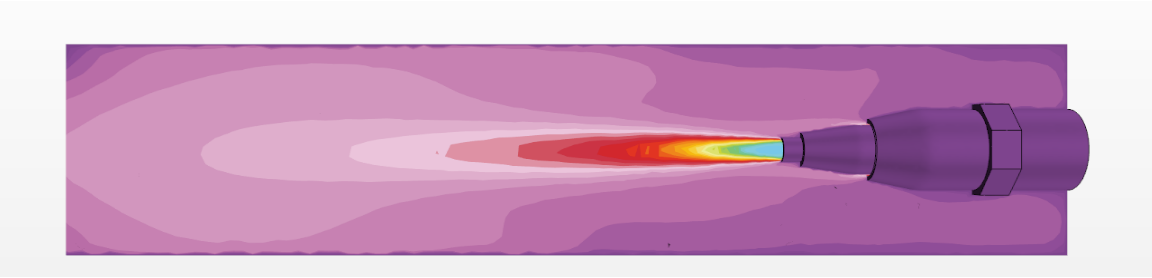

(a)10 μm

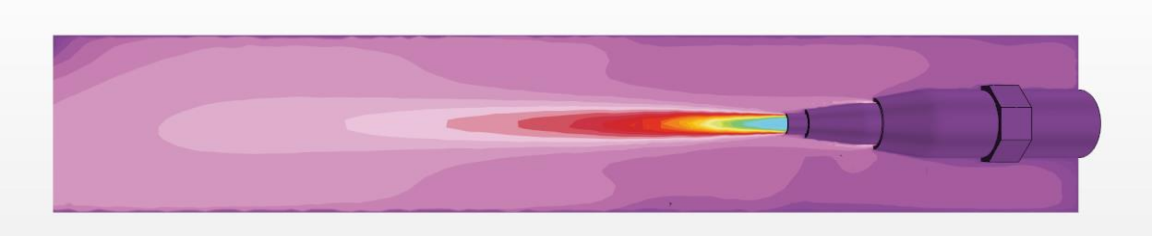

(b)100 μm

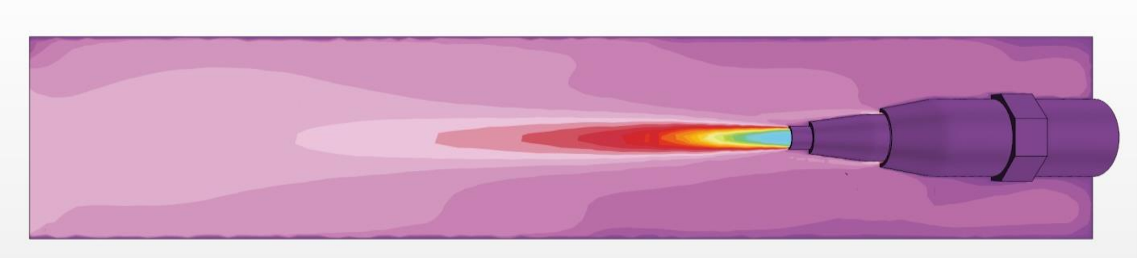

(c)1000 μm

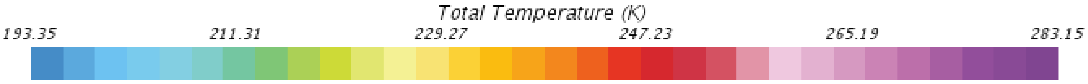

Figure 2.24: **Dry Ice Fraction = 0.358: Closed Nozzle Boundary Temperature Distribution a) 10μm b) 100μm c) 1000μm Particle Size**

CO_2 vapor and air distribution analyses show random motion within the confines of the closed nozzle boundary. Since the nozzle is enclosed, the outer edges may vary in temperature more than what is observed in the open nozzle boundary. There are also more variations in temperatures throughout the nozzle.

We now have boundary temperature distribution for both open and closed nozzle boundaries. Based on this simulation we are able to extrapolate the temperature of air and CO_2 gas.

2.16 VELOCITY VECTOR AND VELOCITY MAGNITUDE ON THE OVERALL MIXTURES OF CO_2 VAPOR AND AIR AT $1\text{-}X_2=0.358$

Figure 2.25 shows the CFD velocity vectors and velocity magnitude when both CO_2 vapor and air exit the Coanda nozzle at $(1\text{-}x_2) = 0.358$ for an open nozzle boundary at dry ice particle sizes of 10, 100 and 1000 µm.

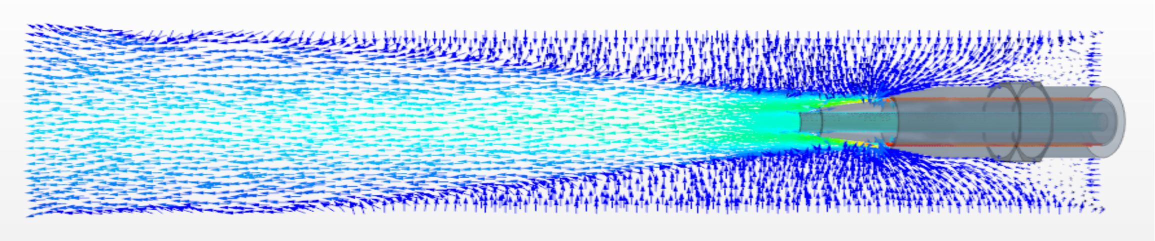

(a)10 µm

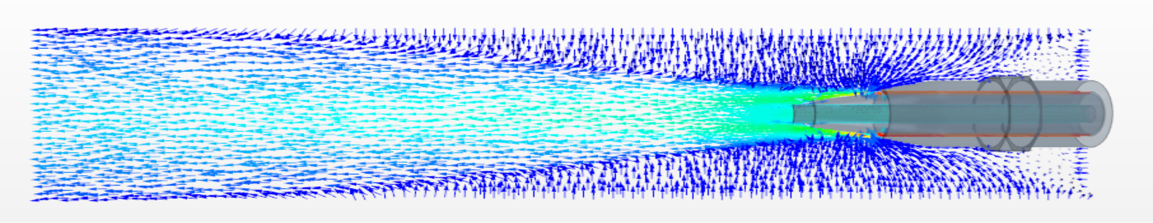

(b) 100 µm

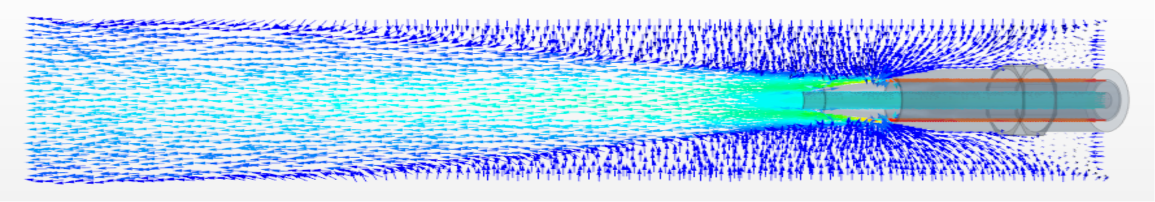

(c)1000 µm

Figure 2.25: **Dry Ice Fraction=0.358: Open Nozzle Boundary for Velocity Vector and Velocity Magnitude Of Overall Mixtures Between CO_2 Vapor And Air at a) 10µm b) 100µm and c) 1000µm particle size**

On each particle size, as air and CO_2 vapor encounter each other, the velocity decreases. Due to the presence of atmospheric pressure, there is a more concentrated flow onto the nozzle due to the atmosphere. Notice the pressure distribution on the nozzle due to the atmosphere on the open nozzle boundary. Both the CO_2 vapor and air are more concentrated along the confines of the nozzle.

Figure 2.26 shows the CFD velocity vector and velocity magnitude when the Coanda nozzle is closed to its surrounding environment at $(1-x_2) = 0.358$. Unlike the open nozzle boundary, there is less symmetry when CO_2 vapor and air exit the Coanda nozzle. Since there is no effect from the atmosphere, there is no pressure distribution directly onto the nozzle.

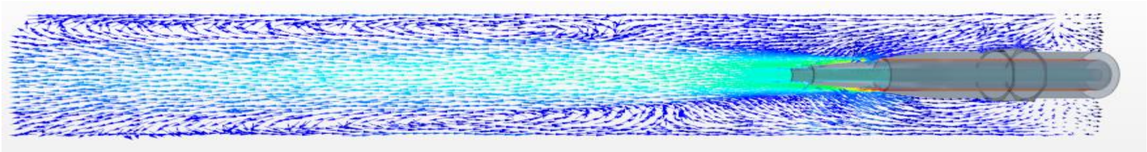

(a) 10 µm

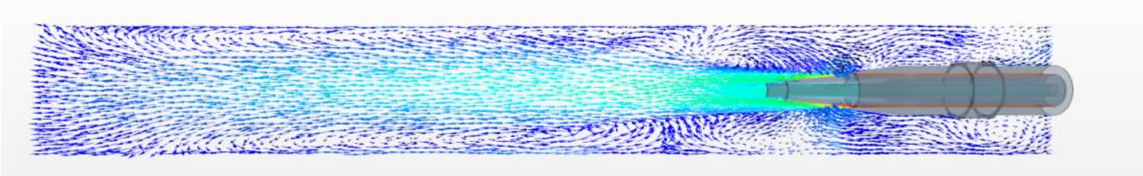

(b) 100 µm

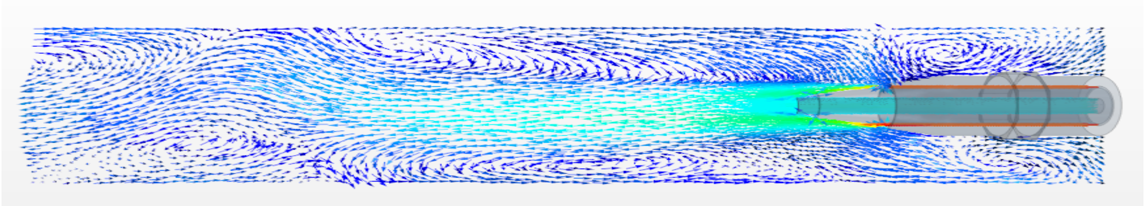

(c) 1000 µm

Figure 2.26: **Dry Ice Fraction=0.358: Closed Nozzle Boundary for Velocity Vector and Velocity Magnitude Of Overall Mixtures Between CO_2 Vapor and Air a) 10µm b) 100µm and c) 1000µm particle size**

2.17 MASS FRACTION OF AIR AND CO_2 ON AN OPEN NOZZLE BOUNDARY

The CFD simulation showing both the mass fraction for air in an open nozzle boundary is shown in Figure 2.27. In Figure 2.27a, the mass fraction of air coming out of the nozzle steadily increases from a mass fraction of 0.00 to 0.200 then to 0.400 and 0.600, ultimately resulting in solely air composing the mass. As a reault of atmospheric air, the distribution is symmetric, unlike its closed nozzle boundary counterpart. Figure 27b shows the mass fraction of CO_2 coming out of the nozzle. The mass fraction of CO_2 steadily decreases. There is no CO_2 along the boundary of its wall.

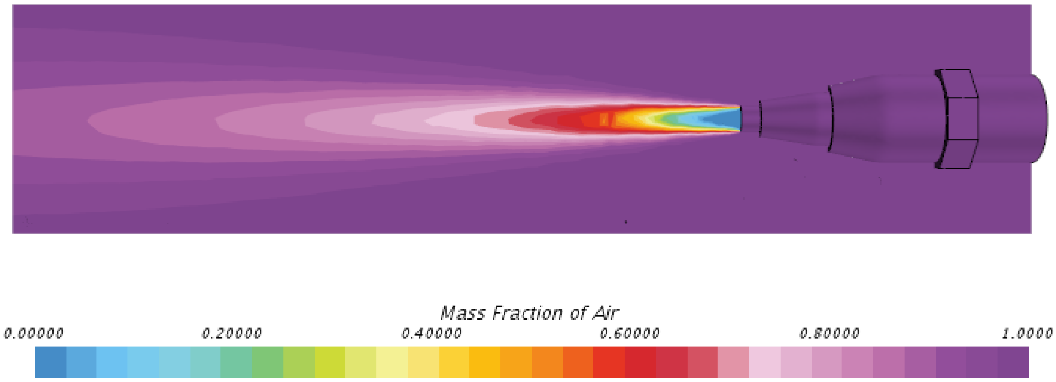

(a) Mass fraction of Air on an Open Nozzle Boundary

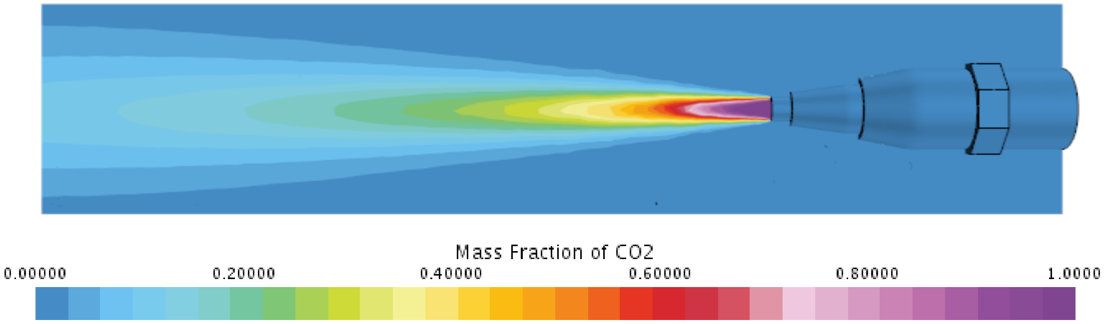

(b) Mass fraction of CO_2 on an Open Nozzle Boundary

Figure 2.27: **Mass fraction of Air and CO_2 vapor on an Open Nozzle Boundary**

2.18 MASS FRACTION OF AIR AND CO_2 ON A CLOSED NOZZLE BOUNDARY

The CFD simulation showing both the mass fraction for air and CO_2 on a closed nozzle boundary in shown in Figure 2.28. In Figure 2.28a, the mass fraction of air coming out of the nozzle steadily increases from a mass fraction of 0.00 to 0.200 then to 0.400 and

0.600, ultimately resulting in only air being present. Figure 2.28b shows the mass fraction of CO_2 coming out of the nozzle. The mass fraction of CO_2 steadily decreases. There is no CO_2 along the boundary of its wall.

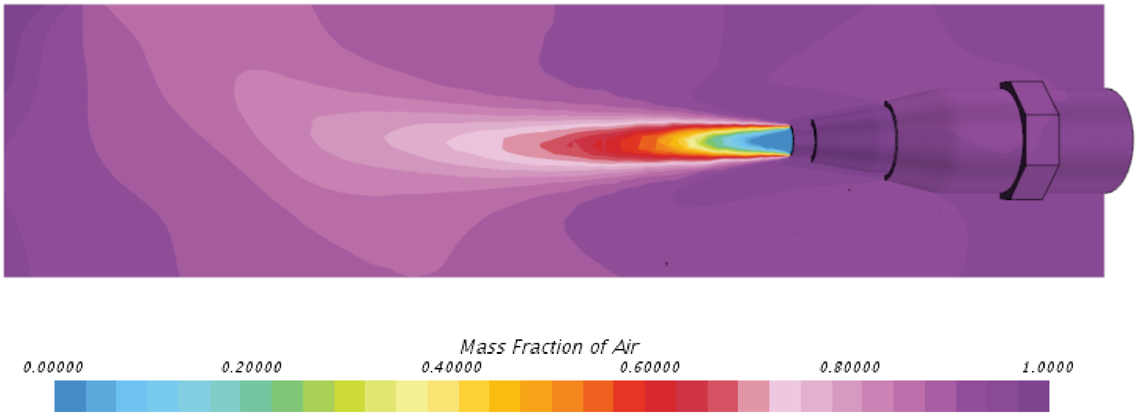

(a)Mass fraction of Air on a Closed Nozzle Boundary

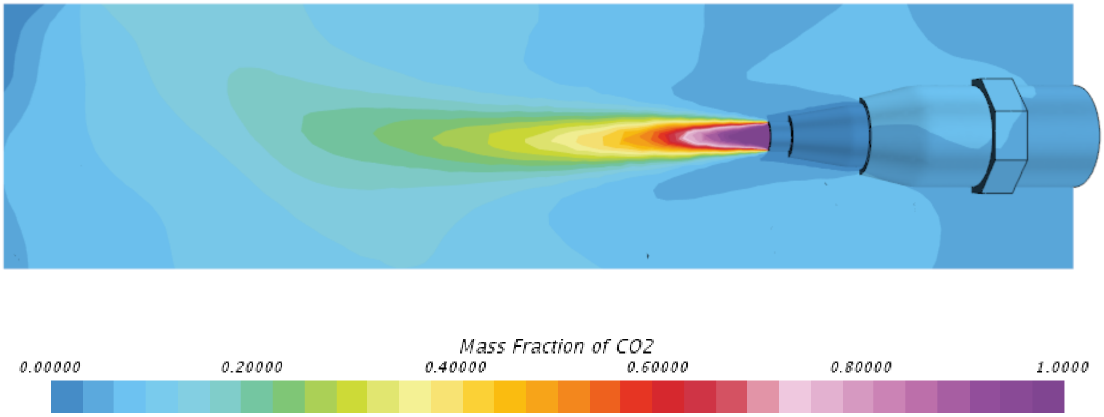

(b)Mass fraction of CO_2 on a Closed Nozzle Boundary

Figure 2.28: **Mass fraction of Air and CO_2 vapor on a Closed Nozzle Boundary**

2.19 NEW KNOWLEDGE FROM MULTI-PHASE MODELING THROUGH A NON-ADJUSTABLE COANDA NOZZLE

Multi-phase computational fluid dynamics (CFD) have been modeled on a non-adjustable Coanda nozzle for the purposes of optimizing process parameters, which include the temperature of the liquid CO_2 supply, the mass fraction of dry ice ($1\text{-}x_2$), the mass flow rate, and the pressure and nozzle and air configuration.

Thermodynamic and process variable information, which were not initially known on a non-adjustable Coanda spray-nozzle system, have been identified as turbulent flow. A 3-D CFD model for spray-freezing has been developed on the Coanda nozzle at 195K and atmospheric pressure (1atm). The mass fraction for both dry ice and CO_2 vapor were determined from the energy balance equation, as described in this chapter. A comparative study on exposure of Coanda nozzle closed and open boundaries to the atmosphere have been compared. Pressure, temperature and mass fraction profiles for each particle size and boundary are now modeled.

The ability to cool a substrate is dependent upon the inlet temperature. This work has provided us with a model as to what the inlet nozzle temperature would be required to lay down a fair amount of dry ice on a carpet or mattress. As the mass fraction of dry ice increases, the dispersion angle and velocity increases. Supporting data for each specific mass studied, 10µm, 100µm, and 1000µm, have been calculated and recorded at specific mass fractions. We now have a knowledge base to inform how much spread a particular dry ice particle size may achieve when hitting a mattress or carpet in the context of a dispersion angle. This work provides an analytical model on two nozzle boundaries. In addition, this study provides a basis for optimizing dispersion angles, temperature, velocity, and mass fraction on any non-adjustable Coanda nozzle.

CHAPTER 3: PHASE EQUILBIRIUM OF MAJOR COMPONENTS OF ESSENTIAL OILS IN LIQUID AND SUPERCRITICAL CARBON DIOXIDE

3.1 MOTIVATION

CarboNix is an innovative company that also seeks to employ a new mechanism to kill, dislodge and remove dust mites from surfaces. This mechanism also applies an acaricide, such as an essential oil, to impede re-infestation. As mentioned previously, research shows that essential oils, such as tea tree oil, have the capacity to act as natural dust mite killers, and to prevent re-infestation. Figure 2.1 shows the CarboNix truck where liquid CO enters the Coanda nozzle and exits as a mixture of dry ice and gaseous CO_2. Figure 3.1, shows this process including the injection of an essential oil onto the CO_2 spray line. The process is improved by applying both dry ice and essential oil spray onto the carpet.

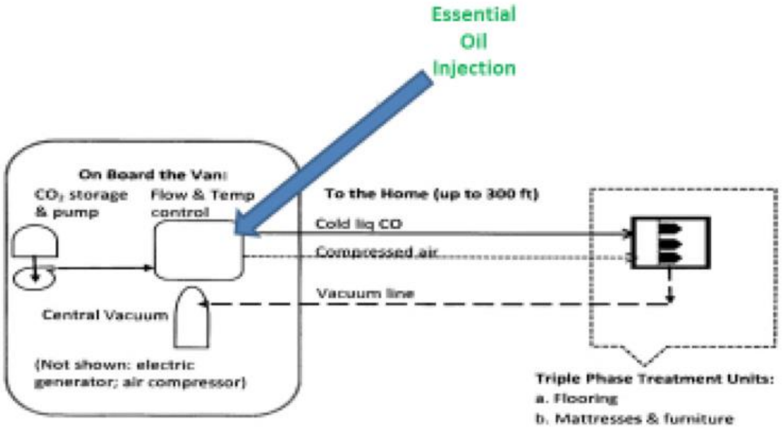

Figure 3.1: **Essential Oil Injection**

3.2 LITERATURE REVIEW ON SOLUBILITY METHODS

3.2.1 THE STATIC SYNTHETIC METHOD

There are two methods used to measure solubility, the static synthetic method and the dynamic method. Figure 3.2 shows the stages of the solubilization process using the static synthetic method. In the static method, a mixture of known composition is introduced into a variable volume cell used for adjusting operating volume and pressure. The vessel is equipped with a sapphire window for visual observations. A fixed amount of solute is dissolved into a known amount of supercritical fluid. Experiments are conducted at a fixed temperature, volume, and pressure and then adjusted to gradually reduce the solubility of the solute causing precipitation. The beginning of the precipitation is called the cloud point and is recorded as a measure of solubility (46).

Solubility data can then be fit and modeled. In the case of orange essential oils, both the Peng-Robinson and Soave-Redlich-Kwong (47) cubic equations of state were employed. The authors used van der Waals mixing rules and experimental data to fit two interaction parameters in these equations of state.

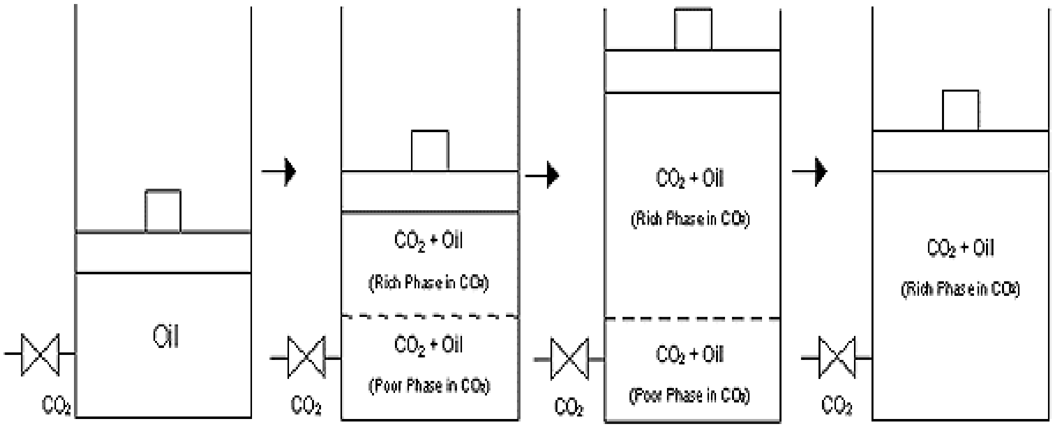

Figure 3.2: **Stages of solubilization process of essential oil sample in carbon dioxide at constant temperature and pressure (47)**

Solubility was measured for orange oil in CO_2 with the static synthetic method (47). The results analyzed the solubility range of orange essential oil in CO_2 at 308.15 K for pressures ranging from 50 to 70bar. The solubility varied from 1.7 ± 0.1 to 3.6 ± 0.1mg/g.

Figure 3.3 shows modeling results for both the Peng-Robinson (PR) and Soave-Redlich-Kwong (SRK) equation of states. Orange essential oil solubility (EOS) in carbon dioxide was determined as a function of pressure for a temperature of 308.15 K using orange essential oil composition. Results were performances similar to that of SRK EOS.

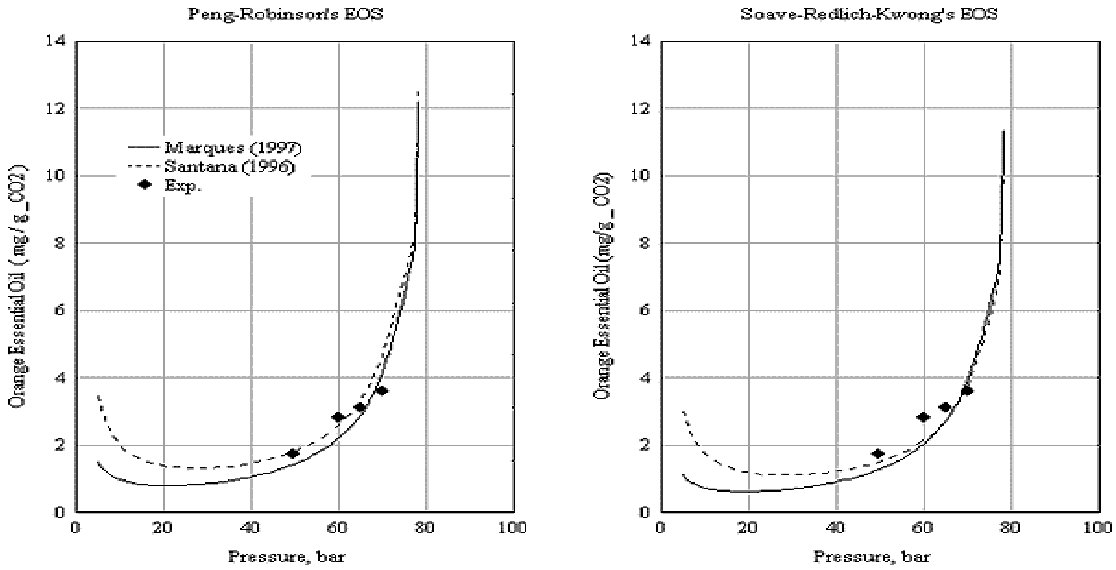

Figure 3.3: **Predicted solubility of orange essential oil in CO_2 according to PR and SRK equations of state (47)**

3.2.2 THE DYNAMIC FLOW METHOD

Francisco and Sivik (48) measured the solubility of 1, 8-cineole, α-pinene, limonene, and mixtures thereof in supercritical fluids with CO_2. They also measured solubility of extract of eucalyptus leaf oils using the dynamic method. In the dynamic method there is a continuous flow of a supercritical fluid or a fluid mixture through a vessel filled with a solute. The flow rate is sufficiently slow that the outer stream is assumed to reach equilibrium. The outlet is then analyzed for the solute concentration by chromatographic, spectroscopic, gravimetric, dielectric or other techniques (46). Francisco and Sivik (48) conducted experiments at pressures of 80, 100, 150, and 250 bar. Constant temperatures of 40 and 60 °C were assessed at each pressure. The results showed that there was an increase in the solubility of all oils with an increase in pressure and decrease in temperature (Figure 3.4). The mixtures of both pure components (Figure 3.5) as well as the eucalyptus oil extracts exhibited lower solubility than the pure single oil components in the same conditions (48). Figure 3.4 shows α-pinene, 1, 8-cineole and limonene at 40° and 60°. Figure 3.5 shows 1, 8-cineole/α-pinene (CP), 1, 8-cineole/limonene (CL) and 1, 8-cineole/limonene/α-pinene (CLP) at 40° and 60 °C.

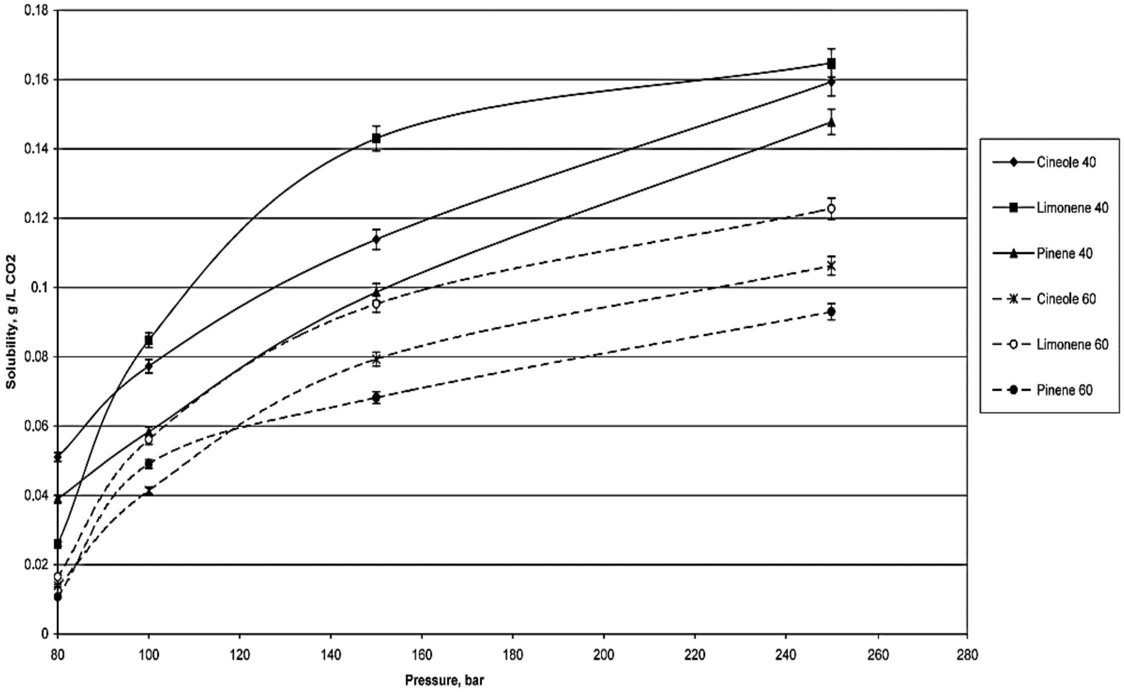

Figure 3.4: **Pressure dependence of solubility of pure terpenes α-pinene, 1, 8-cineole and limonene at 40 and 60°C (48)**

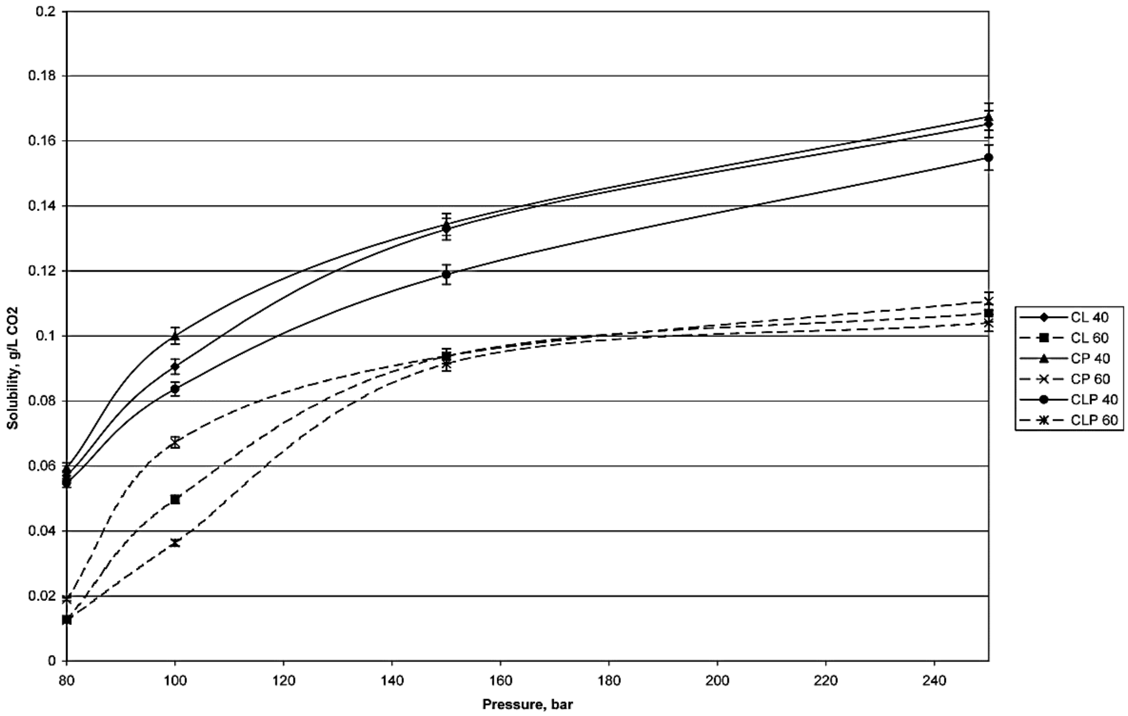

Figure 3.5: **Pressure dependence of solubility of mixtures of pure terpenes CL, CP, and CPL at 40 and 60°C.(48)**

3.3 GAS CHROMATOGRAM AND MASS SPECTRUM OF TEA TREE OIL

The major constituent of each of the three oils were determined by gas chromatography (GC) and mass spectroscopy (MS). A HP (Hewlett Packard, USA) 5890 GC apparatus with an on-column injection was used. The column was 30 m x 0.53 mm internal diameter x 1.5μm film thickness. Helium was the carrier gas and the injector temperature 250°C. The injected sample volume was 2μL. The column oven temperature was programmed from 50°C to 200°C and ramped at 1°C/minute with a final hold at 200°C for 1 minute. The total analysis time was 16 minutes. A VG-705 mass spectrometer was used at Electron Ionization (EI) mode. The ionization voltage was determined to be 70 eV and the scan range was from 50-450 Da. The chemical structure of each constituent was identified by comparing mass data of their peaks with standard library data (49).

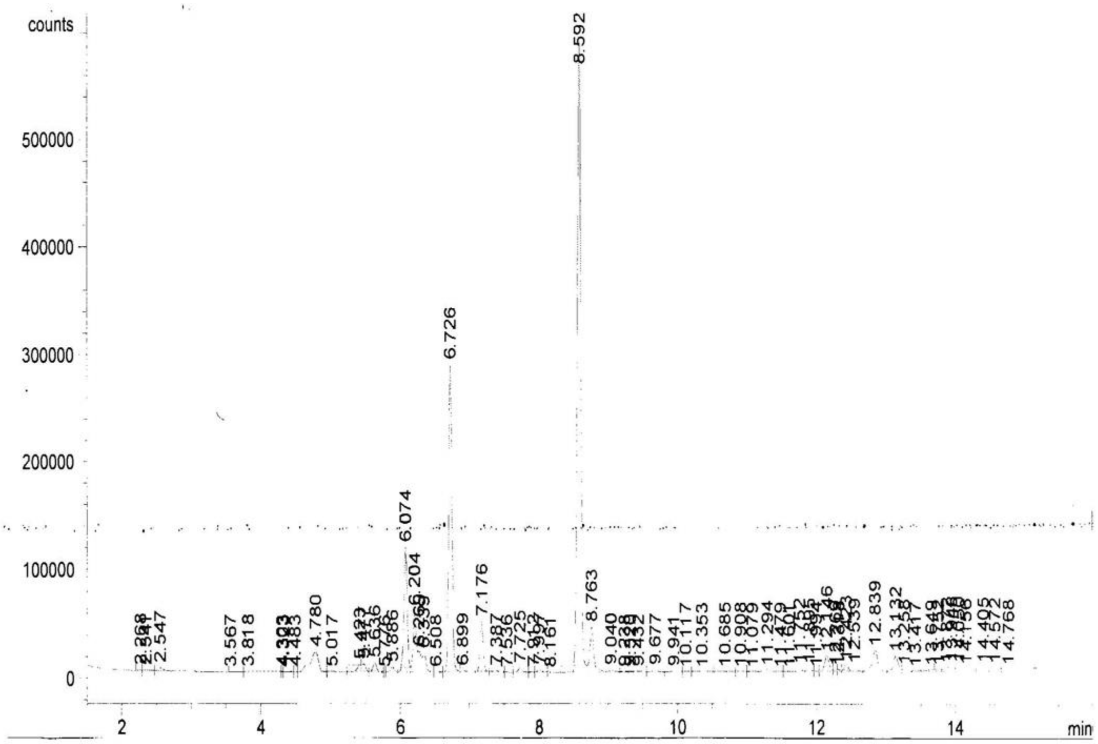

Figure 3.6: **Gas Chromatogram for Tea Tree Oil**

Figure 3.6 shows the gas chromatogram for tea tree oil. Area counts versus time in minutes were plotted. The highest peak occurs at 8 minutes and 59 seconds. Mass spectroscopy confirms the major component of tea tree oil as terpinen-4-ol.(50) This is confirmed in Table 3.1, which reveals the highest area and area count coming from the GC confirms terpinen-4-ol.

Table 3.1: **Three most dominant components in tea tree oil**

Parts per million (ppm) in Ethanol	**Area Count**	**Component**
100	3,787	α-Terpinene
100	8,840	γ-Terpinene
100	17,960	Terpinen-4-ol
10,000	396,190	α-Terpinene
10,000	922,431	γ-Terpinene
10,000	2,069,230	Terpinen-4-ol

Mass spectroscopy confirms the major component of tea tree oil as terpinen-4-ol (49) shown in Figure 3.7.

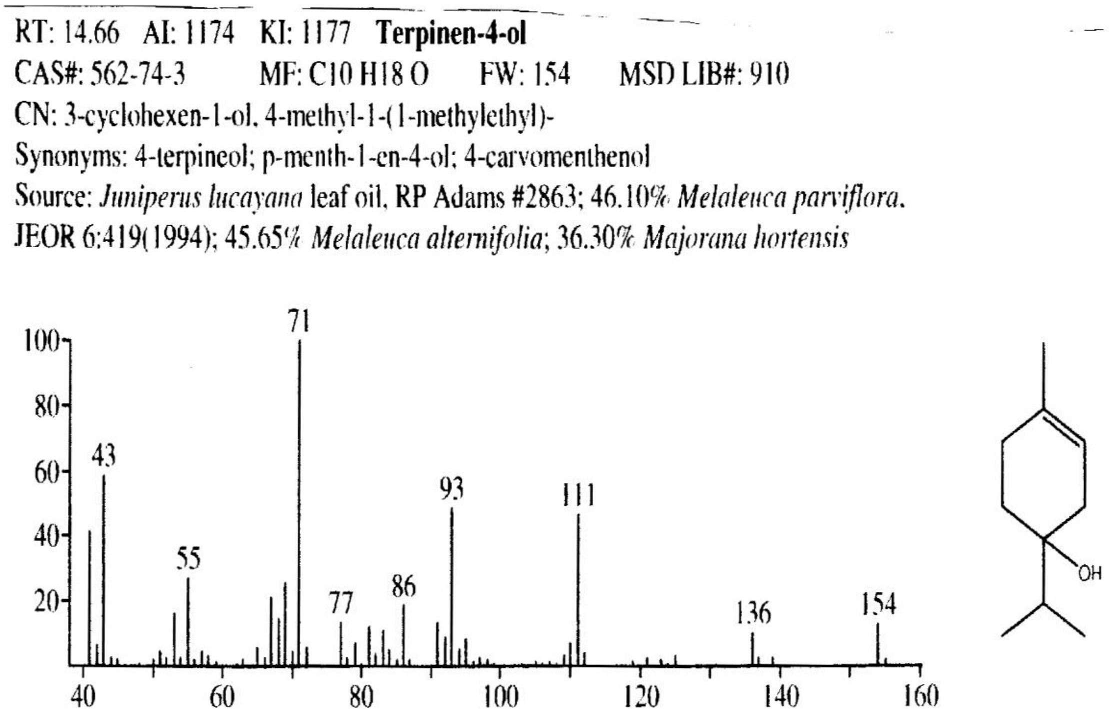

RT: 14.66 AI: 1174 KI: 1177 **Terpinen-4-ol**
CAS#: 562-74-3 MF: C10 H18 O FW: 154 MSD LIB#: 910
CN: 3-cyclohexen-1-ol, 4-methyl-1-(1-methylethyl)-
Synonyms: 4-terpineol; p-menth-1-en-4-ol; 4-carvomenthenol
Source: *Juniperus lucayana* leaf oil, RP Adams #2863; 46.10% *Melaleuca parviflora*, JEOR 6:419(1994); 45.65% *Melaleuca alternifolia*; 36.30% *Majorana hortensis*

Figure 3.7: **Mass Spectrum for Terpinen-4-ol (49).**

3.3.1 TERPINEN-4-OL STRUCTURE

The structure for terpenin-4ol is shown in Figure 3.8. Terpenin-4-ol has a molecular formula $C_{10}H_{18}O$, a molar mass of 154.3 g/mol and a density of 0.933 g/mL.

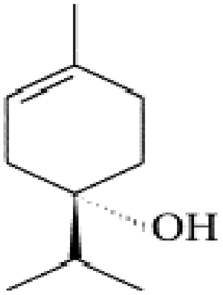

Figure 3.8: **Terpinen-4-ol structure (51)**

The hydroxyl (OH) group terpinen-4-ol makes it slightly soluble in water. With a density of 0.933 g/mL. γ-terpinene and α-terpinene represent the next two highest peak componentsin tea-tree oil.

3.4 GAS CHROMATOGRAM AND MASS SPECTRUM FOR CEDARWOOD OIL

Figure 3.9 shows the gas chromatogram for cedar wood oil. Area counts versus time in minutes were plotted. Gas chromatography shows the most abundant component in cedar wood oil peaks at 11.12 minutes.

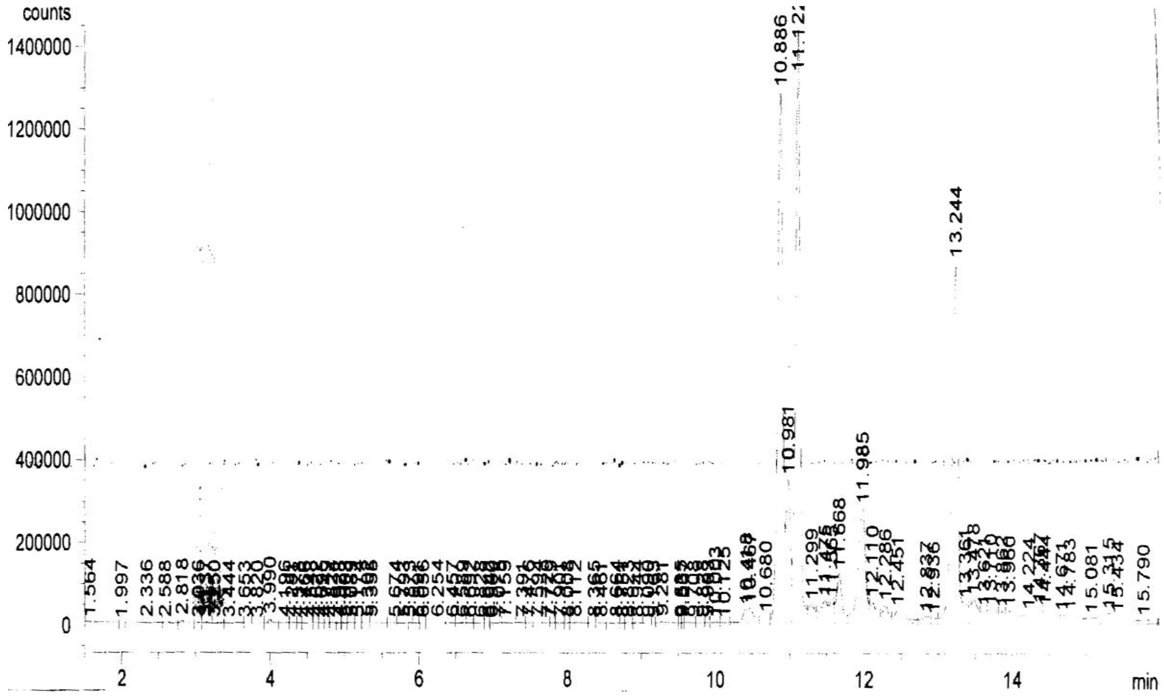

Figure 3.9: **Gas chromatogram for cedar wood oil**

Mass spectrometry identifies the most abundant component as α-cedrene (49) shown in Figure 3.10.

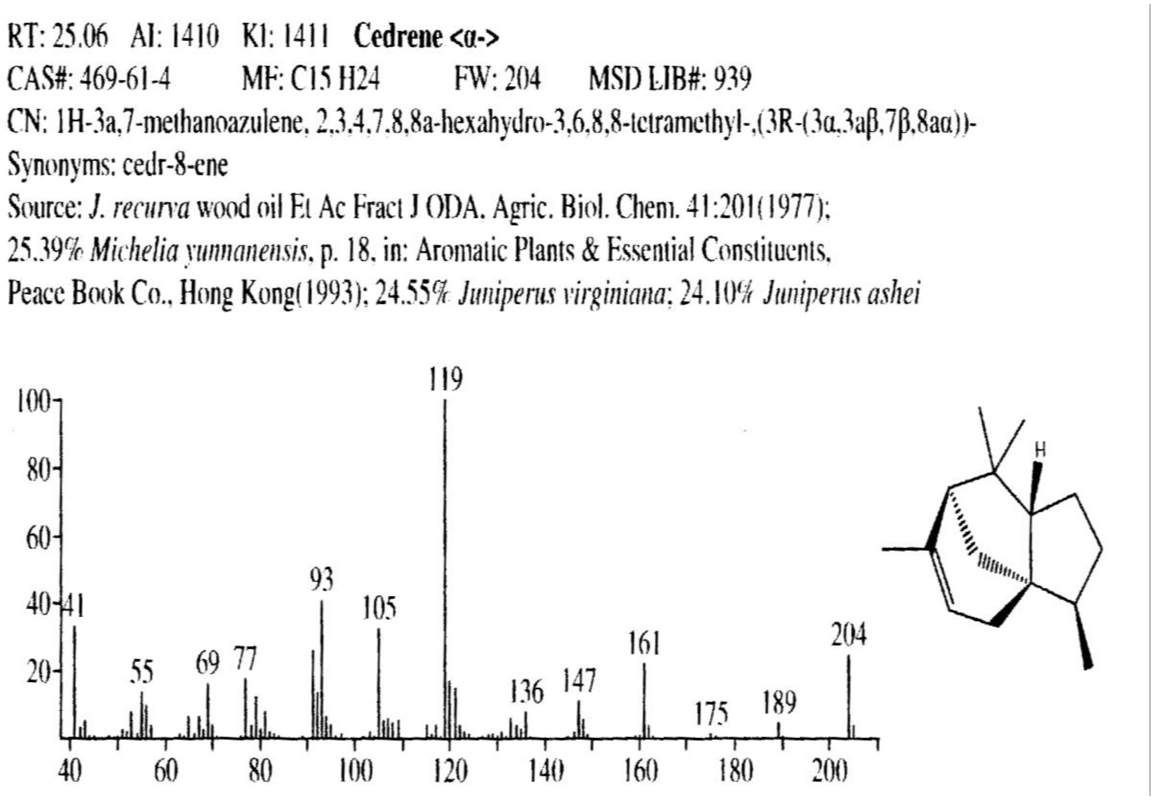

RT: 25.06 AI: 1410 KI: 1411 **Cedrene <α->**

CAS#: 469-61-4 MF: C15 H24 FW: 204 MSD LIB#: 939

CN: 1H-3a,7-methanoazulene, 2,3,4,7,8,8a-hexahydro-3,6,8,8-tetramethyl-,(3R-(3α,3aβ,7β,8aα))-

Synonyms: cedr-8-ene

Source: *J. recurva* wood oil Et Ac Fract J ODA. Agric. Biol. Chem. 41:201(1977);

25.39% *Michelia yunnanensis*, p. 18, in: Aromatic Plants & Essential Constituents,

Peace Book Co., Hong Kong(1993); 24.55% *Juniperus virginiana*; 24.10% *Juniperus ashei*

Figure 3.10: **Mass Spectrometry for cedar wood oil (49).**

3.4.1 α-CEDRENE STRUCTURE

The structure for α-cedrene is shown in Figure 3.11. α-cedrene has a molecular formula of $C_{15}H_{24}$, a molar mass of 204.4 g/mole, and a density of 0.932 g/mL.

Figure 3.11: **α-cedrene Structure (52)**

Thujopsene and cedrol are the next most prevalent components of cedar wood oil.

3.5 GAS CHROMATOGRAM AND MASS SPECTRUM FOR HINOKI OIL

Figure 3.12 shows the gas chromatogram for hinoki oil. Area counts versus time in minutes were plotted and the largest peak occurs at 4 minutes.

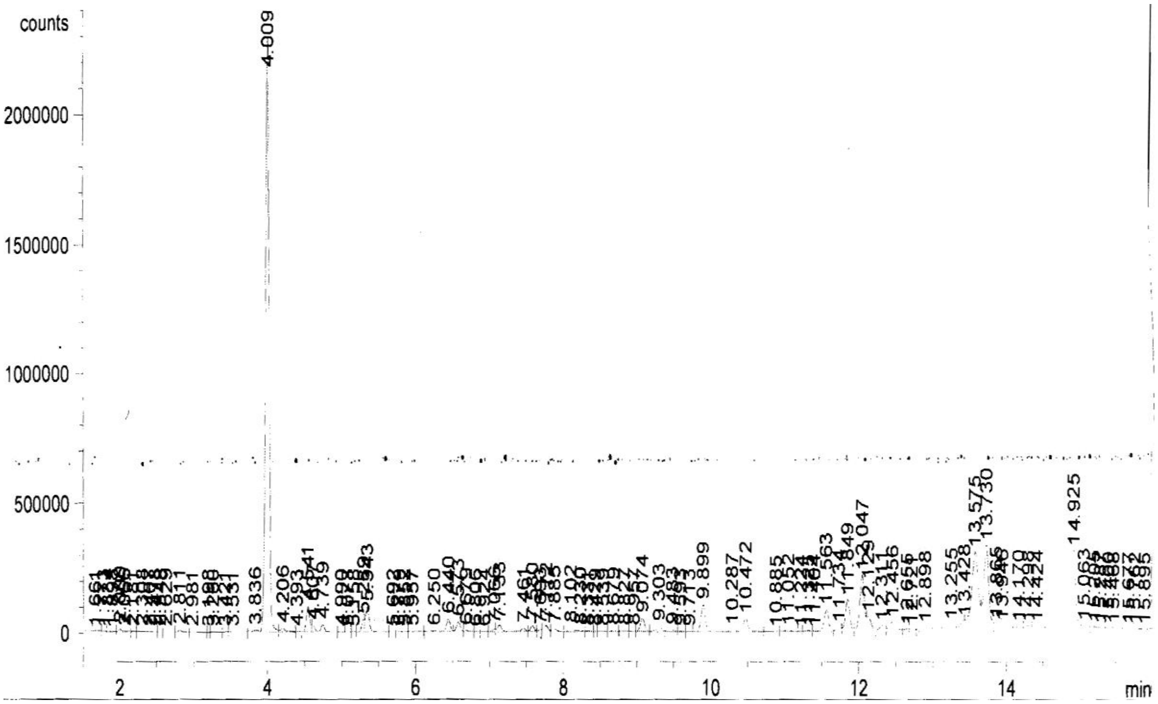

Figure 3.12: **Mass Chromatogram for Hinoki Oil**

The mass spectrum in Figure 3.13 shows the most abundant component to be α-pinene (49).

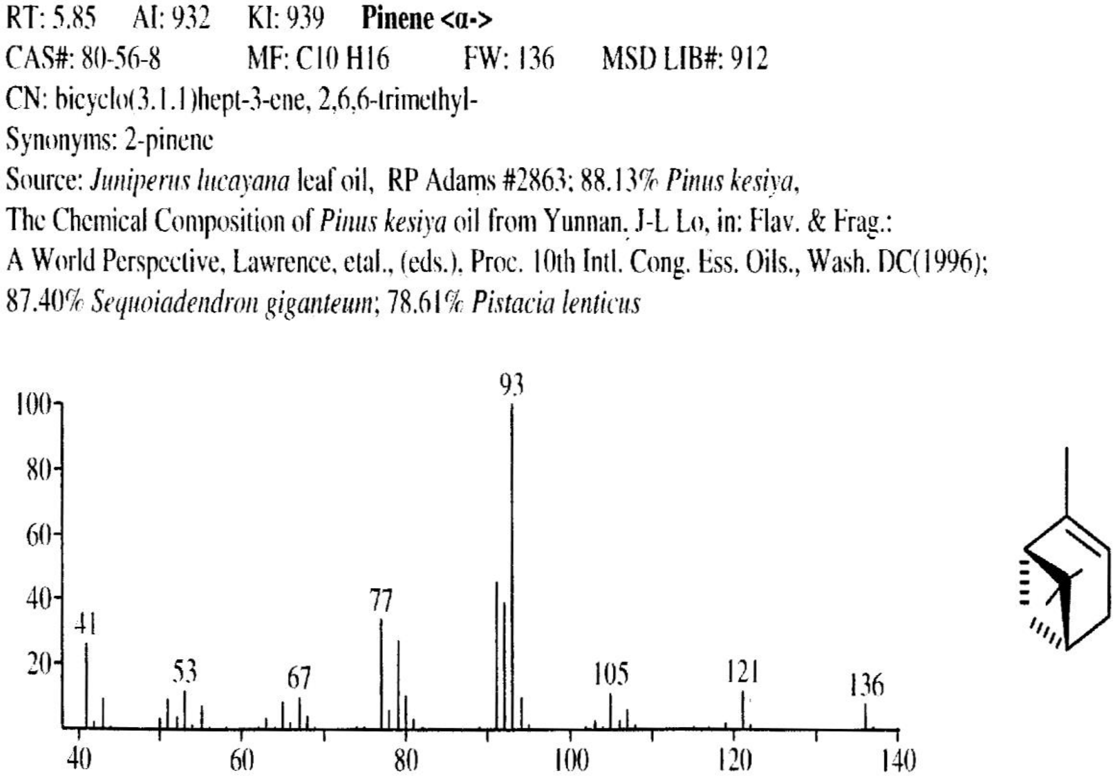

RT: 5.85 AI: 932 KI: 939 **Pinene <α->**
CAS#: 80-56-8 MF: C10 H16 FW: 136 MSD LIB#: 912
CN: bicyclo(3.1.1)hept-3-ene, 2,6,6-trimethyl-
Synonyms: 2-pinene
Source: *Juniperus lucayana* leaf oil, RP Adams #2863; 88.13% *Pinus kesiya*,
The Chemical Composition of *Pinus kesiya* oil from Yunnan, J-L Lo, in: Flav. & Frag.:
A World Perspective, Lawrence, etal., (eds.), Proc. 10th Intl. Cong. Ess. Oils., Wash. DC(1996);
87.40% *Sequoiadendron giganteum*; 78.61% *Pistacia lenticus*

Figure 3.13: **Mass Spectrometry for hinoki oil (49).**

3.5.1 α- PINENE STRUCTURE

α-pinene has a molecular formula $C_{10}H_{16}$, a molar mass of 136.2 g/mole, and a density of 0.858 g/mL. The structure for α-pinene is shown in Figure 3.14.

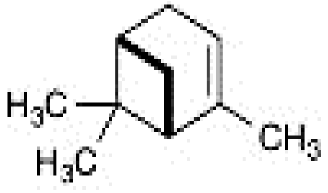

Figure 3.14:**Structure for α-pinene (2)**

As compared to tea-tree and cedar wood oil, hinoki oil is less volatile. Camphene and β-myrcene are the two next most prevalent components in hinoki oil.

3.6 CRITICAL CONSTANTS AND ACENTRIC FACTOR

Experimental information on the physical properties of essential oil components are scarce in the literature (47). Sousa et.al (53) reports the critical constants and acentric factor for terpinen-4-ol as $T_c=754.3\text{K}$, $P_c=33.2$ bar and $\omega=0.509$. For α-pinene, is the calculations reported $T_c=644.0$ K, $P_c=27.7$ bar and $\omega=0.221$. The critical temperature, critical pressure, and acentric factor have not been reported for α-cedrene; thus, properties were estimated using the Joback contribution method.

3.6.1 JOBACK CONTRIBUTION METHOD FOR ALPHA-CEDRENE

Group contributions for α-cedrene are as follows:

>C<(ring)	2 groups
$-CH_3$	4 groups
>CH-(ring)	4 groups
$-CH_2$-(ring)	3 groups
=CH- (ring)	2groups
=C	1 group

Joback Group Contributions for boiling point, critical points, critical pressure and acentric factor are tabulated as follows in Table 3.2 where *tck*, *pck* and *wck* represent specific temperature, pressure and acentric factor group contributions, respectively.

Table 3.2: **α-cedrene Group Contribution**

Group *k*	**N_k**	**$N_k(tbk)$**	**$N_k(tck)$**	**$N_k(pck)$**	**$N_k(wck)$**
>C<(ring)	2	42.64	0.0084	0.0122	-0.702
$-CH_3$	4	94.32	0.0564	-0.0048	1.184
>CH-(ring)	3	65.34	0.0366	0.0012	-0.213
$-CH_2$-(ring)	4	108.60	0.040	0.010	0.588
=CH- (ring)	1	26.73	0.0082	0.0011	0.252
=C	1	31.01	0.0143	0.0008	-0.210
$\sum_{k=i}^{6} N_k F_k$		368.64	0.1639	0.0205	0.899

Poling et. al.(54) estimated the boiling point, critical temperature, critical pressure and acentric factor as follows:

$$T_B(\mathrm{K}) = 198 + \sum_k N_k(\mathrm{tbk})$$

$$T_B(\mathrm{K}) = 198 + 368.64 = 566.64\ \mathrm{K}$$

$$T_c\ (\mathrm{K}) = \frac{T_b}{0.584+0.965\,\{\sum_k N_k\ (tck)\} - \{\sum_k N_k{}^2\ tck^2\}}$$

$$T_c\ (\mathrm{K}) = \frac{566.64}{0.584+0.965(0.1639)-0.1639\text{^}2} = 792.2\ \mathrm{K}$$

$$\omega = 0.4085\{ln[\sum N_k(\mathrm{w1k}) + 1.1507]\}^{1/0.505}$$

$$\omega = 0.4085\ (\ln[(0.899) + 1.1507]\text{^}1.98$$

$$\omega = 0.212$$

$$P_c\ (\mathrm{bar}) = \left[\frac{1}{0.113+0.0032N_{atoms} - \sum N_{k\ (pck)}}\right]^2$$

Where N = the number of atoms. α-cedrene has 39 atoms

$$P_c\ (bar) = \left[\frac{1}{0.113+0.0032(39)-0.0205}\right]^{2} = 21.2\ \mathrm{bar}$$

The critical properties for each pure component are tabulated in Table 3.3.

Table 3.3 **PR-EOS Parameters**

Substance	**T_c(K)**	**P_c(bar)**	**ω**
CO_2	304.2	73.7	0.225
Terpinen-4-ol	754.3(53)	33.2(53)	0.509(53)
α-cedrene	792.2	21.2	0.212
α-pinene	644.0(53)	27.7(53)	0.221(53)

3.7 BINARY INTERACTION PARAMETERS

3.7.1 FATEEN VALIDATION FOR K_{12} IN LIQUID AND SUPERCRITICAL CO_2

The PR-EOS requires a binary interaction parameter for each component. Different methods have been suggested in the literature to estimate these parameters, but estimates may fail to predict the complex phase behavior at high pressures (55). In this work, the binary interaction parameter was computed (55) for each component in CO_2 using the following equation:

$$k_{12} = 1 - \frac{1}{2}\frac{b_2}{b_1}\sqrt{\frac{a_1}{a_2}} - \frac{1}{2}\frac{b_1}{b_2}\sqrt{\frac{a_2}{a_1}} + \frac{1}{2}\frac{b_2 RT}{\sqrt{a_1 a_2}}\frac{\theta_1}{T_{r1}^{\theta_2} P_{r1}^{\theta_3}} \quad (2)$$

where *a* and *b* are the standard PR-EOS parameters. θ_1, θ_2 and θ_3 are adjustable parameters for carbon dioxide/aromatics and k_{12} is the binary interaction parameter. The subscript 1 represents the solvent (CO_2) and 2 the solute (essential oil). The values of the adjustable parameters for carbon dioxide/aromatics have been fitted for $\theta_1 = 1.0531$, $\theta_2 = 0.97216$ and $\theta_3 = 0.049409$ (55). To validate this scheme, we applied the PR-EOS with equation (2) to the system CO_2 + d-limonene, for which data are available in the literature (41). Validation of this correlation for the CO_2 + d-limonene system agrees with the literature as shown in

Table 3.4. Iwai et al. (56) fitted the binary interaction parameter for this system and obtained k_{12} =0.09. This value of 0.09 was also produced by invoking eq. (45) with the values for θ_1 to θ_3.

Table 3.4: **Validation of k_{12} with d-limonene**

Author	**k_{12}**
Iwai (56)	0.09
Glenn	0.09

The critical temperature and pressure for CO_2 are $T_c = 304.2$ K and $P_c = 7.37$ bar, respectively, with $T_r = \frac{T}{T_c}$ and $P_r = \frac{P}{P_c}$. The average k_{12} has been used for terpinen-4-ol and α-cedrene in this study. The reported k_{12} (38) has been used for α-pinene.

The binary interaction parameter increases as both temperature and pressure increase. Tables 3.5-3.7 show each k_{12} on the most abundant component in the essential oil as a function of its temperature and pressure used in this study. The mean k_{12} has been reported for each most abundant component.

The T_{cr2} and P_{cr2} for terpinen-4-ol is 754.3 K and 3.32 MPa respectively.

3.7.2 k_{12} AS A FUNCTION OF TEMPERATURE AND PRESSURE FOR TERPINEN-4-OL

Table 3.5: **Binary interaction parameter as a function of temperature and pressure for terpinen-4-ol**

T=298.15 K

ρ(g/mL)	**P (MPa)**	**k_{12}**
0.2	5.69	0.074
0.7	6.43	0.083

T=313.15 K

ρ(g/mL)	**P (MPa)**	**k_{12}**

0.2	7.03	0.091
0.3	8.18	0.106
0.4	8.69	0.112
0.6	9.67	0.125
0.7	11.43	0.147

T=323.15 K

ρ(g/mL)	**P (MPa)**	k_{12}
0.2	7.93	0.098
0.3	9.18	0.118
0.4	10.13	0.129
0.6	12.26	0.157
0.7	15	0.191

T=333.15 K

ρ(g/mL)	**P (MPa)**	k_{12}
0.2	8.2	0.106
0.3	10.2	0.13
0.4	11.6	0.148
0.6	14.9	0.189
0.7	18.6	0.237

The average k_{12} for terpinen-4-used in this study is 0.124. As both temperature and pressured increase, so does the binary interaction parameter.

3.7.3 k_{12} AS A FUNCTION OF TEMPERATURE AND PRESSURE FOR A-CEDRENE

The T_{cr2} and P_{cr2} for α-cedrene is 792.2 K and 2.12 MPa respectively.

Table 3.6: **Binary interaction parameter as a function of temperature and pressure for α-cedrene**

T=298.15 K

ρ(g/mL)	**P (MPa)**	k_{12}
0.2	5.69	0.083
0.7	6.43	0.084

T=313.15 K

ρ(g/mL)	**P (MPa)**	k_{12}
0.2	7.03	0.077
0.3	8.18	0.078
0.4	8.69	0.078
0.6	9.67	0.079
0.7	11.43	0.08

T=323.15 K

ρ(g/mL)	**P (MPa)**	k_{12}
0.2	7.63	0.085
0.3	9.18	0.086
0.4	10.12	0.087
0.6	12.26	0.088
0.7	15	0.089

T=333.15 K

ρ(g/mL)	**P (MPa)**	k_{12}
0.2	8.21	0.085
0.3	10.16	0.087
0.4	11.56	0.088
0.6	14.89	0.089
0.7	18.64	0.091

The average k_{12} for α-cedrene in this study is 0.084. Similarly, as temperature and pressure increase so does the binary interaction parameter.

3.7.4 K_{12} AS A FUNCTION OF TEMPERATURE AND PRESSURE FOR A-PINENE

The T_{cr2} and P_{cr2} for α-pinene is 644.0 K and 2.77 MPa respectively.

Table 3.7: **Binary interaction parameter as a function of temperature and pressure for α-pinene**

T=298.15 K

ρ(g/mL)	**P (MPa)**	k_{12}
0.2	5.69	0.086
0.7	6.43	0.087

T=313.15 K

ρ(g/mL)	**P (MPa)**	k_{12}
0.2	7.03	0.087
0.3	8.18	0.088
0.4	8.69	0.089
0.6	9.67	0.09
0.7	11.43	0.091

T=323.15 K

ρ(g/mL)	**P (MPa)**	k_{12}
0.2	7.63	0.088
0.3	9.18	0.089
0.4	10.12	0.09
0.6	12.26	0.091
0.7	15	0.092

T=333.15 K

ρ(g/mL)	P (MPa)	k_{12}
0.2	8.21	0.089
0.3	10.16	0.09
0.4	11.56	0.091
0.6	14.89	0.092
0.7	18.64	0.094

The average k_{12} for α-pinene is 0.089 which Sousa et. al (53) report as $k_{12} = 0.110$ for supercritical temperatures. In this study, $k_{12}=0.110$ was used. Similarly, as temperature and pressure increase so does the binary interaction parameter. Table 3.8 shows the binary interaction parameters used in this study for the most abundant component in each essential oil.

Table 3.8: Binary interaction parameters on most abundant component in essential oils

Most Abundant Oil Component	Binary Interaction Parameter k_{12}
Terpinen-4-ol	0.124
α-cedrene	0.084
α-pinene	0.110

3.8 MODIFIED EXTRACTOR DESIGN FOR DYNAMIC SOLUBILITY MEASUREMENTS IN CO_2

The dynamic solubility method was used in this work. An ISCO SFX 2-10 Supercritical Fluid Extractor, shown in Figure 3.15, was modified from its original design so as to change the direction of flow allowing CO_2 to enter the extraction vessel from the bottom and exit from the top. This permitted for measuring the vapor mole fraction of each component in the CO_2 rich phase. With the modification, the oil-rich phase remains in the bottom of the extraction vessel, and the CO_2-rich phase exits the top of the vessel for subsequent analysis. Thus, we measured the vapor phase mole fraction of a given component in the CO_2-rich phase.

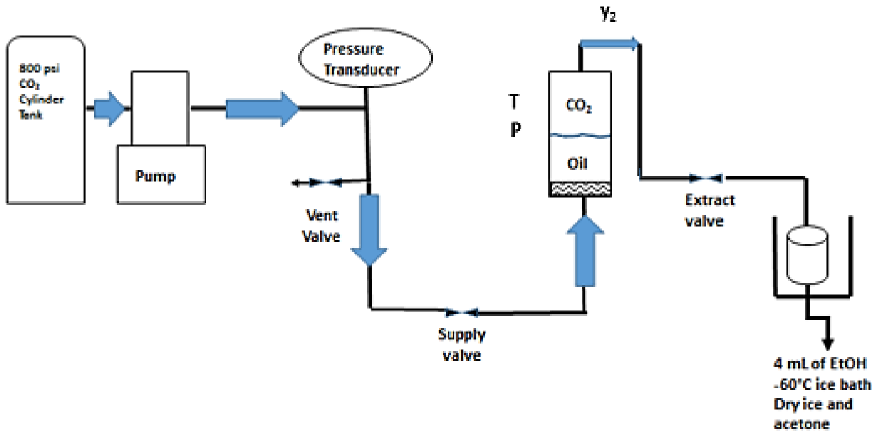

Figure 3.15: **Modified Extractor Design for Dynamic Solubility Measurements in CO_2**

The extraction vessel was embedded in an isothermal heat block to maintain the desired temperature. The extractor was pressurized with CO_2 by an ISCO D260 high-pressure syringe pump, which is controlled by an ISCO series D pump controller. The pump was filled from a standard CO_2 cylinder. To insure equilibration between phases, the total time of CO_2 flow was 180 minutes for each experimental run. The total CO_2 flow rate was determined by dividing the total volume CO_2 from the pump by the total extraction time. The extract was depressurized at the extract valve, and the CO_2 + solute mixture was bubbled into 4000 μL of ethanol solvent, which was kept at -60°C using a dry ice/acetone bath.

3.9 UV-VIS

The mole fraction of the solute in the ethanol was quantified using UV-VIS spectrometry. The UV spectrometer was calibrated for each component at several wavelengths, with a wavelength of 290 nm providing most linear curve. Calibration curves for each component are shown. Calibration procedure are documented in Appendix B.

3.9.1 TERPINEN-4-OL CALIBRATION

The calibration data was most linear at 290 nm for terpinen-4-ol. The results documented in Table 3.9 show absorbance as a function of concentration in µg/µL. The graph is plotted in Figure 3.16.

Table 3.9: **Calibration data for terpinen-4-ol at 290 nm**

Concentration (ug/uL)	Absorbance
0	0
18.7	0.033
46.7	0.111
93.3	0.193

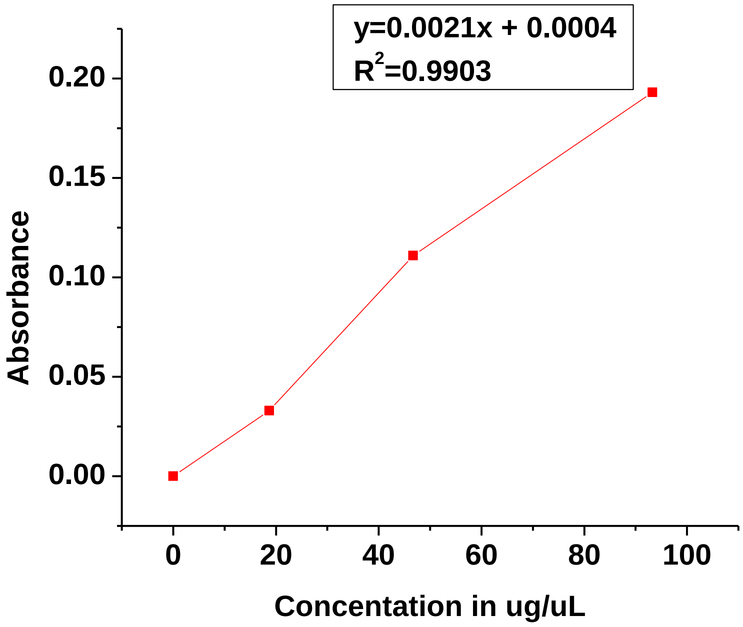

Figure 3.16:**Calibration of UV-VIS Spectrometry at 290 nm for terpinen-4-ol**

The linear regression equation is $y = 0.0021x + 0.0004$ with $R^2 = 0.9903$ where y is the dependent variable representing absorbance and x represents concentration in µg/µL. In Appendix F, Column 3 show the measured absorbance.

$$x = \frac{y - 0.0004}{0.0021}$$

The concentration x, in µg/µL, from each measured absorbance is shown in column 4 of Appendix F. The amount of ethanol injected is 4000 µL. Multiplying column 4 by 4000 µL, the amount of ethanol injected, gave the amount of grams extracted in µg in column 5. Dividing by 1,000,000 calculated the value of grams extracted in column 6. Column 7 shows the calculated moles of terpinen-4-ol extracted. The molecular weight of terpinen-4-ol is 154.25 g/mol.

$$Moles\ extracted = \frac{Grams\ extracted}{Molecular\ weight\ of\ terpinen - 4 - ol}$$

The total CO_2 volume from the pump was recorded in column 8. The total extraction time was 3 hours (180 minutes). The total CO_2 flow rate was determined by dividing the total volume CO_2 from the pump by 180 minutes shown in column 9. Column 10 shows the calculated moles of CO_2. The molecular weight of CO_2 is 44.01 g/mol. The density of CO_2 represents the density at the pump. The chiller brings the pump temperature to 0°C. The density at 0°C is 0.927 g/mL.

$$Moles\ of\ CO2 = \frac{\rho V}{molecular\ weight\ of\ CO2}$$

Finally, column 11 shows y_2, the mole fraction of terpinen-4-ol in CO_2.

$$y_2 = \frac{Moles\ of\ terpinen{-}4{-}ol}{Moles\ of\ CO2 + moles\ of\ terpinen{-}4{-}ol}$$

3.9.2 α-CEDRENE CALIBRATION

The calibration data was most linear at 290 nm for α-cedrene. The results documented in Table 3.10 show absorbance as a function of concentration in ug/uL. The graph is plotted in Figure 3.17.

Table 3.10: **Calibration data for α-cedrene at 290 nm**

Concentration (ug/uL)	Absorbance
0	0
0.093	0.008
9.32	0.712
18.7	1.24

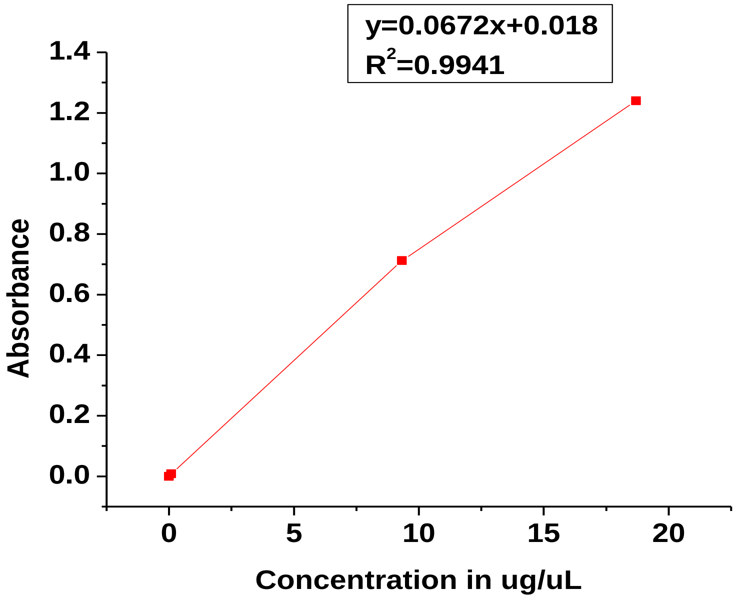

Figure 3.17: **Calibration of UV-VIS Spectrometry at 290 nm for α-cedrene**

The linear regression equation is $y = 0.0672x + 0.018$ with $R^2 = 0.9941$, where *y* is the dependent variable representing the absorbance and *x* represents the concentration in μg/μL. In Appendix G, Column 3 shows the measured absorbance.

$$x = \frac{y + 0.0001}{0.0062}$$

The concentration x, in µg/µL, from each measured absorbance is shown in column 4 of Appendix G. The amount of ethanol injected is 4000 µL and is multiplied by x (column 4) in µg/µL. Multiplying column 4 by 4000 µL, the amount of ethanol injected, calculated the value of grams extracted in µg, column 5. Dividing by 1,000,000 calculated the amount of grams extracted in column 6. Column 7 shows the calculated moles of α-cedrene extracted. The molecular weight of α-cedrene is 204.35 g/mol.

$$Moles\ extracted = \frac{Grams\ extracted}{Molecular\ weight\ of\ \alpha - cedrene}$$

The total CO_2 volume from the pump was recorded in column 8. The total extraction time is 3 hours (180 minutes). The total CO_2 flow rate was determined by dividing the total volume CO_2 from the pump by 180 minutes shown in column 9. Column 10 shows calculated moles of CO_2. The molecular weight of CO_2 is 44.01 g/mol. The density of CO_2 represents the density at the pump. The chiller brings the pump temperature to 0°C. The density at 0°C is 0.927 g/mL.

$$Moles\ of\ CO2 = \frac{\rho V}{molecular\ weight\ of\ CO2}$$

Finally, column 11 show y_2, the mole fraction of α-cedrene in CO_2.

$$y_2 = \frac{Moles\ of\ \alpha - cedrene}{Moles\ of\ CO2 + moles\ of\ \alpha - cedrene}$$

3.9.3 α-PINENE CALIBRATION

The calibration data was also most linear at 290 nm for α-pinene. The results documented in Table 3.11 show absorbance as a function of concentration, ug/uL. The graph is plotted in Figure 3.18.

Table 3.11: **Calibration data for α-pinene at 290 nm**

Concentration in (ug/uL)	Absorbance
0	0
17.2	0.112
42.9	0.25
85.8	0.533

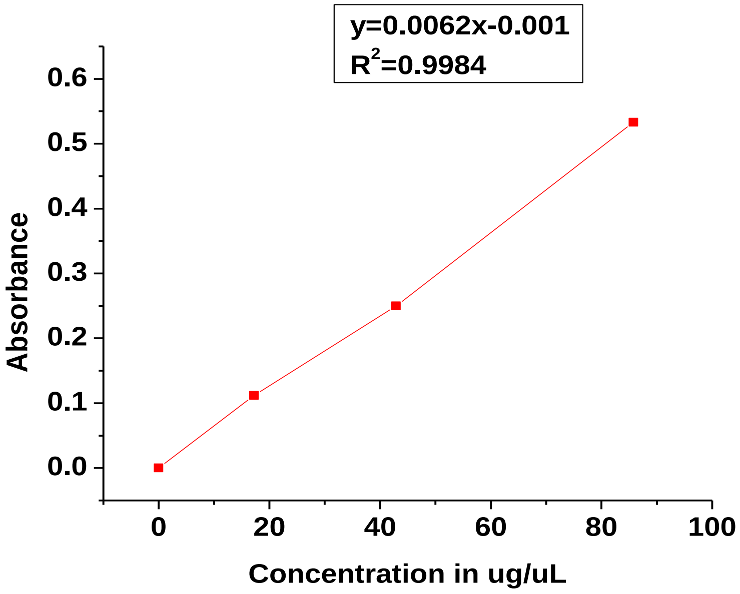

Figure 3.18: **Calibration of UV-VIS Spectrometry at 290 nm for α-pinene**

The linear regression equation is $y = 0.0062x - 0.001$ with $R^2 = 0.9984$ where y is the dependent variable representing absorbance and x represents the concentration in µg/µL. In Appendix H, column 3 shows the measured absorbance.

$$x = \frac{y + 0.001}{0.0062}$$

The concentration x, in µg/µL, from each measured absorbance is shown in column 4. . Multiplying column 4 by 4000 µL, the amount of ethanol injected, provided the value of grams extracted in µg, column 5. Dividing by 1,000,000 calculated the grams extracted, column 6. Column 7 shows the calculated moles of α-pinene extracted. The molecular weight of α-pinene is 136 g/mol.

$$Moles\ extracted = \frac{Grams\ extracted}{Molecular\ weight\ of\ \alpha - pinene}$$

The total CO_2 volume from the pump was recorded in column 8. The total extraction time is 3 hours (180 minutes). The total CO_2 flow rate was determined by dividing the total volume CO_2 from the pump by 180 minutes shown in column 9. Column 10 shows the calculated moles of CO_2. The molecular weight of CO_2 is 44.01 g/mol. The density of CO_2 represents the density at the pump. The chiller brings the pump temperature to 0°C. The density at 0°C is 0.927 g/mL.

$$Moles\ of\ CO2 = \frac{\rho V}{molecular\ weight\ of\ CO2}$$

Finally, column 11 show $y_{2,}$ the mole fraction of α-pinene in CO_2.

$$y_2 = \frac{Moles\ of\ \alpha{-}pinene}{Moles\ of\ CO2{+}moles\ of\ \alpha{-}pinene}$$

3.9.4 MEAN ABSORBANCE AND STANDARD DEVIATION

Prior to determining the vapor mole fraction (y_2) of the three essential oils, the absorbance values were determined from the arithmetic mean of three absorbance values provided by the UV-VIS analysis. Each absorbance was measured during 3 time intervals within a one day period. The mean absorbance was then used to determine the solubility in liquid and supercritical CO_2. Tables 3.12-3.14 show that as both temperature and density increase, so does the absorbance and ultimately the vapor mole fraction.

3.9.5 MEAN AND STANDARD DEVIATION ABSORBANCE FOR TERPINEN-4-OL

The mean and standard deviation absorbance for terpinen-4-ol are shown in Table 3.12. The mean absorbance at each temperature and density were used to determine the vapor mole fraction y_2 shown in column 3 in Appendix F.

Table 3.12: **Mean and Standard Deviation Absorbance for terpinen-4-ol**

T = 25°C

ρ(g/mL)	**Absorbance 1**	**Absorbance 2**	**Absorbance 3**	**Mean**	**Standard deviation**
0.2	0.005	0.003	0.004	0.004	0.001
0.7	0.089	0.087	0.084	0.087	0.002

T = 40°C

ρ (g/mL)	**Absorbance 1**	**Absorbance 2**	**Absorbance 3**	**Mean**	**Standard deviation**
0.2	0.008	0.003	0.003	0.005	0.002
0.3	0.012	0.015	0.011	0.013	0.002
0.4	0.019	0.011	0.013	0.014	0.004
0.6	0.030	0.025	0.026	0.027	0.003
0.7	0.410	0.360	0.400	0.390	0.027

T=50°C

ρ (g/mL)	**Absorbance 1**	**Absorbance 2**	**Absorbance 3**	**Mean**	**Standard deviation**
0.2	0.005	0.001	0.002	0.003	0.002
0.3	0.040	0.026	0.029	0.032	0.007
0.4	0.040	0.035	0.029	0.040	0.090
0.6	0.195	0.210	0.195	0.200	0.007
0.7	0.650	0.649	0.659	0.653	0.006

T=60°C

ρ (g/mL)	**Absorbance 1**	**Absorbance 2**	**Absorbance 3**	**Mean**	**Standard deviation**
0.2	0.050	0.030	0.020	0.033	0.015
0.3	0.033	0.034	0.039	0.035	0.003
0.4	0.022	0.010	0.002	0.111	0.008
0.6	0.170	0.130	0.140	0.150	0.021
0.7	0.300	0.260	0.270	0.270	0.025

3.9.6 MEAN AND STANDARD DEVIATION FOR A-CEDRENE

The mean and standard deviation absorbance for α-cedrene are shown in Table 3.13. The mean absorbance at each temperature and density were used to determine the vapor mole fraction y_2 shown in column 3 in Appendix G.

Table 3.13: **Mean and Standard Deviation for α-cedrene**

T = 25°C

ρ(g/mL)	Absorbance 1	Absorbance 2	Absorbance 3	Mean	Standard deviation
0.2	0.036	0.034	0.035	0.035	0.001
0.7	0.065	0.064	0.063	0.064	0.001

T = 40°C

ρ (g/mL)	Absorbance 1	Absorbance 2	Absorbance 3	Mean	Standard deviation
0.2	0.195	0.191	0.192	0.193	0.002
0.3	0.300	0.295	0.298	0.298	0.003
0.4	0.530	0.525	0.533	0.529	0.003
0.6	0.536	0.531	0.533	0.533	0.002
0.7	0.834	0.824	0.819	0.826	0.006

T=50°C

ρ (g/mL)	Absorbance 1	Absorbance 2	Absorbance 3	Mean	Standard deviation
0.2	0.044	0.043	0.042	0.044	0.001
0.3	0.085	0.077	0.090	0.084	0.007
0.4	0.465	0.462	0.460	0.462	0.003
0.6	0.660	0.659	0.658	0.659	0.001
0.7	1.095	1.091	1.093	1.093	0.002

T=60°C

ρ (g/mL)	Absorbance 1	Absorbance 2	Absorbance 3	Mean	Standard deviation
0.2	0.110	0.108	0.109	0.109	0.001
0.3	0.132	0.125	0.140	0.132	0.008
0.4	0.272	0.287	0.279	0.279	0.006
0.6	1.550	1.570	1.470	1.530	0.004
0.7	1.400	1.330	1.490	1.400	0.070

3.9.7 MEAN AND STANDARD DEVIATION FOR α-PINENE

The mean and standard deviation absorbance for α-pinene are shown in Table 3.14. The mean absorbance at each temperature and density were used to determine the vapor mole fraction y_2 shown in column 3 in Appendix H.

Table 3.14: **Mean and Standard Deviation Absorbance for α-pinene**

T = 25°C

ρ(g/mL)	**Absorbance 1**	**Absorbance 2**	**Absorbance 3**	**Mean**	**Standard deviation**
0.2	0.009	0.008	0.007	0.008	0.001
0.7	0.018	0.016	0.017	0.017	0.001

T = 40°C

ρ (g/mL)	**Absorbance 1**	**Absorbance 2**	**Absorbance 3**	**Mean**	**Standard deviation**
0.2	0.007	0.008	0.005	0.007	0.002
0.3	0.002	0.012	0.011	0.011	0.007
0.4	0.018	0.010	0.009	0.012	0.005
0.6	0.017	0.011	0.012	0.013	0.003
0.7	0.028	0.023	0.022	0.024	0.003

T=50°C

ρ (g/mL)	**Absorbance 1**	**Absorbance 2**	**Absorbance 3**	**Mean**	**Standard deviation**
0.2	0.018	0.015	0.011	0.015	0.004
0.3	0.018	0.011	0.023	0.017	0.005
0.4	0.043	0.041	0.048	0.044	0.004
0.6	0.055	0.050	0.047	0.051	0.004
0.7	0.062	0.058	0.055	0.058	0.004

T=60°C

ρ (g/mL)	**Absorbance 1**	**Absorbance 2**	**Absorbance 3**	**Mean**	**Standard deviation**
0.2	0.018	0.02	0.011	0.016	0.005
0.3	0.028	0.025	0.015	0.023	0.007
0.4	0.074	0.055	0.058	0.062	0.010
0.6	0.077	0.078	0.076	0.077	0.001
0.7	0.112	0.080	0.l00	0.098	0.018

3.10 PENG ROBINSON EQUATION OF STATE

Solubilities were correlated with the Peng-Robinson (PR) cubic equation of state with standard mixing rules (57).

$$P = \frac{RT}{V_m - b} - \frac{a}{V^{2}_{m+2V_{m}b-b^{2}}} \qquad (1)$$

$$a = \frac{0.457236\,\alpha\,R^{2}\,T_c^{2}}{P_c} \qquad 2)$$

$$b_i = \frac{0.077961\,R\,T_c}{P_c} \qquad (3)$$

$$\alpha_i = \left(1 + \left(0.37464 + 1.54226\,\omega_i - 0.26992\,\omega_i^{2}\right)\left(1 - \sqrt{\frac{T}{T_{c_i}}}\right)\right)^{2} \qquad (4)$$

For binary mixtures,

$$a = \Sigma\Sigma\, x_i\, x_j\, a_{ij} \qquad (5)$$

$$b = \Sigma\, x_i\, b_i \qquad (6)$$

$$a_{ij} = (1 - k_{ij})\sqrt{a_i}\, a_j \qquad (7)$$

where k_{ij} is the binary interaction parameter. For purpose of this work, the subscript i represents the solvent (CO_2) and j the solute.

$$\ln \phi_j = \frac{b_i}{b}\,(Z\text{-}1) - \ln\,(Z - B) - \frac{A}{2\sqrt{2}B} \times \left(\frac{2\sum z_j\, a_{ij}}{a} - \frac{bi}{b}\right) \ln\left(\frac{Z+(1+\sqrt{2})B}{Z+(1-\sqrt{2})B}\right) \qquad (8)$$

Where $B = \frac{bP}{RT}$ $A = \frac{aP}{RT^{2}}$ and $Z = \frac{PV}{RT}$

Component fugacity coefficients for CO_2 and each most abundant component oil as well as liquid and vapor mole fractions for CO_2 and the most abundant component at the mean k_{12} are tabulated in Appendices I-K at temperatures and densities observed in this study.

3.11 LIQUID AND SUPERCRITICAL CO_2

CO_2 is a non-toxic, non-flammable substance that is used commercially for carbonating beverages and food packaging. CO_2 is inexpensive and readily available from industrial sources. While CO_2 exists as a gas at ambient temperatures, it can be liquefied at temperatures below 31°C if the pressure is around 800 psig. CO_2 is commonly stored and delivered from steel tanks at ambient temperature. Above the critical point, 31.1°C and 74 atm, CO_2 exists as a supercritical fluid (58). Figure 3.19 shows the region which encompasses both liquid and supercritical states used in the solubility of the most abundant component of three essential oils in this study.

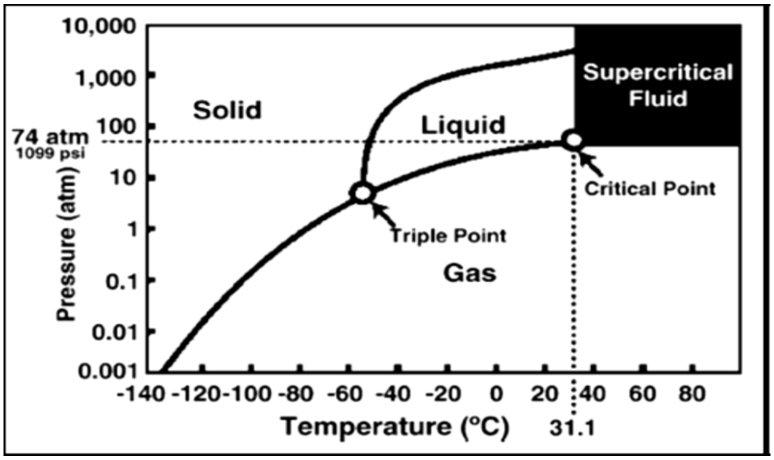

Figure 3.19: **Phase diagram for Carbon Dioxide (59).**

3.12 VALIDATION OF EXPERIMENTAL TECHNIQUE

There are no known data available on the solubility of terpinen-4-ol and α-cedrene. However, there is some solubility data on α-pinene but not at the temperatures and densities performed in this research. Akgun et. al (45) used the static solubility method to report vapor mole fraction solubility at 323.15 K and 9.18 MPa as 0.0076.

Reported vapor mole fraction solubility at the same temperature of 323.15K and density of 0.6 g/mL using the dynamic solubility method reported a vapor mole solubility of 0.0078 which is in exact agreement with those of Akgun et al (60). These results validate experimental technique used from the modified extractor and UV-VIS.

3.13 SOLUBILITY OF TERPINEN-4-OL IN SUPERCRITCAL CO_2

The mole fraction of a given component was computed for each experimental temperature and density. Both the mass of ethanol and the total mass of CO_2 were measured for a given experimental run, allowing calculation of the component mole fraction by mass balance. Solubility versus density curves were generated by conducting multiple experiments at specified temperatures and CO_2 density. The vapor mole fraction (y_2) of terpinen-4-ol is plotted against the pure CO_2 density at supercritical temperatures in Figure 3.20. At a given density, increasing temperature increases the solubility due to the increased vapor pressure of the solute.

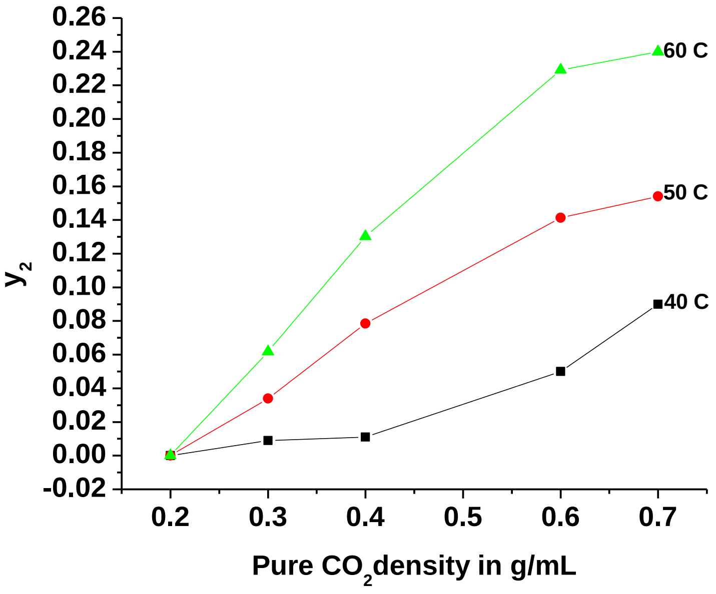

Figure 3.20: **Solubility of terpinen-4-ol in SC-CO_2**

3.14 SOLUBILITY OF α-CEDRENE IN LIQUID AND SUPERCRITCAL CO_2

The vapor mole fraction (y_2) of alpha-cedrene in CO_2 is plotted against the density at various temperatures in Figure 3.21. The values are in good agreement with the PR-EOS. At a given density, increasing temperature increases the solubility as a result of the increased vapor pressure of the solute.

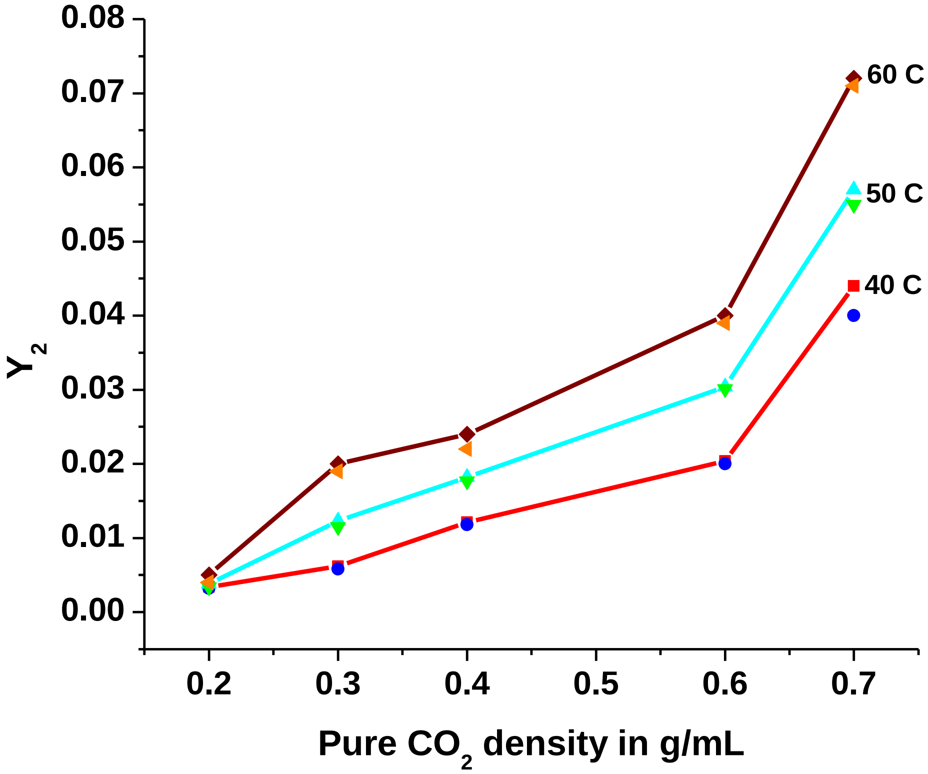

Figure 3.21: **Solubility of α-cedrene in SC-CO_2**

3.15 SOLUBILITY OF α-PINENE IN LIQUID AND SUPERCRITCAL CO_2

The solubility of α-pinene in supercritical CO_2 was measured at several densities at 313K, 323K and 333K shown in Figure 3.22. The vapor mole fraction (y_2) of alpha-pinene is plotted against the pure CO_2 density at each supercritical temperature.

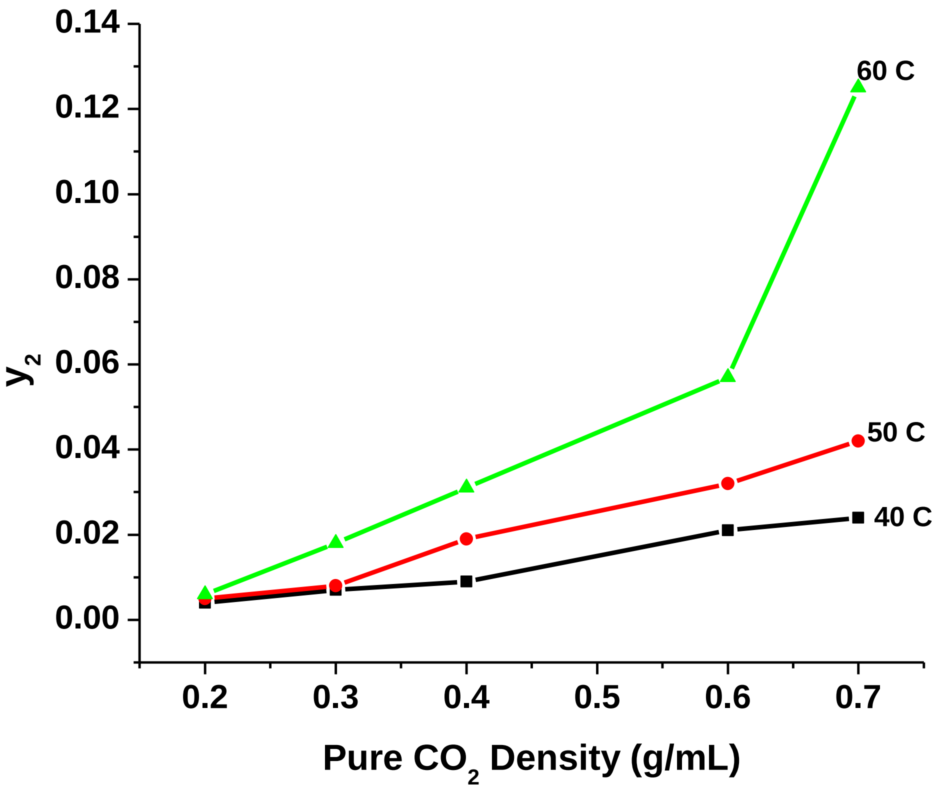

Figure 3.22: **Solubility of α-pinene in supercritical CO_2**

There are two phenomena that we gather from the solubility data. First, as the density increases, the solubility increases and secondly, as the temperatures increases so does the solubility increase along each isotherm.

Table 3.15 shows the vapor mole fraction for each of the 3 most abundant components in the studied essential oils at 60ºC at various densities. The vapor mole fraction increases as the density increases. α-pinene has a higher vapor mole fraction over α-cedrene with terpinen-4-ol having the highest vapor mole fractions (Figure 3.23). This is what we would expect as α-pinene is the most volatile out of the 3 most abundant oil components. We suspect terpinen-4-ol as having the highest vapor mole fraction due to hydrogen bonding.

Table 3.15: **Component solubility at 60°c**

ρ (g/mL)	**Y_2 α-cedrene $C_{15}H_{24}$**	**Y_2 α-pinene $C_{10}H_{16}$**	**Y_2 terpinen-4-ol $C_{10}H_{18}OH$**
0.2	0.004	0.006	0.011
0.3	0.016	0.018	0.063
0.4	0.023	0.031	0.111
0.6	0.042	0.057	0.226
0.7	0.061	0.125	0.240

3.16 SOLUBILITY OF TERPINEN-4-OL AND PR-EOS

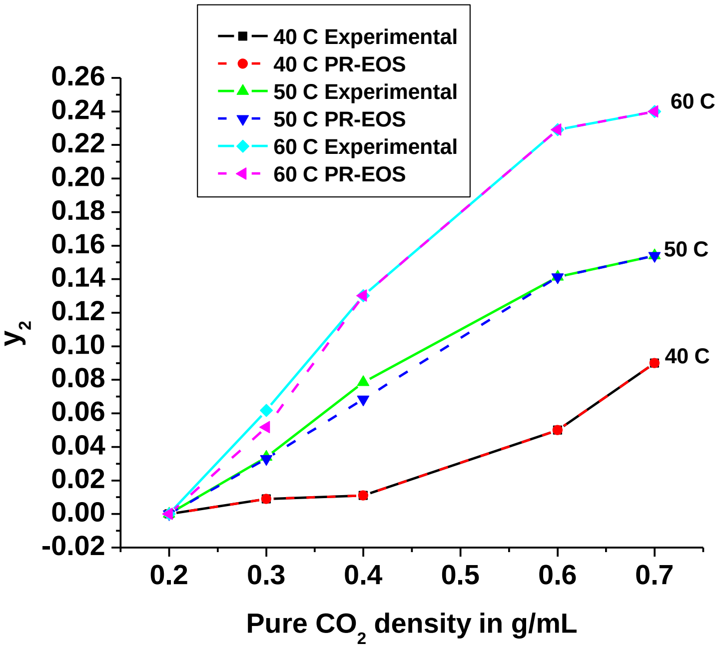

Figure 3.23: **Solubility of terpinen-4-ol with PR-EOS in SC-CO_2**

Table 3.16: **Solubility of terpinen-4-ol in supercritical CO_2 at T= 40°C with PR-EOS**

Density (g/mL)	**Y_2**	**Y_2 PREOS**
0.2	1e-4	1e-4
0.3	0.007	0.001
0.4	0.023	0.020
0.6	0.068	0.068
0.7	0.120	0.120

Table 3.17: **Solubility of terpinen-4-ol in supercritical CO_2 at T= 50°C with PR-EOS**

Density (g/mL)	**Y_2**	**Y_2 PREOS**
0.2	0.007	1e-4
0.3	0.019	0.010
0.4	0.072	0.072
0.6	0.150	0.150
0.7	0.160	0.160

Table 3.18: **Solubility of terpinen-4-ol in supercritical CO_2 at T= 60°C with PR-EOS**

Density (g/mL)	**Y_2**	**Y_2 PREOS**
0.2	2e-4	2e-4
0.3	0.050	0.020
0.4	0.100	0.100
0.6	0.225	0.225
0.7	0.240	0.240

The chemical structure for terpinen-4-ol includes a hydroxyl group whereas α-cedrene and α-pinene do not. Terpinen-4-ol is soluble in water and therefore, the solubility in liquid and supercritical CO_2 is much higher than for α-cedrene (Figure 3.24) and α-pinene (Figure 3.25) at higher temperatures and density. The correlation of the experimental data in this work agrees with the PR-EOS at each supercritical CO_2 temperature and density.

3.17 SOLUBILITY OF α-CEDRENE AND PR-EOS

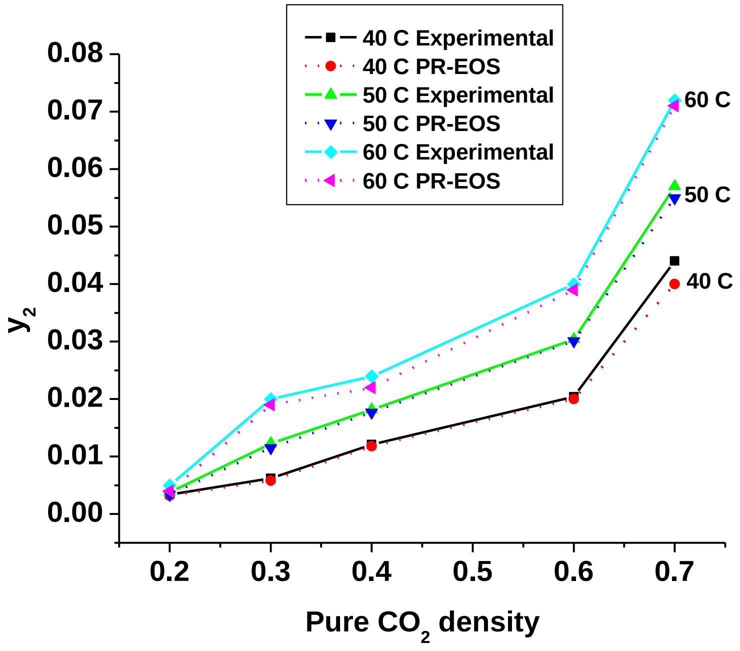

Figure 3.24: **Solubility of α-cedrene with PR-EOS in SC-CO_2**

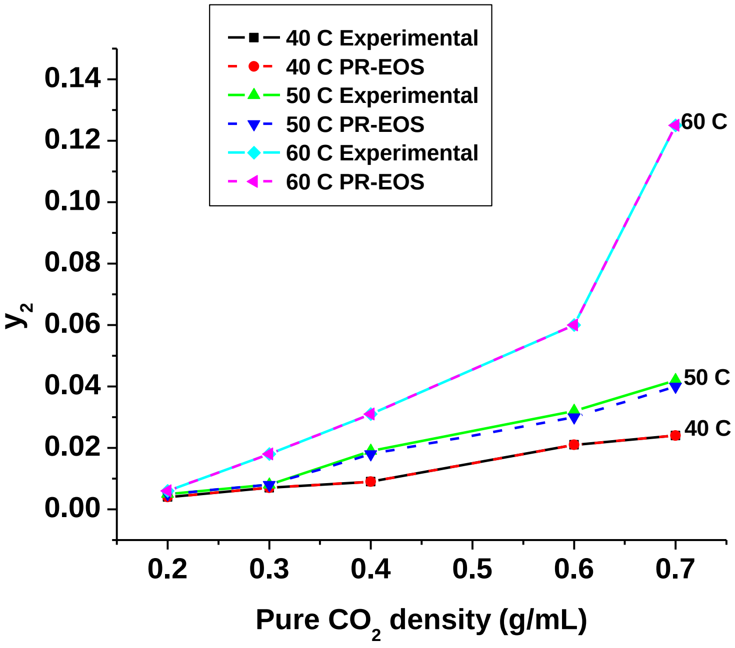

Figure 3.25: **Solubility of α-pinene with PR-EOS in SC-CO_2**

Tables 3.19-3.21 show the measured y_2 experimental data compared for each PR-EOS value.

Table 3.19: **Solubility of α-cedrene in supercritical CO_2 at T= 40°C with PR-EOS**

Density (g/mL)	**Y_2**	**Y_2 PREOS**
0.2	1e-4	1e-4
0.3	0.003	0.003
0.4	0.014	0.014
0.6	0.036	0.036
0.7	0.044	0.044

Table 3.20**: Solubility of α-cedrene in supercritical CO_2 at T= 50°C with PR-EOS**

Density (g/mL)	**Y_2**	**Y_2 PREOS**
0.2	0.001	0.001
0.3	0.006	0.005
0.4	0.018	0.018
0.6	0.037	0.037
0.7	0.054	0.054

Table 3.21: **Solubility of α-cedrene in supercritical CO_2 at T= 60°C with PR-EOS**

Density (g/mL)	**Y_2**	**Y_2 PREOS**
0.2	0.003	0.001
0.3	0.008	0.008
0.4	0.021	0.021
0.6	0.040	0.040
0.7	0.122	0.122

The correlation of the experimental data of this work agrees with the PR-EOS at each supercritical temperature.

3.18 SOLUBILITY OF α-PINENE AND PR-EOS

Reported vapor mole fraction solubility at 323.15K and 9.18 MPa is 0.008 in exact agreement with those of Akgun et al.(60). Results again are well correlated with the PR-EOS in Tables 3.22-3.24.

Table 3.22: **Solubility of α-pinene in supercritical CO_2 at T= 40°C with PR-EOS**

Density (g/mL)	**Y_2**	**Y_2 PREOS**
0.2	0.004	0.004
0.3	0.010	0.010
0.4	0.012	0.012
0.6	0.017	0.017
0.7	0.020	0.020

Table 3.23: **Solubility of α-pinene in supercritical CO_2 at T= 50°C with PR-EOS**

Density (g/mL)	**Y_2**	**Y_2 PREOS**
0.2	0.006	0.006
0.3	0.012	0.012
0.4	0.020	0.020
0.6	0.030	0.030
0.7	0.040	0.040

Table 3.24: **Solubility of α-pinene in supercritical CO_2 at T= 60°C with PR-EOS**

Density (g/mL)	**Y_2**	**Y_2 PREOS**
0.2	0.008	0.008
0.3	0.018	0.018
0.4	0.030	0.030
0.6	0.050	0.050
0.7	0.060	0.060

3.19 SOLUBLITY OF MAJOR COMPONENTS IN LIQUID CO_2

The apparent vapor mole fractions for each of the three essential oil components are tabulated in Table 3.25 for liquid CO_2 at a density of 0.1781 g/mL at 25°C as well as for the vapor mole fraction for liquid CO_2 at a density of 0.7105 g/mL at 25°C. The results show experimental solubilities in agreement with the PREOS in the vapor phase for each of the most abundant oil components.

Table 3.25: **Experimental and PR prediction of solubility of major components of essential oils in CO_2 in liquid CO_2**

	ρ=0.1781 g/mL and 25°C		**ρ=0.7105 g/mL and 25°C**	
Component	Exp.	PR	Exp.	PR
Terpinen-4-ol	0.0100	0.0100	0.0597	0.0597
α-cedrene	0.0009	0.0009	0.0125	0.0125
α-pinene	0.0020	0.0020	0.0189	0.0189

3.20 ESSENTIAL OIL AND MOST ABUNDANT COMPONENT COMPARISON

The vapor mole fraction of each essential oil was then compared with the vapor mole fraction of the most abundant component of the essential oil at T=50°C and ρ=0.6 g/mL. Calibrations for each essential oil can be found in section 3.9.

3.21 SOLUBILITY OF ESSENTIAL OIL COMPARED TO ITS MOST ABUNDAMENT COMPONENT

Table 3.26 shows that the mole fractions of the most abundant component well represent the total essential oil component.

Table 3.26: **Y_2 comparison of essential oil with most abundant component at 50°C and 12.26 MPa**

Oil/Key Component	Y_2 Oil	Y_2 Key Component
Hinoki / α - pinene	0.344	0.344
Tea tree / terpinen-4-ol	0.167	0.160
Cedar wood/ α - cedrene	0.037	0.032

The results correlate well with the Gas Chromatogram results reported earlier. Tea tree oil peaked at 8 minutes and 59 seconds from Figure 2.5. A very close peak came out at 8 minutes and 76 seconds which explains why the solubility of the entire oil and most abundant oil vary slightly. Cedar wood oil peaked at 11 minutes and 12 seconds with very close peaks at both 10 minutes and 89 seconds and 10 minutes and 98 minutes from Figure 2.8. The solubility of the entire oil and the most abundant component varied slightly. Hinoki oil peaked at 8 minutes and 59 seconds with no other peaks near it in Figure 2.11. This is why the solubilities of the most abundant component came out to be exactly the same solubility of 0.344 at 50°C and 12.26 MPa.

3.22 NEW KNOWLEDGE ON PHASE EQUILIBRIUM OF TERPENIN-4-OL, α-CEDRENE, α-PINENE IN LIQUID AND SUPERCRITICAL CO_2

The most abundant components in tea tree, cedar wood and hinoki oils have been identified as terpinen-4-ol, α-cedrene and α-pinene, respectively. Specifically, the boiling temperature, critical temperature, critical pressure and acentric factor are now reported for α-cedrene as 566.64 K, 792.2 K, 21.2 bar and 0.212 respectively using The Joback Contribution Method.

The binary interaction parameters for CO_2/terpinen-4-ol, CO_2/α-cedrene, CO_2/α-pinene have been identified at temperatures of 298.15 K, 313.15 K, 323.15 K and 333.15 K at various pressures. Mean absorbance values as a function of temperature and density have also been recorded in this research.

The vapor mole fraction of terpinen-4-ol in both liquid and supercritical CO_2, as well as the vapor mole fraction of α-pinene using the dynamic solubility method at densities of 0.2, 0.3, 0.4, 0.6 and 0.7 g/mL are now known. Results show an increase in the solubility of each oil with an increase in density as well as a solubility increase as the temperature increases along a given isotherm. The experimental data correlates well with the PR-EOS. In addition, the vapor mole fraction of each essential oil well represents the most abundant component of each essential oil. Table 3.27 shows the correlation of the molecular weight, the boiling point and vapor pressure of each of the most abundant component compared to its highest solubility.

Table 3.27: **Solubility characterization**

Most Abundant Component	**Boiling Point (°C)**	**Molecular Weight (g/mol)**	**Vapor Pressure (mm Hg) at 25°C**	**Highest Solubility y_2**
α-pinene	156	136.2	4.750	0.13
Terpinen-4-ol	209	154.3	0.040	0.25
α-cedrene	262	204.4	0.018	0.06

CHAPTER 4: DEACTIVATION OF ALLERGENIC PROTEINS WITH ESSENTIAL OILS

4.1 MOTIVATION

The motivation behind the final chapter of this research was to test to see if indeed, essential oils themselves could in any way, inactivate allergenic protein using an Enzyme-Linked Immunosorbent Assay (ELISA) response. Dust samples were gathered from a local home in Columbia, South Carolina with known cat allergens. The goal of this work is to test the hypothesis that an essential oil may inactivate the allergenic proteins *Fel d 1* and *Der f 1* as measured by sandwich ELISA. Another hypothesis tested in this work is to determine whether prolonged exposure to dry ice temperatures (-70°C) will affect the ELISA response of *Fel d 1*. The statistical analytical tool used in this work is a one-way repeated ANOVA analysis using IBM SPSS Statistics Software. The confidence level was set to 95% with $\alpha = 0.05$. The Sandwich ELISA assay was the primary tool for evaluating the activity the cat allergen protein (61).

4.2 LITERATURE REVIEW

Domestic cats (*Felis domesticus)* are a popular pet in United Stated homes, but cat allergens are one of the major triggers of asthma worldwide. Cat allergens are particularly prevalent and mobile, 99.9% of homes have measurable levels of cat allergens, even though only 49.1% of homes had either a dog or a cat (6). Cat allergens are adhesive meaning that they stick to clothes and to very small particles that can become aerosolized. The highest levels of cat allergen are found in living rooms (10). The dominant cat allergen, *Fel d 1*, is produced largely in cat saliva and sebaceous glands (11). The protein is of an unknown function in the animal but causes an IgG or IgE reaction in sensitive humans.

Essential oils are volatile and limpid. They are lipid soluble and soluble in organic solvents, having a generally lower density than that of water. Essential oils can be synthesized by plant organs including buds, flowers, leaves, stems, twigs, seeds, fruits, roots, wood, or bark and are stored in secretory cells, cavities, canals, epidermic cells, or glandular trichomes. At present, promising approaches have been reported using essential oils or components thereof in medicinal products for human or veterinary use (62).

Essential oils have several biological properties, (63) such as larvicidal action (64), antioxidant (65), analgesic and anti-inflammatory (66), fungicide (67), and antitumor activity (68). The *in vitro* antimicrobial activity of essential oils has been researched extensively against a variety of microorganisms (69).

There is a long history related to the use of plants in treatment of human diseases (70). For example, licorice (Glycyrrhiza glabra), myrrh (Commiphora species) and poppy capsule latex (Papaversomniferum), have written historic record to be used in 2600 B.C. and these plants are still used in treatments either as a part of drug or as herbal preparations in traditional medicine (71). Traditional use of plants as a therapeutic tool, especially those with ethnopharmacological uses, serve as basis for their use in modern medicine (70). According to a recent analysis 80% of 122 plant-derived drugs are related to their original traditional uses (72).

As a motivation for this work, a patent has been published that supports some evidence that cedar wood oil and hinoki oil are of potential value in deactivating variousallergens. Hinoki oil and cedar wood essential oils are used against one or both of *Der p 1* and *Der f 1* allergens (27).

There is some evidence that essential oils can act as an antimicrobial or antioxidant agent or have a pharmacological effect on various tissue (17). McDonald and Tovey (19) initially reported that several essential oils could be emulsified in low concentrations in the laboratory detergent Tween to form effective acaricides. However, Tween is not available to the general public (19). Their follow-up study (20) shows it possible to make a simple, effective, inexpensive laundry acaricidal wash that eliminates the need for very hot water and also maintains low allergen levels in bedding for longer than normal laundering alone. By using eucalyptus oil, which is a widely available essential oil, with a specific kitchen detergent concentrate, McDonald and Tovey (19) formulated an inexpensive acaricidal wash. Table 4.1 shows that more than 80% of mites were killed after immersion in 0.2% and 0.4% solutions of eucalyptus oil for 30 and 60 minutes.

Table 4.1: **Efficacy of Eucalyptus oil formulations for killing dust mites (20)**

Minutes	**Control**	**5% treatment**	**10% treatment**	**20% treatment**	**40% treatment**
7.5	20	30	35	35	40
15	15	35	30	45	70
30	25	50	50	75	90
60	15	20	70	85	90

We are primarily interested in these phenomena due to a patented technology for allergy abatement in the home called “The CarboNix Triple Phase Treatment”. CarboNix uses jets of air and dry ice powder to freeze dust mites in mattresses and carpet. The jets also loosen the dust triggers, which are then vacuumed away. This work is primarily focused on essential oil in the hope that they will prevent re-infestation and regrowth of cat allergen.

4.3 ENZYME LINKED IMMUNOSORBENT ASSAY TECHNOLOGY

The sandwich ELISA illustrated in Figure 4.1 quantifies antigens between two layers of antibodies (i.e. capture and detection antibody). ELISAs are plate-based assays designed for detecting and quantifying substances such as peptides, proteins, antibodies and hormones (73). Performing an ELISA involves at least one antibody with specificity for a particular antigen. The sample with an unknown amount of antigen is immobilized on a solid support (usually a polystyrene micro titer plate) (73).

After the antigen is immobilized, the detection antibody is added, forming a complex with the antigen. The detection antibody can be covalently linked to an enzyme or can itself be detected by a secondary antibody that is linked to an enzyme through bioconjugation. Between each step, the plate is washed with a mild detergent solution to remove any proteins or antibodies that are not specifically bound. After the final wash step, the plate is developed by adding an enzymatic substrate to produce a visible signal, which indicates the quantity of antigen in the sample (73).

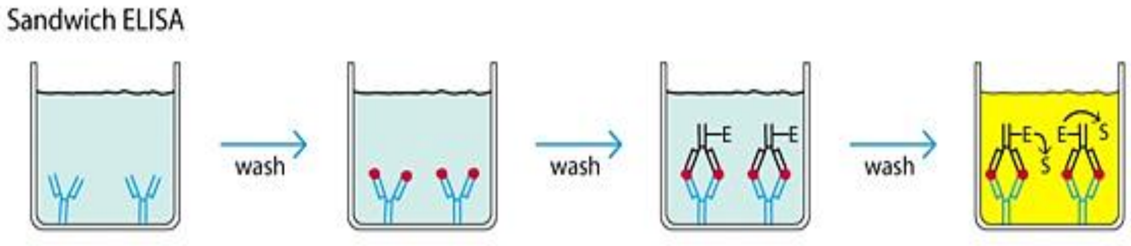

Figure 4.1: **Sandwich ELISA steps (73)**

While ELISA has been one of the primary methods for detecting antigens for over 40 years, the Mutliplex Array for Indoor Allergens (MARIA) has recently been employed by Indoor Biotechnologies for greater sensitivity and reproducibility (74). The MARIA analysis combines Indoor Biotechnologies proprietary panels of monoclonal antibodies with multiplexing technology. MARIA technology uses polystyrene microspheres that are internally dyed with distinct fluorophores to create as many as 100 distinctly coded bead sets. Capture antibodies are covalently coupled to different bead sets and then used to develop quantitative immunoassays using biotinylated detector antibodies and a reporting fluorophore. Up to 11 common allergens can currently be measured simultaneously using this technology (74). According to Indoor Biotechnologies, the typical variability in MARIA assay is quite low. The variability of response in a given sample is generally less than 10% however, results for replicate dust samples can vary as much as 30% because of the variability between dust samples collected in a home.

Preliminary ELISA tests done in the lab show that the highest inactivation resulted at supercritical conditions, where 80% inactivation for *Der p 1* and 37% for *Fel d 1* were observed. Table 4.2 shows that with dry heat treatment only 2.6% *Der p 1* was measured and no deactivation of *Fel d 1* was seen. Because *Der p 1* and *Fel d 1* have different structure and molecular weights, we expected the level of inactivation would be different (11).

Table 4.2: **Percent inactivation of protein, as quantified by ELISA**

CO_2 State	***Der p 1***	***Fel d 1***
Liquid CO_2	5%	2%
Dry Heat	2.6%	None
Supercritical CO_2	80%	37%

The shortcoming with this preliminary data lies in the fact that the allergens were dissolved in water while being exposed to supercritical CO_2. Pillows and mattresses in homes where dust mites live contain allergens bound to dry dust particles. However, the results tell us that the deactivation of the proteins using supercritical CO_2 is promising.

4.4 EVAPORATION RATE OF ESSENTIAL OILS

The evaporation rate for each oil was determined over four days. Each of the dust samples were placed in a vacuum chamber at 30° and then measured each day over four days. Mineral oil was initially used as a control to compare its volatility with that of essential oils. There is no single chemical formula for mineral oil because it is a blend of various hydrocarbons and additives. They are typically light mixtures of alkanes in the C_{15} to C_{40} range. The phase is typically solid when alkanes begin at C_{18}. The masses of each oil/initial mass versus time in hours were plotted, as shown in Figure 4.2. The mass of oil represents the mass of the sample – mass of dry dust. Mineral oil is not volatile and takes a longer time to evaporate. $C_{10}H_{22}$ served better from its low number of carbons, its high volatility, non-polar nature and lack of chemical functionality.

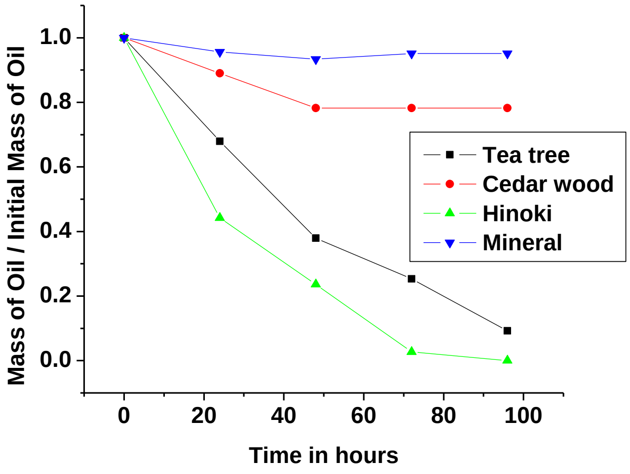

Figure 4.2: **Evaporation rate of essential oils at 30°C with mineral oil as control**

Tables 4.3-4.6 show the four-day evaporation rate for each oil with mineral oil serving as a control.

Table 4.3: **Evaporation rate over four days for mineral oil**

Time in hours	**Mass of sample – Mass of dry dust= mass of oil (mg)**	**Mass of oil / initial mass**
0	0.0932	1.0000
24	0.08912	0.9562
48	0.08890	0.95386
72	0.08869	0.95161
96	0.08869	0.95161

Table 4.4: **Evaporation rate over four days for tea-tree oil**

Time in hours	**Mass of sample – Mass of dry dust= mass of oil (mg)**	**Mass of oil / initial mass**
0	0.1113	1.0000
24	0.0756	0.6792
48	0.0421	0.3791
72	0.0282	0.2531
96	0.0103	0.0923

Tea tree oil $C_{10}H_{18}O$; $\rho = 0.878$ g/mL

Table 4.5: **Evaporation rate over four days for cedar wood oil**

Time in hours	**Mass of sample – Mass of dry dust= mass of oil (mg)**	**Mass of oil / initial mass**
0	0.1110	1.0000
24	0.0979	0.8902
48	0.0861	0.7823
72	0.0861	0.7823
96	0.0861	0.7823

Cedar wood oil $C_{15}H_{24}$; $\rho = 0.952$ g/mL

Table 4.6: **Evaporation rate over four days for hinoki oil**

Time in hours	Mass of sample – Mass of dry dust= mass of oil (mg)	Mass of oil / initial mass
0	1.1087	1.0000
24	0.4904	0.4423
48	0.2614	0.2358
72	0.0301	0.0271
96	0.0000	0.0000

Hinoki oil $C_{10}H_{16}$; ρ=0.8821 g/mL

Tables 4.7-4.10 show the four-day evaporation rate for each oil with n-decane serving as a control.

Table 4.7: **Evaporation rate over four days for n-decane**

Time in hours	Mass of sample – Mass of dry dust= mass of oil (mg)	Mass of oil / initial mass
0	0.0859	1.0000
24	0.0599	0.6973
48	0.0347	0.4039
72	0.0098	0.1141
96	0.000051	0.0059

N-decane $C_{10}H_{22}$; ρ = 0.73005 g/mL

Table 4.8: **Evaporation rate over four days for tea-tree oil**

Time in hours	Mass of sample – Mass of dry dust= mass of oil (mg)	Mass of oil / initial mass
0	0.1116	1.0000
24	0.0811	0.7268
48	0.0535	0.4794
72	0.0251	0.2249
96	0.0082	0.0735

Tea tree oil $C_{10}H_{18}O$; ρ = 0.878 g/mL

Table 4.9: **Evaporation rate over four days for cedar wood oil**

Time in hours	Mass of sample – Mass of dry dust= mass of oil (mg)	Mass of oil / initial mass
0	0.1055	1.0000
24	0.1010	0.9574
48	0.0882	0.8303
72	0.0882	0.8303
96	0.0882	0.8303

Cedar wood oil $C_{15}H_{24}$; $\rho = 0.952$ g/mL

Table 4.10: **Evaporation rate over four days for hinoki oil**

Time in hours	Mass of sample – Mass of dry dust= mass of oil (mg)	Mass of oil / initial mass
0	0.1060	1.000
24	0.0463	0.4368
48	0.0290	0.2736
72	0.0032	0.0302
96	0.0001	0.0009

Hinoki oil $C_{10}H_{16}$; $\rho=0.8821$ g/mL

As shown in Figure 4.3, n-decane's volatility is in between hinoki oil and tea tree oil with cedarwood oil as least volatile. As shown from gas chromatography, the oil volatility agrees.

4.5 PROTOCOL FOR TREATING WET DUST SAMPLES WITH ESSENTIAL OILS

4.5.1 METHOD

Initial analysis of essential oil study began by taking 100 mg of dust from a home. Fine dust particles were isolated using a No. 45 mesh (355 μm) screen to remove large particles and cat hair fibers. 2.0 mL of PBS-T per 100 mg of sample was added to an aliquot with 0.1 mL of oil added to each aliquot. Aliquot 1 was labeled as pure sample of dust with no essential oil added. Aliquot 2 was labeled as cedar wood oil and dust for a total of 2.1 mL. Aliquot 3 was labeled as hinoki oil and dust for a total of 2.1 mL. Aliquot 4 was labeled as tea tree oil and dust for a total of 2.1 mL. Each 2.1 mL / 100 mg mixture was vortexed and placed on a rocker for 2 hours at room temperature and then centrifuged at 2500 rpm for 20 minutes. ELISA analysis was then performed for *Fel d 1* as per the protocol in Appendix Q. Two plate readers were used to compare absorbance values shown in Appendix T.

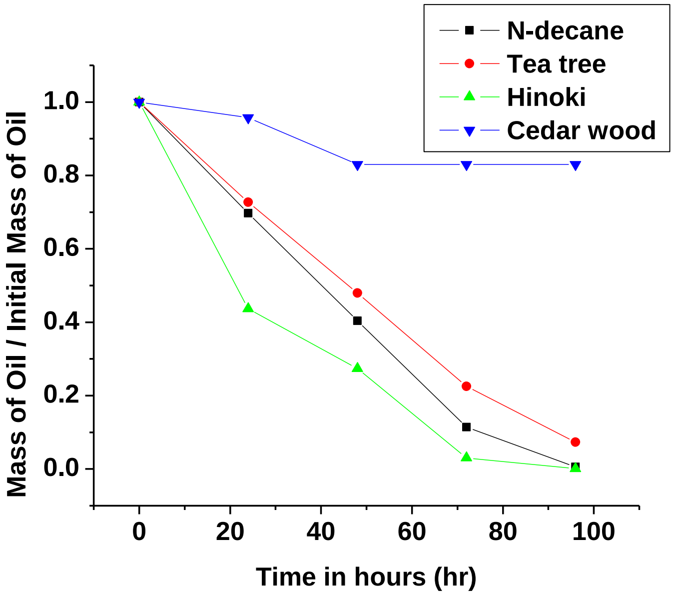

Figure 4.3: **Evaporation rate of essential oils at 30°C with n-decane as control**

A standard curve was developed by plotting the x-axis as the logarithmic scale in ng/mL and the y-axis as linear shown in Figure 4.4. The concentration for *Fel d 1* runs from 100 ng/mL down to 0.2 ng/mL. The absorbance values are on the y-axis. The average absorbance on each blank standard well was determined. This value was subtracted from the well absorbance's to account for any background noise.

Next, the standard curve was determined, shown in Figure 4.4 from the linear region of the absorbance versus log concentration. Concentration was then determined via µg of cat allergen / total grams of dust and then compared.

A second order linear regression was performed on the standard curve and plotted with noise subtracted out.

Table 4.11: **Standard curve data for wet dust sample**

Concentration (ng/m L)	**Log Concentration (ng/m L)**	**Absorbance**
100	2	3.0203
50	1.69897	2.8603
25	1.39794	1.8719
12.5	1.09691	1.0877
6.25	0.79588	0.7361
3.125	0.49485	0.463
1.56	0.193125	0.2649

To get the linear regression curve, only the liner region was plotted from the above data.

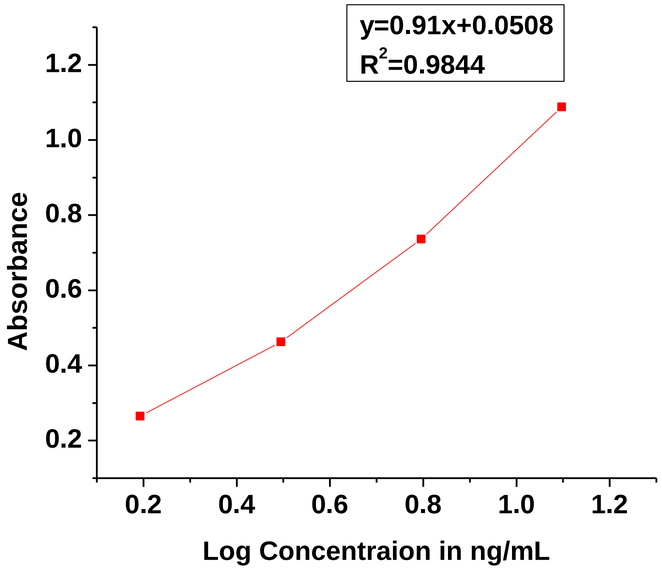

Figure 4.4: **Standard curve for *Fel d 1***

Figure 4.5 shows the 2nd order linear regression curve for the linear portion from the standard curve in Figure 4.4 on *Fel d 1*. The linear regression equation is $y = 0.091x + 0.0508$ with $R^2 = 0.9844$ where y is the dependent variable representing the absorbance and x represents the concentration in ng/mL.

Two plate readers were used to gather results. Both readers correlated well with the results. Figure 4.5 shows the standard curve used to measure the absorbance from Plate Reader 1.

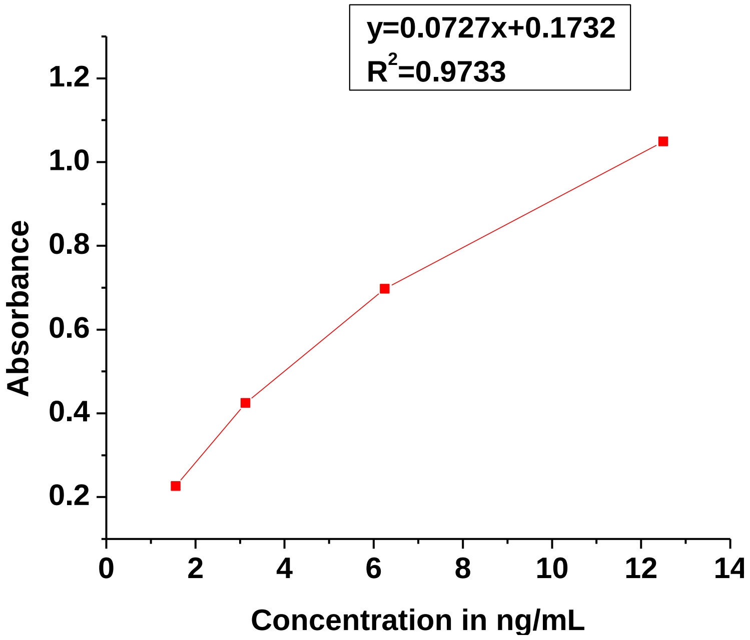

Figure 4.5: **Linear regression on plate reader 1**

The linear regression from the second plate reader is shown in Figure 4.6. The linear regression equation is $y = 0.0717x + 0.0186$ with $R^2=0.971$ where y is the dependent variable representing the absorbance and x represent the concentration in ng/mL.

4.5.6 PROTOCOL FOR TREATING DRY DUST SAMPLES WITH ESSENTIAL OILS

The objective of this work was to analyze the effect of essential oils on the ELISA response of *Fel d 1* and *Der p 1* protein. Prior to the ELISA assay analysis, a “Miele vacuum cleaner” was used to gather dust samples from a home with known cat allergen, following the protocol recommended by the U.S. Department of Housing and Urban Development. (75) Two home rugs were thoroughly vacuumed as dust was collected in filters. Fine dust particles were isolated using a No. 45 mesh (355 um) screen to remove large particles and cat hair fibers. To produce a homogenous sample, all individual collections of fine dust were mixed together. The ELISA response was quantified for 18 dust samples including controls. The treatments included exposure to dry ice temperature, tea tree oil, cedar wood oil, hinoki oil, and n-decane.

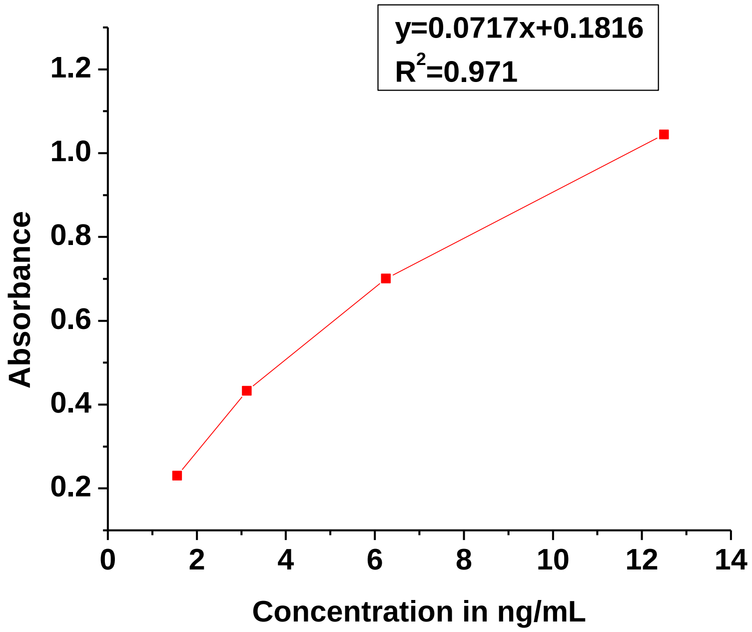

Figure 4.6: **Linear regression on plate reader 2**

Two 300 mg homogenous sample of fine dust were placed in a closed vial and left to sit for 5 days. After 5 days, the vials were then put into a vacuum chamber at 30°C for 7 days to produce a desiccated sample. Six replicates of 100 mg each were treated. Three of the six samples were then exposed to dry ice at -70°C for 5 days and three untreated samples were used as a control.

Similarly, for the essential oil treatment, a homogenous sample of 300 mg of fine dust for each essential oil was placed into a closed vial for 5 days. After 5 days, the vials were desiccated under vacuum at 30°C and 30 psig for 7 days to produce a dry, oil-free sample. Finally, the treated oils were portioned into three 100 mg aliquots for MARIA analysis. Three 100 mg replicates were created for each essential oil with n-decane serving as the negative control.

MARIA analysis was conducted on aqueous extracts by Indoor Biotechnologies. To isolate *Fel d 1* from dust, samples were extracted according to protocols supplied by Indoor Biotechnologies. The extraction procedure was as follows.

Each individual dust aliquot (nominally 100 mg) was extracted by weighing out 100 mg (±5 mg) of fine dust into a 75 mm x 12 mm plastic test tube. Then 2.0 mL of PBS-T (0.05% Tween 20 in phosphate buffered saline) was added to each sample followed by re-suspension using a vortex mixer. The samples were then placed on a laboratory rocker and mixed for 2 hours. Next each sample was centrifuged for 20 minutes at 2,500 rpm. Using a Pasteur pipette, about 1.5 mL of supernatant was removed for ELISA measurement of the antigen. Prior to shipment, aqueous extracts, were stored at -20°C in a freezer vial with each sample labeled and coded. Sample extracts were ultimately analyzed by Indoor Biotechnologies (INDOBIO) via MARIA analysis (76).

4.6 EFFECT OF ESSENTIAL OIL EXPOSURE ON ALLERGENIC PROTEINS ON WET DUST SAMPLES

Table 4.11 and 4.12 show the concentrations of each sample and oil from the two plate readers following application of dilution factor and conversion from ng/mL to µg/g.

Table 4.12: **Effect of essential oil exposure on *Fel d 1* ELISA response (µg of cat allergen / total gram on wet dust sample from plate reader 1**

Sample (µg/g)	Tea tree oil(µg/g)	Cedar wood(µg/g)	Hinoki (µg/g)
3.44	3.92	12.3	10.9
4.57	66.8	23.4	20.7

Table 4.13: **Effect of essential oil exposure on *Fel d 1* ELISA response (µg of cat allergen / total gram on wet dust sample from plate reader 2**

Sample (µg/g)	Tea tree oil(µg/g)	Cedar wood(µg/g)	Hinoki (µg/g)
3.55	3.94	12.3	10.9
4.56	6.72	23.4	20.9

The shortcoming with the above data lie in the fact that cat allergen in homes are typically dry. The dust exposed to essential oil is not typical in a home. There is also high variability within each sample. Essential oils on wet dust samples do nothing to inactivate dust allergenic levels with ELISA measurement. In addition, the response levels are very low, and we cannot conclude that the oils are effective or not.

A home dust sample was sent out to INDOBIO for analysis. Extraction protocol, shown in Appendix L, were performed in lab. The same protocol was followed as above with a sample having no oil added compared to 2.1 mL /100 mg of oil added for three essential oils. Table 4.14 shows the result confirming essential oil on wet dust does nothing to the concentration level of *Fel d 1*.

Table 4.14: **Effect of essential oil exposure on *Fel d 1* ELISA response (µg of cat allergen / total gram on wet dust sample from INDOBIO**

Sample (µg/g)	Tea tree oil(µg/g)	Cedar wood(µg/g)	Hinoki (µg/g)
2.11	4.39	2.13	3.8

4.7 EFFECT OF ESSENTIAL OIL EXPOSURE ON ALLERGENIC PROTIENS ON DRY DUST SAMPLES

A one-way repeated ANOVA test was conducted to compare each essential oil with dry, n-decane and dry ice as controls. The Wilks' Lambda model served as the determinant. The Wilks' Lambda model is a test statistic used in multivariate analysis of variance (MANOVA) which is used todetermine if there are differences between the means of identified groups of subjects on a combination of dependent variables (77).

4.7.1 CASE STUDY 1 FOR ELISA RESPONSE ON *FEL D 1*

Table 4.15 shows the concentration of dust sample in micrograms of *Fel d 1* per gram of dry dust. The mean and standard deviation for each test are shown as well. Exposure to essential oils generally reduced the ELISA concentration response of household dust containing *Fel d 1*.

Table 4.15: **Effect of essential oil exposure on *Fel d 1* ELISA response (ug of cat allergen/total gram of dry sample dust)**

Sample	Dry dust	Dry ice	Tea tree	Hinoki	Cedarwood	N-decane
Sample 1	974.1	649.5	174.9	575.8	103.3	1,181.3
Sample 2	1,098.9	888.8	91.2	282.2	104.9	240.3
Sample 3	1,556.2	1,488.9	84.8	401.4	127.4	327.50
Mean	1,209.7	1,009.1	116.9	419.8	111.9	583.4
Std. Dev.	306.5	432.4	50.3	147.7	13.5	519.7

4.7.2 STATISTICAL ANALYSIS

There is a statistically significant effect on dry dust exposed to tea tree (p=0.031) and cedar wood oil (p=0.023) shown in Table 4.16. Hinoki oil showed a marginal statistical significance (p=0.069). Between each oil, results show statistical significance for tea tree and hinoki oil treatments with a p-value of 0.038. Cedar wood, tea tree and hinoki oils were marginally significant at 0.066 and 0.071. Dry dust samples compared with the samples that were exposed to dry ice sample show no statistical significance. Dry dust samples relative to n-decane also show no statistical significance. Dry ice samples compared with n-decane and hinoki oil show no statistical significance. Dry ice samples compared with tea tree oil, cedar wood and hinoki oil also show no statistical significance.

Table 4.16: **Statistical significance in reduction of *Fel d 1* levels in dry dust for each treatment within subjects**

	Control	**TTO**	**HO**	**CWO**	**DI**	**N-Decane**
Control		0.031	0.069	0.023	0.057	0.14
TTO			0.038	0.066	0.082	0.228
HO				0.071	0.182	0.536
CWO					0.066	0.261
DI						0.485
N-decane						

4.7.3 CASE STUDY 2 FOR ELISA RESPONSE ON *FEL D 1*

In the same home, another study revealed the effect tea tree oil has on *Fel d 1* allergen with n-decane as a control oil. Table 4.17 shows the concentration of dust sample in µg of *Fel d 1* per gram of dry dust. The mean and standard deviation for each test are shown as well. Exposure to essential oils generally reduced the ELISA concentration response of household dust containing *Fel d 1*.

Table 4.17: **Effect of essential oil exposure on *Fel d 1* ELISA response (ug of *Fel d 1*/total gram of dry sample dust)**

Sample	**Dry dust**	**Tea tree**	**N-decane**
Sample 1	1193.9	728.6	779.1
Sample 2	1165.8	1470.1	1555.4
Sample 3	708.3	647.7	1103.9
Mean	1022.7	948.8	1146.1
Std. Dev.	272.6	453.3	389.9

4.7.4 TEA TREE OIL ON *DER F 1* ELISA RESPONSE

Another study showed the effect of tea tree oil on *Der f 1* allergen with n-decane as a control. Table 4.18 shows the concentration of dust sample in µg of *Der f 1* per gram of dry dust. Both mean and standard deviation for each test are shown. Exposure to tea tree oil generally reduced the ELISA concentration response on household dust containing *Der f 1*.

Table 4.18: **Effect of tea tree oil exposure on *Der f 1* ELISA response (ug of *Der f 1*/ total gram of dry sample dust)**

Sample	**Dry dust**	**Tea tree**	**N-decane**
Sample 1	4.134	3.674	3.281
Sample 2	6.771	3.682	6.881
Sample 3	4.434	3.806	4.052
Mean	5.113	3.721	4.738
Std. Dev.	1.179	0.060	1.548

Statistical analysis, shown in Table 4.19, indicates that *Der f 1* was not statistically significant (p=0.167). Future studies would include more sample tests of essential oils on this allergen.

Table 4.19**: Statistical significance in reduction of Der f1 levels in dry dust for each treatment within subject.**

	Control	**TTO**	**N-decane**
Control		0.167	0.207
TTO			0.208
N-decane			

4.8 NEW KNOWLEDGE ON ALLERGENIC PROTEIN DEACTIVATION WITH ESSENTIAL OILS

An attempt has been made to determine whether essential oils, alone, inactivate allergenic proteins on both wet and dry dust samples quantified in µg/total grams of house dust, specifically for cat allergen, *Fel d 1*. The results confirm essential oils do nothing to inactivate allergenic proteins levels on wet dust samples. Although results on dry dust show statistical significance for essential oil treatment, the small sample size as well as a negative result on a second test make the results uninterpretable. More tests with larger sample sizes would be needed to formulate a valid conclusion. This work employed ELISA as the assay to determine inactivation, however other assays would need to be employed to determine if essential oils have a particular role in inactivating allergens.

REFERENCES

1. Akinbami OJ, Moorman JE, Liu X. 2011. *Asthma prevalence, health care use, and mortality: United States, 2005-2009*. US Department of Health and Human Services, Centers for Disease Control and Prevention, National Center for Health Statistics
2. Dhar P, Chan P, Cohen DT, Khawam F, Gibbons S, et al. 2014. Synthesis, antimicrobial evaluation, and structure–activity relationship of α-pinene derivatives. *Journal of agricultural and food chemistry* 62:3548-52
3. (NIAID) NIoAaID. 2001. *Asthma: A concern for Minority Populations, NIAID Fact sheet*. http://www.rightdiagnosis.com/artic/asthma_a_concern_for_minority_populations_niaid_fact_sheet_niaid.htm
4. Rodriquez M.A. W, M.A., Ahn, D., Sundquist, J., Kraemer, H.C. 2002. Identification of population subgroups of children and adolescents with high asthma prevalence: findings from the Third National Health and Nutrition Examination survey. *Arch. Pediatric Adolescence Medicine* 156:269-75
5. Arbes SJ, Cohn RD, Yin M, Muilenberg ML, Burge HA, et al. 2003. House dust mite allergen in US beds: results from the First National Survey of Lead and Allergens in Housing. *Journal of Allergy and Clinical Immunology* 111:408-14
6. Salo PM, Arbes SJ, Jr., Crockett PW, Thorne PS, Cohn RD, Zeldin DC. 2008. Exposure to multiple indoor allergens in US homes and its relationship to asthma. *The Journal of allergy and clinical immunology* 121:678-84 e2
7. National Institute of Health H, Lung and Blood Institute. 2007. Definition, Pathophysiology and Pathogensis of asthma and natural history of asthma.11-34. Number of 11-34 pp.
8. Organization WH. 2011. *What triggers an asthma attack?* http://www.who.int/features/qa/46/en/
9. Tovey ER, Taylor DJ, Mitakakis TZ, De Lucca SD. 2001. Effectiveness of laundry washing agents and conditions in the removal of cat and dust mite allergen from bedding dust. *Journal of allergy and clinical immunology* 108:369-74
10. Kaiser L, Grönlund H, Sandalova T, Ljunggren H-G, van Hage-Hamsten M, et al. 2003. The crystal structure of the major cat allergen Fel d 1, a member of the secretoglobin family. *Journal of Biological Chemistry* 278:37730-5
11. Yu J. 2010. *Inactivation of allergenic proteins by compressed carbon dioxide*, University of South Carolina
12. Kagaku S. 2009. Development of Allergen Denaturing Agents, R&D and Technical Division; Speciality Chemicals Technical Department, Sumika Enviro-Science Co., Ltd.
13. Arlian LG, Bernstein D, Bernstein IL, Friedman S, Grant A, et al. 1992. Prevalence of dust mites in the homes of people with asthma living in eight different geographic areas of the United States. *The Journal of allergy and clinical immunology* 90:292-300

14. Meno K, Thorsted PB, Ipsen H, Kristensen O, Larsen JN, et al. 2005. The crystal structure of recombinant proDer p 1, a major house dust mite proteolytic allergen. *Journal of immunology (Baltimore, Md. : 1950)* 175:3835-45
15. Institute SRE. 2013. *Protein Structures: Primary, Secondary, Tertiary, Quaternary*. http://schoolworkhelper.net/protein-structures-primary-secondary-tertiary-quaternary/
16. Bakkali F, Averbeck S, Averbeck D, Idaomar M. 2008. Biological effects of essential oils – A review. *Food and Chemical Toxicology* 46:446-75
17. Lis-Balchin M. 1997. Essential oils and 'aromatherapy': their modern role in healing. *Journal of the Royal Society of Health* 117:324-9
18. Szelenyi I, Brune K. 2002. Herbal remedies for asthma treatment: between myth and reality. *Drugs Today* 38:265
19. McDonald LG, Tovey E. 1993. The effectiveness of benzyl benzoate and some essential plant oils as laundry additives for killing house dust mites. *Journal of allergy and clinical immunology* 92:771-2
20. Tovey ER, McDonald LG. 1997. A simple washing procedure with eucalyptus oil for controlling house dust mites and their allergens in clothing and bedding. *Journal of allergy and clinical immunology* 100:464-6
21. Hart P, Brand C, Carson C, Riley T, Prager R, Finlay-Jones J. 2000. Terpinen-4-ol, the main component of the essential oil of Melaleuca alternifolia (tea tree oil), suppresses inflammatory mediator production by activated human monocytes. *Inflammation Research* 49:619-26
22. Tranchida PQ, Shellie RA, Purcaro G, Conte LS, Dugo P, et al. 2010. Analysis of fresh and aged tea tree essential oils by using GCxGC-qMS. *Journal of chromatographic science* 48:262-6
23. Carson C, Hammer K, Riley T. 2006. Melaleuca alternifolia (tea tree) oil: a review of antimicrobial and other medicinal properties. *Clinical microbiology reviews* 19:50-62
24. Hammer K, Carson C, Riley T. 2003. Antifungal activity of the components of Melaleuca alternifolia (tea tree) oil. *Journal of Applied Microbiology* 95:853-60
25. Tumen I, Süntar I, Eller FJ, Keleş H, Akkol EK. 2013. Topical wound-healing effects and phytochemical composition of heartwood essential oils of Juniperus virginiana L., Juniperus occidentalis Hook., and Juniperus ashei J. Buchholz. *Journal of medicinal food* 16:48-55
26. Hieda T, Tazaki M, Morishita Y, Aoki T, Nagahama S. 1996. Sesquiterpene alcohols from< i> Chamaecyparis obtusa</i> leaf oil. *Phytochemistry* 42:159-62
27. Suh J, Cornelius G, McKechnie MT, Thompson IA. 2004. Deactivants for dust mite allergens. Google Patents
28. Priestley C, Burgess I, Williamson E. 1998. Effects of essential oils on house dust mites. *Journal of Pharmacy and Pharmacology* 50:193-
29. Williamson EM, Priestley CM, Burgess IF. 2007. An investigation and comparison of the bioactivity of selected essential oils on human lice and house dust mites. *Fitoterapia* 78:521-5
30. Kim K-N, Ko Y-J, Yang H-M, Ham Y-M, Roh SW, et al. 2013. Anti-inflammatory effect of essential oil and its constituents from fingered citron (Citrus medica L. var. sarcodactylis) through blocking JNK, ERK and NF-κB

signaling pathways in LPS-activated RAW 264.7 cells. *Food and Chemical Toxicology* 57:126-31

31. Budisa N, Schulze-Makuch D. 2014. Supercritical carbon dioxide and its potential as a life-sustaining solvent in a planetary environment. *Life* 4:331-40
32. Singh JK, Peterson C. Development and validation of a correlation for exit velocity of water through OP nozzle using CFD simulation. *Proc. THE 4TH INTERNATIONAL MEETING OF ADVANCES IN THERMOFLUIDS (IMAT 2011), 2012*, 1440:216-25: AIP Publishing
33. Karunanidhi SG, Melvinraj C, Sarath Das K, Rao GS. CFD Studies of Combustion in Diesel Engine. *Journal of Engineering Research and Applications (IJERA) ISSN* 2248:9622
34. Anandharamakrishnan C, Gimbun J, Stapley A, Rielly CD. 2009. Application of computational fluid dynamics (CFD) simulations to spray-freezing operations. *Drying Technology* 28:94-102
35. Jackson DP. 2007. *USA Patent No. 7,293,570*
36. Lee JM, Cho MY, Hong CK, Yoon SM, Kim HS, Kim YJ. Effect of Coanda nozzle clearance on the flow characteristics of air amplifier. *Proc. 2014 ISFMFE - 6th International Symposium on Fluid Machinery and Fluid Engineering, 22-25 Oct. 2014, Stevenage, UK, 2014*:083 (6 pp.): IET
37. Blasius H. 1913. Das Ahnlichkeitsgesetz bei Reibungsvorgangen in Flussigkeiten. *Forsch. Arb. Ing.* **134**
38. Cengel Y. 2013. *Heat transfer: a practical approach*. McGraw-Hill Science/Engineering Math
39. Kevin R. Anderson MD, Watit Pakdee, Niveditha Krishnamoorthy. 2013. STAR CCM+ CFD Simulations of Enhanced Heat Transfer in High-Power Density Electronics Using Forced Air Heat Exchanger and Pumped Fluid Loop Cold Plate Fabricated from High Thermal Conductivity Materials. *Journal of Electronics Cooling and Thermal Control* 3

144-54

40. Softwarre SP. 2017. STAR-CCM+ v12.04 User Guide.
41. Salim SM, Cheah S. Wall Y strategy for dealing with wall-bounded turbulent flows. *Proc. Proceedings of the international multiconference of engineers and computer scientists, 2009*, 2: Citeseer
42. Hiltunen K, Jäsberg A, Kallio S, Karema H, Kataja M, et al. 2009. Multiphase flow dynamics. *Theory and Numerics. Tech. Rep* 722
43. Schiller L, and Naumann, A. 1933. *Ueber die grundlegenden Berechnungen bei der Schwerkraftaufbereittung*. pp 318-320.
44. N.I.O.S.A. 2011. Thermophysical Properties of Fluid Systems. In *Technology*
45. 2009. A.I.G., Carbon Dioxide AIGA 068/10 GLOBALLY HARMONISED DOCUMENT. Association
46. Gupta RB, Shim J-J. 2006. *Solubility in supercritical carbon dioxide*. CRC press
47. CARDOZO-FILHO L, WOLFF F, MEIRELES MAA. 1997. HIGH PRESSURE PHASE EQUILIBRIUM: PREDICTION OF ESSENTIAL OIL SOLUBILITY. *Food Science and Technology (Campinas)* 17:485-8

48. Francisco JdC, Sivik B. 2002. Solubility of three monoterpenes, their mixtures and eucalyptus leaf oils in dense carbon dioxide. *The Journal of supercritical fluids* 23:11-9
49. Adams RP. 2007. *Identification of Essential Oil Components by Gas Chromatography/Mass Spectrometry*. Illinois, USA: Allured Publishing Corporation, Carol Stream. 804 pp.
50. Tranchida PQ, Shellie RA, Purcaro G, Conte LS, Dugo P, et al. 2010. Analysis of fresh and aged tea tree essential oils by using GC× GC-qMS. *Journal of chromatographic science* 48:262-6
51. Isman MB. 2000. Plant essential oils for pest and disease management. *Crop protection* 19:603-8
52. Jaoui M, Kleindienst TE, Docherty KS, Lewandowski M, Offenberg JH. 2013. Secondary organic aerosol formation from the oxidation of a series of sesquiterpenes: α-cedrene, β-caryophyllene, α-humulene and α-farnesene with O 3, OH and NO 3 radicals. *Environmental Chemistry* 10:178-93
53. Sousa EM, Chiavone-Filho O, Moreno M, Silva D, Marques M, Meireles M. 2002. Experimental results for the extraction of essential oil from Lippia sidoides Cham. using pressurized carbon dioxide. *Brazilian Journal of chemical engineering* 19:229-41
54. Poling BE, Prausnitz JM, John Paul OC, Reid RC. 2001. *The properties of gases and liquids*. McGraw-Hill New York
55. Fateen S-EK, Khalil MM, Elnabawy AO. 2013. Semi-empirical correlation for binary interaction parameters of the Peng–Robinson equation of state with the van der Waals mixing rules for the prediction of high-pressure vapor–liquid equilibrium. *Journal of advanced research* 4:137-45
56. Iwai Y, Morotomi, T., Sakamoto, K., Koga, Y., & Arai, Y. 1996. High pressure vapor-liquid equilbria for carbon dioxide + Limonene. *Journal of Chemical Engineering Data* 41:951-2
57. Peng JYR, D.B. 1976. A new two-constant equation of state. *Ind. Eng. Chem. Fundam.* 15:59-64
58. McHugh M, Krukonis V. 2013. *Supercritical fluid extraction: principles and practice*. Elsevier
59. White A, Burns D, Christensen TW. 2006. Effective terminal sterilization using supercritical carbon dioxide. *Journal of Biotechnology* 123:504-15
60. Mesut Akgun NAA, Salih Dincer. 1999. Phase behavior of essential oil components in supercritical carbon dioxide. *Journal of Supercritical Fluids* 15:117-25
61. Earle CD, King, E.M., Tsay, A., Pittman, K., Saric, B., Vailes, L., Godbout, R., Oliver, K, Chapman, M. 2007. High-throughput fluorescent multiplex array for indoor allergen exposure assessment. *Journal of Allergy and Clinical Immunology* 119:428-33
62. Franz CM. 2010. Essential oil research: past, present and future. *Flavour and fragrance journal* 25:112-3
63. Chandra D, Kohli G., Prasad K., Bisht, G., Punetha V., Panwar, A., Pande V. 2016. Antimicrobal activity of swertia ciliata, acorous calaus and viola serpens. *World Journal of Pharmaceutical Research* 5:913-24

64. Govindarajan M. 2010. Chemical composition and larvicidal activity of leaf essential oil from Clausena anisata (Willd.) Hook. f. ex Benth (Rutaceae) against three mosquito species. *Asian Pacific Journal of Tropical Medicine* 3:874-7
65. Aidi Wannes W, Mhamdi B, Sriti J, Ben Jemia M, Ouchikh O, et al. 2010. Antioxidant activities of the essential oils and methanol extracts from myrtle (Myrtus communis var. italica L.) leaf, stem and flower. *Food and Chemical Toxicology* 48:1362-70
66. Mendes SS, Bomfim RR, Jesus HCR, Alves PB, Blank AF, et al. 2010. Evaluation of the analgesic and anti-inflammatory effects of the essential oil of Lippia gracilis leaves. *Journal of Ethnopharmacology* 129:391-7
67. Carmo ES, de Oliveira Lima E, de Souza EL. 2008. The potential of Origanum vulgare L. (Lamiaceae) essential oil in inhibiting the growth of some food-related Aspergillus species. *Brazilian Journal of Microbiology* 39:362-7
68. Silva S. L. CJS, Figueiredo P. M. S. and Yano T.,. 2008. Cytoxicc evaluation of essential oil from Casearia sylvestris on huan cancer cells and erythrocytes. *Acta Amazonica* 1:107-12
69. Lopez P. C. SR, Battle and Nerin C.,. 2005. Solid and vapor-phase antimicrobial activities of six essential oils: Susceptibility of selected foodborne bacterial and fungal strains. *Journal of Agricultural Food Chemistry* 53:6939-46
70. Rizvi ZF, Mukhtar R, Chaudhary MF, Zia M. 2013. Antibacterial and antifungal activities of Lawsonia inermis, Lantana camara and Swertia angustifolia. *Pak. J. Bot* 45:275-8
71. Newman DJ, Cragg GM, Snader KM. 2000. The influence of natural products upon drug discovery. *Natural product reports* 17:215-34
72. Fabricant DS, Farnsworth NR. 2001. The value of plants used in traditional medicine for drug discovery. *Environmental health perspectives* 109:69
73. Chakravarthy A. 2011. *ELISA-Enzyme Linked Immunosorbent Assay*. http://exploreable.wordpress.com/2011/05/25/elisa-enzyme-linked-immunosorbent-assay/
74. King EM, Filep S, Smith B, Platts-Mills T, Hamilton RG, et al. 2013. A multi-center ring trial of allergen analysis using fluorescent multiplex array technology. *Journal of immunological methods* 387:89-95
75. Control HOoHHaLH. 2008. Vaccum Dust Sample Collection Protocol For Allergens.
76. Biotechnologies I. 2006. Multiplex Array for Indoor Allergens (MARIA).
77. Carey G. 1998. Multivariate analysis of variance (MANOVA): I. *Theory. Retrieved March* 6:2007

APPENDIX A: GAS CHROMATOGRAM INSTRUCTIONS

1) Turn on the Helium valve.
2) Check to see if the flow rate from the GC or the flow meter is about 20 mL/min.
3) Turn on the following:
    a. Oven temperature to ON position.
    b. Injector A to ON positon.
    c. Det. A to ON positon.
4) Once the above items are ON, turn on the hydrogen and air valves and ignite.
5) Press SIGNAL 1. This should be a high number. This number says that it is ready for an injection and a run.
6) Do a blank run with only a solvent such as ethanol or acetone. Inject and press START.
7) To start up the computer:
    a. Press START
    b. HP CHEMSTATION
    c. INSTRUMENT 1 ONLINE
8) To start a new file:
    a. RUN CONTROL

    - b. SAMPLE INFO
    - c. CHANGE ANY EXISTING FILE NUMBER TO THE NEXT NUMBER
    - d. RUN METHOD
    - e. HIT THE START BUTTON ON THE GC

9) To see the GC graph (Area counts versus Time)
    - a. VIEW
    - b. ONLINE SIGNALS
    - c. SIGNAL 1

10) To change a method
    - a. METHOD
    - b. NEW METHOD
    - c. CREATE A FILENAME
    - d. EDIT ENTIRE METHOD

APPENDIX B: CALIBRATION DATA

Terpinen-4-ol : ρ= 0.933 g/mL at no dilutions.

To make x10 dilution, put 9 mL of EtOH and 1 mL of tea tree oil in a small vial. The density becomes 0.0933 g/mL = 93.3 mg/mL = 93.3 ug/uL

To make x 20 dilution, put 3 mL of EtOH and 3 mL of tea tree oil in a small vial. The density becomes 46.7 ug/uL

To make x 50 dilution, put 4 mL of EtOH with 1 mL of tea tree oil in a small vial. The density becomes 18.7 ug/uL.

To make x100 dilution, put 4.5 mL of EtOH with 0.5 mL of tea tree oil in a small vial. The density becomes 9.33 ug/uL.

To make x1,000 dilution, put 4.5 mL of EtOH with 0.5 mL of tea tree oil in a small vial. The density becomes 0.933 ug/uL.

To make x 10,000 dilution, put 4.5 mL of EtOH with 0.5 mL of tea tree oil in a small vial. The density becomes 0.0933 ug/uL.

To make x 100,000 dilution, put 4.5 mL of EtOH with 0.5 mL of tea tree oil in a small vial. The density becomes 0.00933 ug/uL

α- cedrene ; ρ= 0.932 g/mL at no dilutions

To make x10 dilution, put 9 mL of EtOH and 1 mL of cedar wood oil in a small vial. The density becomes 0.0932 g/mL = 93.2 mg/mL = 93.3 ug/uL

To make x 20 dilution, put 3 mL of EtOH and 3 mL of tea tree oil in a small vial. The density becomes 46.6 ug/uL

To make x 50 dilution, put 4 mL of EtOH with 1 mL of tea tree oil in a small vial. The density becomes 18.7 ug/uL.

To make x100 dilution, put 4.5 mL of EtOH with 0.5 mL of tea tree oil in a small vial. The density becomes 9.32 ug/uL.

To make x1,000 dilution, put 4.5 mL of EtOH with 0.5 mL of tea tree oil in a small vial. The density becomes 0.932 ug/uL.

To make x 10,000 dilution, put 4.5 mL of EtOH with 0.5 mL of tea tree oil in a small vial. The density becomes 0.0932 ug/uL.

To make x 100,000 dilution, put 4.5 mL of EtOH with 0.5 mL of tea tree oil in a small vial. The density becomes 0.00932 ug/uL

α- pinene : ρ = 0.858 g/mL at no dilutions.

To make x10 dilution, put 9 mL of EtOH and 1 mL of tea tree oil in a small vial. The density becomes 0.858 g/mL = 93.3 mg/mL = 85.8 ug/uL

To make x 20 dilution, put 3 mL of EtOH and 3 mL of tea tree oil in a small vial. The density becomes 42.9 ug/uL

To make x 50 dilution, put 4 mL of EtOH with 1 mL of tea tree oil in a small vial. The density becomes 17.2 ug/uL.

To make x100 dilution, put 4.5 mL of EtOH with 0.5 mL of tea tree oil in a small vial. The density becomes 8.58 ug/uL.

To make x1,000 dilution, put 4.5 mL of EtOH with 0.5 mL of tea tree oil in a small vial. The density becomes 0.858 ug/uL.

To make x 10,000 dilution, put 4.5 mL of EtOH with 0.5 mL of tea tree oil in a small vial. The density becomes 0.0858 ug/uL.

To make x 100,000 dilution, put 4.5 mL of EtOH with 0.5 mL of tea tree oil in a small vial. The density becomes 0.00858 ug/uL

APPENDIX C: T_{r1}, P_{r1}, a AND b CONSTANTS AS A FUNCTION OF T AND P IN DETERMINING K_{12} VALUES FOR TERPINEN-4-OL

Table C.1: Design Parameter for 273.15 K

T=298.15 K ;

ρ (g/mL)	P(MPa)	$P_{r1}=\frac{P}{P_c}$
0.2	5.69	**0.7720**
0.7	6.43	**0.8725**

T_{cr1}=304.2 K ; T_{cr2}= 754.3 K ; P_{cr1} = 7.37 MPa ; P_{cr2} = 3.32 MPa ; T_{r1} = 0.980112 ; a_1=402516.985 ; a_2= 10687349.4 ; b_1 = 26.698 ; b_2 = 146.960

Table C.2: Design Parameter for 283.15 K

T = 313.15 K ;

ρ (g/mL)	P(MPa)	$P_{r1}=\frac{P}{P_c}$
0.2	7.03	0.9539
0.3	8.18	1.110
0.4	8.69	1.179
0.6	9.67	1.312
0.7	11.43	1.551

T_{cr1}=304.2 K ; T_{cr2}= 754.3 K ; P_{cr1} = 7.37 MPa ; P_{cr2} = 3.32 MPa ; T_{r1} = 1.029421 ; a_1=388716.133 ; a_2= 10429878.4 ; b_1 = 26.698 ; b_2 = 146.960

Table C.3: Design Parameter for 293.15K

T = 323.15 K

ρ (g/mL)	P(MPa)	$P_{r1}=\frac{P}{P_c}$
0.2	7.63	1.035
0.3	9.18	1.246
0.4	10.12	1.373
0.6	12.26	1.664
0.7	15	2.035

T_{cr1}=304.2 K ; T_{cr2}= 754.3 K ; P_{cr1} = 7.37 MPa ; P_{cr2} = 3.32 MPa ; T_{r1} = 1.062295 ; a_1=379828.561 ; a_2= 10263340.1 ; b_1 = 26.698 ; b_2 = 146.960

Table C.4: Design Parameter for 303.15K

T = 333.15 K

ρ (g/mL)	**P(MPa)**	**$P_{r1}=\frac{P}{P_c}$**
0.2	8.21	1.114
0.3	10.16	1.379
0.4	11.56	1.569
0.6	14.89	2.020
0.7	18.64	2.530

T_{cr1}=304.2 K ; T_{cr2}= 754.3 K ; P_{cr1} = 7.37 MPa ; P_{cr2} = 3.32 MPa ; T_{r1} = 1.095168 ; a_1=371177.896 ;
a_2= 10100668.9 ; b_1 = 26.698 ; b_2 = 146.960

APPENDIX D: T_{r1}, P_{r1}, a AND b CONSTANTS AS A FUNCTION OF T AND P IN DETERMINING K_{12} VALUES FOR α-CEDRENE

Table D.1: Alpha-Cedrene at 298.15 K

T=298.15 K

ρ (g/mL)	**P(MPa)**	**$P_{r1}=\frac{P}{P_c}$**
0.2	5.69	**0.7720**
0.7	6.43	**0.8725**

T_{cr1}=304.2 K ; T_{cr2}= 792.2 K ; P_{cr1} = 7.37 MPa ; P_{cr2} = 2.12 MPa ; T_{r1} = 0.980112 ; a_1=402516.985 ; a_2= 15008896 ; b_1 = 26.698 ; b_2 = 241.708

Table D.2: Alpha-Cedrene at 313.15 K

T = 313.15 K

ρ (g/mL)	**P(MPa)**	**$P_{r1}=\frac{P}{P_c}$**
0.2	7.03	0.9539
0.3	8.18	1.110
0.4	8.69	1.179
0.6	9.67	1.312
0.7	11.43	1.551

; T_{cr1}=304.2 K ; T_{cr2}= 792.2 K ; P_{cr1} = 7.37 MPa ; P_{cr2} = 2.12 MPa ; T_{r1} = 1.029421 ; a_1=388716.133 ; a_2= 14760840.9 ; b_1 = 26.698 ; b_2 = 241.708

Table D.3: Alpha-Cedrene at 323.15 K

T = 323.15 K

ρ (g/mL)	**P(MPa)**	**$P_{r1}=\frac{P}{P_c}$**
0.2	7.63	1.035
0.3	9.18	1.246
0.4	10.12	1.373
0.6	12.26	1.664
0.7	15	2.035

T_{cr1}=304.2 K ; T_{cr2}= 792.2 ; P_{cr1} = 7.37 MPa ; P_{cr2} = 2.12 MPa ; T_{r1} = 1.062295 ; a_1=379828.561 ; a_2= 14599879.7 ; b_1 = 26.698 ; b_2 = 241.708

Table D.4: Alpha-Cedrene at 333.15 K.

T = 333.15 K

ρ (g/mL)	**P(MPa)**	**$P_{r1}=\frac{P}{P_c}$**
0.2	8.21	1.114
0.3	10.16	1.379
0.4	11.56	1.569
0.6	14.89	2.020
0.7	18.64	2.530

T_{cr1}=304.2 K ; T_{cr2}= 792.2 K ; P_{cr1} = 7.37 MPa ; P_{cr2} = 2.12 MPa ; T_{r1} = 1.095168 ; a_1=371177.896 ; a_2= 14442244.7 ; b_1 = 26.698 ; b_2 = 241.708

APPENDIX E: T_{r1}, P_{r1}, a AND b CONSTANTS AS A FUNCTION OF T AND P IN DETERMINING K_{12} VALUES FOR α-PINENE

Table E.1:T=298.15 K

ρ (g/mL)	**P(MPa)**	**$P_{r1}=\frac{P}{P_c}$**
0.2	5.69	**0.7720**
0.7	6.43	**0.8725**

T_{cr1}=304.2 K ; T_{cr2}= 644.0 K ; P_{cr1} = 7.37 MPa ; P_{cr2} = 2.77 MPa ; T_{r1} = 0.980112 ; a_1=402516.985 ; a_2= 7095416.68 ; b_1 = 26.698 ; b_2 = 150.383

Table E.2: T = 313.15 K

ρ (g/mL)	**P(MPa)**	**$P_{r1}=\frac{P}{P_c}$**
0.2	7.03	0.9539
0.3	8.18	1.110
0.4	8.69	1.179
0.6	9.67	1.312
0.7	11.43	1.551

T_{cr1}=304.2 K ; T_{cr2}= 644.0 K ; P_{cr1} = 7.37 MPa ; P_{cr2} = 2.77 MPa ; T_{r1} = 1.029421 ; a_1=388716.133 ; a_2= 6958480.67 ; b_1 = 26.698 ; b_2 = 150.383

Table E.3: T = 323.15 K

ρ (g/mL)	**P(MPa)**	**$P_{r1}=\frac{P}{P_c}$**
0.2	7.63	1.035
0.3	9.18	1.246
0.4	10.12	1.373
0.6	12.26	1.664
0.7	15	2.035

T_{cr1}=304.2 K ; T_{cr2}= 644.0 K ; P_{cr1} = 7.37 MPa ; P_{cr2} = 2.77 MPa ; T_{r1} = 1.062295 ; a_1=379828.561 ; a_2= 6869726.08 ; b_1 = 26.698 ; b_2 = 150.383

Table E.4: T = 333.15 K

ρ (g/mL)	**P(MPa)**	**$P_{r1}=\frac{P}{P_c}$**
0.2	8.21	1.114
0.3	10.16	1.379
0.4	11.56	1.569
0.6	14.89	2.020
0.7	18.64	2.530

T_{cr1}=304.2 K ; T_{cr2}= 644.0 K ; P_{cr1} = 7.37 MPa ; P_{cr2} = 2.77 MPa ; T_{r1} = 1.095168 ; a_1=371177.896 ; a_2= 6782891.07 ; b_1 = 26.698 ; b_2 = 150.383

APPENDIX F: EXPERIMENTAL DATA FOR TERPINEN-4-OL

Extraction Time:180 minutes
Wavelength:290 nm
Ethanol injection: 4000 µL

	Temp ℃	Density g/mL	Absorb.	ug/uL	ug	Grams extracted	Moles extracted	Volume mL	Flow rate mL/min	Moles of CO2	$y_{T\text{-}4\text{-}ol}$ mole frac	std. D Deviation	Max	Min
	25	0.2	0.004	1.71	6857.14	0.0069	0.0000	4.0000	0.0222	0.0843	0.0005	0.001	0.002	0.000
	25	0.7	0.087	41.24	164952.38	0.1650	0.0011	0.8000	0.0044	0.0169	0.0597	0.002	0.062	0.058
	40	0.2	0.005	2.19	8761.90	0.0088	0.0001	0.9000	0.0050	0.0190	0.0030	0.002	0.005	0.001
	40	0.3	0.013	6.00	24000.00	0.0240	0.0002	0.8200	0.0046	0.0173	0.0089	0.002	0.011	0.007
	40	0.4	0.014	6.48	25904.76	0.0259	0.0002	0.2000	0.0011	0.0042	0.0383	0.004	0.042	0.034
	40	0.6	0.027	12.67	50666.67	0.0507	0.0003	0.1700	0.0009	0.0036	0.0840	0.003	0.087	0.081
	40	0.7	0.390	185.52	742095.24	0.7421	0.0048	1.8000	0.0100	0.0379	0.1126	0.027	0.140	0.086
	50	0.2	0.003	1.24	4952.38	0.0050	0.0000	0.3800	0.0021	0.0080	0.0100	0.002	0.012	0.008
	50	0.3	0.032	15.05	60190.48	0.0602	0.0004	0.5500	0.0031	0.0116	0.0326	0.007	0.040	0.026
	50	0.4	0.040	18.86	75428.57	0.0754	0.0005	0.2000	0.0011	0.0042	0.1040	0.090	0.194	0.014
	50	0.6	0.200	95.05	380190.48	0.3802	0.0025	0.6500	0.0036	0.0137	0.1526	0.007	0.160	0.146
	50	0.7	0.653	310.76	1243047.62	1.2430	0.0081	2.0000	0.0111	0.0421	0.1606	0.006	0.167	0.155
Tea tree	50	0.6	0.238	105.45	421818.18	0.4218	0.0027	0.6500	0.0036	0.0137	0.1665	0.030	0.196	0.136
	60	0.2	0.033	15.52	62095.24	0.0621	0.0004	1.7900	0.0099	0.0377	0.0106	0.015	0.026	-0.004
	60	0.3	0.035	16.48	65904.76	0.0659	0.0004	0.3000	0.0017	0.0063	0.0633	0.003	0.066	0.060
	60	0.4	0.011	5.05	20190.48	0.0202	0.0001	0.0500	0.0003	0.0011	0.1105	0.008	0.119	0.103
	60	0.6	0.150	71.24	284952.38	0.2850	0.0018	0.3000	0.0017	0.0063	0.2262	0.021	0.247	0.205
	60	0.7	0.270	128.38	513523.81	0.5135	0.0033	0.5000	0.0028	0.0105	0.2402	0.025	0.265	0.215

APPENDIX G: EXPERIMENTAL DATA FOR α-CEDRENE

Extraction Time:180 minutes
Wavelength:290 nm
Ethanol injection: 4000 μL

	Temp. ℃	Density g/mL	Absorb.	ug/uL	ug	Grams extracted	Moles extracted	Volume mL	Vol. flow mL/min	Moles of CO2	Mole Fraction	STD DEV.	MAX	MIN
	25	0.2	0.035	0.252976	1011.905	0.001012	4.95182E-06	0.27	0.0015	0.005687	0.00087	0.001	0.002	-0.001
	25	0.7	0.064	0.684524	2738.095	0.002738	1.3399E-05	0.05	0.000278	0.001053	0.012563	0.001	0.014	0.011
	40	0.2	0.193	2.604167	10416.67	0.010417	5.09746E-05	0.8	0.004444	0.016851	0.003016	0.002	0.005	0.001
	40	0.3	0.298	4.166667	16666.67	0.016667	8.15594E-05	1.2	0.006667	0.025276	0.003216	0.003	0.006	0.001
	40	0.4	0.529	7.604167	30416.67	0.030417	0.000148846	0.8	0.004444	0.016851	0.008756	0.003	0.012	0.006
	40	0.6	0.533	7.66369	30654.76	0.030655	0.000150011	0.2	0.001111	0.004213	0.034385	0.002	0.036	0.032
	40	0.7	0.826	12.02381	48095.24	0.048095	0.000235357	0.25	0.001389	0.005266	0.042783	0.006	0.049	0.037
	50	0.2	0.044	0.386905	1547.619	0.001548	7.57337E-06	0.1	0.000556	0.002106	0.003583	0.001	0.005	0.003
	50	0.3	0.084	0.982143	3928.571	0.003929	1.92247E-05	0.09	0.0005	0.001896	0.010039	0.007	0.017	0.003
	50	0.4	0.462	6.607143	26428.57	0.026429	0.00012933	0.35	0.001944	0.007372	0.017241	0.003	0.020	0.015
	50	0.6	0.659	9.53869	38154.76	0.038155	0.000186713	0.24	0.001333	0.005055	0.035619	0.001	0.037	0.035
	50	0.7	1.093	15.99702	63988.1	0.063988	0.00031313	0.25	0.001389	0.005266	0.056127	0.002	0.058	0.054
Cedar wood	50	0.6	0.688	9.965774	39863.1	0.039863	0.000195073	0.24	0.001333	0.005055	0.037155	0.002	0.039	0.036
	60	0.2	0.109	1.354167	5416.667	0.005417	2.65068E-05	0.3	0.001667	0.006319	0.004177	0.001	0.005	0.003
	60	0.3	0.132	1.696429	6785.714	0.006786	3.32063E-05	0.1	0.000556	0.002106	0.01552	0.008	0.024	0.008
	60	0.4	0.269	3.735119	14940.48	0.01494	7.31122E-05	0.15	0.000833	0.00316	0.022617	0.006	0.029	0.017
	60	0.6	1.530	22.5	90000	0.09	0.000440421	0.48	0.002667	0.01011	0.041743	0.004	0.046	0.038
	60	0.7	1.400	20.56548	82261.9	0.082262	0.000402554	0.11	0.000611	0.002317	0.148024	0.070	0.218	0.078

APPENDIX H: EXPERIMENTAL DATA FOR α-PINENE

Extraction Time:180 minutes
Wavelength:290 nm
Ethanol injection: 4000 μL

	Temp. ℃	Density g/mL	Absorb.	ug/uL	ug	Grams extracted	Moles extracted	Volume mL	Vol. flow mL/min	Moles of CO2	y2 Mole Fraction	Std.	Max	Min
	25	0.2	0.008	1.451613	5806.452	0.005806	4.26224E-05	0.95	0.005278	0.02001	0.002126	0.001	0.003	0.001
	25	0.7	0.017	2.903226	11612.9	0.011613	8.52448E-05	0.21	0.001167	0.004423	0.018907	0.001	0.020	0.018
	40	0.2	0.007	1.290323	5161.29	0.005161	3.78866E-05	0.51	0.002833	0.010742	0.003514	0.002	0.005	0.002
	40	0.3	0.010	1.774194	7096.774	0.007097	5.20941E-05	0.37	0.002056	0.007793	0.00664	0.007	0.014	0.000
	40	0.4	0.012	2.096774	8387.097	0.008387	6.15657E-05	0.33	0.001833	0.006951	0.008779	0.005	0.014	0.004
	40	0.6	0.013	2.258065	9032.258	0.009032	6.63015E-05	0.15	0.000833	0.00316	0.020553	0.003	0.024	0.017
	40	0.7	0.024	4.032258	16129.03	0.016129	0.000118396	0.23	0.001278	0.004845	0.023856	0.003	0.027	0.021
	50	0.2	0.015	2.580645	10322.58	0.010323	7.57732E-05	0.73	0.004056	0.015376	0.004904	0.004	0.008	0.001
	50	0.3	0.018	3.064516	12258.06	0.012258	8.99807E-05	0.54	0.003	0.011374	0.007849	0.005	0.012	0.003
	50	0.4	0.044	7.258065	29032.26	0.029032	0.000213112	0.52	0.002889	0.010953	0.019086	0.005	0.024	0.014
	50	0.6	0.051	8.387097	33548.39	0.033548	0.000246263	0.35	0.001944	0.007372	0.032325	0.004	0.036	0.028
	50	0.7	0.058	9.516129	38064.52	0.038065	0.000279414	0.3	0.001667	0.006319	0.042345	0.004	0.046	0.039
Hinoki oil	50	0.6	0.038	9.976744	39906.98	0.039907	0.000292938	0.39	0.002167	0.008215	0.034432	0.002	0.036	0.032
	60	0.2	0.016	2.741935	10967.74	0.010968	8.0509E-05	0.65	0.003611	0.013691	0.005846	0.005	0.011	0.001
	60	0.3	0.023	3.870968	15483.87	0.015484	0.00011366	0.3	0.001667	0.006319	0.017669	0.007	0.024	0.011
	60	0.4	0.062	10.16129	40645.16	0.040645	0.000298357	0.45	0.0025	0.009479	0.030517	0.010	0.041	0.020
	60	0.6	0.077	12.58065	50322.58	0.050323	0.000369394	0.29	0.001611	0.006108	0.057025	0.001	0.058	0.056
	60	0.7	0.098	15.96774	63870.97	0.063871	0.000468847	0.3	0.001667	0.006319	0.069071	0.098	0.167	-0.029

Y_2 mole fraction at 50°C and 0.3 g/mL of 0.008 is in agreement with Akgun(45)

APPENDIX I: PENG ROBINSON Y_2 FOR TERPINEN-4-OL @ K_{12}=0.124

T=25°C

P MPa	ρ(g/mL)	X_1	X_2	Φ_1^{liquid}	Φ_1^{vapor}	Φ_2^{liquid}	Φ_2^{vapor}	$K_1=\phi_1^{liquid}/\phi_1^{vapor}$	$K_2=\phi_2^{liquid}/\phi_2^{vapor}$	Y_1	Y_2	Y_1+Y_2
5.69	0.2	0.7	0.3	1.2263	0.7070	1.2e-6	0.0254	1.7345	4.7e-5	1.2142	0.00001	1.2142
6.43	0.7	0.95	0.05	0.7001	0.7086	1.765e-5	1.429e-5	0.9880	1.235	0.9386	0.0618	1.0000

T=40°C

P MPa	ρ(g/mL)	X_1	X_2	Φ_1^{liquid}	Φ_1^{vapor}	Φ_2^{liquid}	Φ_2^{vapor}	$K_1=\phi_1^{liquid}/\phi_1^{vapor}$	$K_2=\phi_2^{liquid}/\phi_2^{vapor}$	Y_1	Y_2	Y_1+Y_2
7.03	0.2	0.70	0.30	1.251	0.6938	3.5e-6	0.0176	1.803	0.0002	1.262	0.0001	1.2611
8.18	0.3	0.80	0.20	0.9269	0.6511	5.5e-6	0.00085	1.424	0.0065	1.139	0.0013	1.1405
8.69	0.4	0.85	0.150	0.8013	0.6506	8.4e-6	8.2e-5	1.232	0.1024	1.047	0.0154	1.0626
9.67	0.6	0.89	0.11	0.6801	0.6474	1.3e-5	2.1e-5	1.051	0.6190	0.9354	0.0681	1.0034
11.4	0.7	0.90	0.10	0.5875	0.6015	1.4 e-5	1.2e-5	0.9767	1.1667	0.8790	0.1167	1.0000

T=50°C

P MPa	ρ(g/mL)	X_1	X_2	Φ_1^{liquid}	Φ_1^{vapor}	Φ_2^{liquid}	Φ_2^{vapor}	$K_1=\phi_1^{liquid}/\phi_1^{vapor}$	$K_2=\phi_2^{liquid}/\phi_2^{vapor}$	Y_1	Y_2	Y_1+Y_2
7.93	0.2	0.75	0.25	1.173	0.6919	8.8e-6	0.0171	1.6953	5.1e-4	1.271	0.0001	1.272
9.18	0.3	0.82	0.18	0.9142	0.6804	1.3e-5	0.0003	1.3436	0.0433	1.1018	0.0078	1.109
10.13	0.4	0.84	0.16	0.8129	0.7273	1.42e-5	3.14e-5	1.117	0.4522	0.938	0.0723	1.010
12.26	0.6	0.85	0.15	0.6886	0.6920	1.5e-5	1.5e-5	0.9951	1.0000	0.8458	0.1500	1.0000
15	0.7	0.86	0.14	0.5541	0.5672	8.02e-6	7.02e-6	0.9769	1.1425	0.8401	0.1599	1.0000

T=60°C

P MPa	**ρ(g/mL)**	**X_1**	**X_2**	**Φ_1^{liquid}**	**Φ_1^{vapor}**	**Φ_2^{liquid}**	**Φ_2^{vapor}**	**$K_1=\phi_1^{liquid}/\phi_1^{vapor}$**	**$K_2=\phi_2^{liquid}/\phi_2^{vapor}$**	**Y_1**	**Y_2**	**Y_1+Y_2**
8.2	0.2	0.70	0.30	1.378	0.715	1.4e-5	0.021	1.927	6.7e-4	1.349	0.0002	1.349
10.2	0.3	0.71	0.29	1.1322	0.7304	1.3e-5	0.0002	1.550	0.0650	1.105	0.0189	1.119
11.6	0.4	0.72	0.28	1.0061	0.7362	1.3e-5	5.4e-5	1.367	0.2407	0.984	0.0674	1.052
14.9	0.6	0.74	0.26	0.8069	0.7631	1.3e-5	1.5e-5	1.057	0.866	0.782	0.2252	1.007
18.6	0.7	0.75	0.25	0.6808	0.67033	1.3e-5	1.4e-5	1.016	0.9286	0.7620	0.2400	1.001

APPENDIX J: PENG ROBINSON Y_2 FOR α-CEDRENE @ K_{12}=0.110

T=25°C

P MPa	ρ(g/mL)	X_1	X_2	Φ_1^{liquid}	Φ_1^{vapor}	Φ_2^{liquid}	Φ_2^{vapor}	$K_1=\phi_1^{liquid}/\phi_1^{vapor}$	$K_2=\phi_2^{liquid}/\phi_2^{vapor}$	Y_1	Y_2	Y_1+Y_2
5.69	0.2	0.65	0.35	0.7485	0.7059	5.1e-5	0.01236	1.060	0.0041	0.6897	0..0014	1.0000
6.43	0.7	0.985	0.015	0.6694	0.6687	7.0e-5	7.6e-5	1.001	0.9211	0.9860	0.0138	1.0000

T=40°C

P MPa	ρ(g/mL)	X_1	X_2	Φ_1^{liquid}	Φ_1^{vapor}	Φ_2^{liquid}	Φ_2^{vapor}	$K_1=\phi_1^{liquid}/\phi_1^{vapor}$	$K_2=\phi_2^{liquid}/\phi_2^{vapor}$	Y_1	Y_2	Y_1+Y_2
7.03	0.2	0.75	0.25	0.9349	0.6938	2.1e-5	0.0087	1.348	0.0024	1.011	0.00001	1.011
8.18	0.3	0.88	0.120	0.7312	0.6454	3.6e-5	0.0016	1.133	0.0225	0.9970	0.0027	1.000
8.69	0.4	0.90	0.100	0.6824	0.6252	4.2e-5	0.0003	1.091	0.1400	0.9819	0.0140	1.000
9.67	0.6	0.94	0.060	0.6035	0.5898	6.5e-5	0.00011	1.023	0.5909	0.9616	0.0355	1.000
11.4	0.7	0.953	0.047	0.5287	0.5269	7.7e-5	8.2e-5	1.003	0.9390	0.9558	0.0441	1.000

T=50°C

P MPa	ρ(g/mL)	X_1	X_2	Φ_1^{liquid}	Φ_1^{vapor}	Φ_2^{liquid}	Φ_2^{vapor}	$K_1=\phi_1^{liquid}/\phi_1^{vapor}$	$K_2=\phi_2^{liquid}/\phi_2^{vapor}$	Y_1	Y_2	Y_1+Y_2
7.93	0.2	0.72	0.28	0.9705	0.6919	3.4e-5	0.0088	1.403	0.0039	1.010	0.0011	1.011
9.18	0.3	0.878	0.122	0.7470	0.6501	6.2e-5	0.0014	1.149	0.0443	1.009	0.0054	1.014
10.13	0.4	0.92	0.08	0.6624	0.6196	9.2e-5	0.00042	1.069	0.2190	0.983	0.0175	1.001
12.26	0.6	0.94	0.06	0.5674	0.5553	0.00011	0.00018	1.004	0.6111	0.9438	0.0367	1.000
15	0.7	0.95	0.05	0.4922	0.4947	0.00013	0.00012	0.9950	1.0833	0.9453	0.0542	1.000

T=60°C

P MPa	ρ(g/mL)	X_1	X_2	Φ_1^{liquid}	Φ_1^{vapor}	Φ_2^{liquid}	Φ_2^{vapor}	$K_1=\phi_1^{liquid}/\phi_1^{vapor}$	$K_2=\phi_2^{liquid}/\phi_2^{vapor}$	Y_1	Y_2	Y_1+Y_2
8.2	0.2	0.75	0.25	1.0220	0.7134	6.1e-5	0.0146	1.433	0.0042	1.075	0.0010	1.075
10.2	0.3	0.85	0.15	0.7846	0.6572	8.7e-5	0.0017	1.194	0.0512	1.015	0.0077	1.023
11.6	0.4	0.92	0.08	0.6613	0.6193	0.00016	0.0006	1.068	0.2667	0.983	0.021	1.004
14.9	0.6	0.94	0.06	0.5512	0.5424	0.00020	0.0003	1.016	0.6667	0.955	0.040	1.000
18.6	0.7	0.96	0.04	0.4757	0.5231	0.0003	9.8e-5	0.909	3.061	0.873	0.1224	1.000

APPENDIX K: PENG ROBINSON Y_2 FOR α-PINENE @k_{12} = 0.110

T=25°C

P MPa	ρ(g/mL)	X_1	X_2	Φ_1^{liquid}	Φ_1^{vapor}	Φ_2^{liquid}	Φ_2^{vapor}	$K_1=\phi_1^{liquid}/\phi_1^{vapor}$	$K_2=\phi_2^{liquid}/\phi_2^{vapor}$	Y_1	Y_2	Y_1+y_2
5.69	0.2	0.600	0.400	1.0520	0.7059	0.00031	0.0604	1.4903	0.00513	0.894	0.0021	1.0000
6.43	0.7	0.988	0.012	0.6679	0.6692	0.0026	0.0023	0.9981	1.1304	0.986	0.0136	1.0000

T=40°C

P MPa	ρ(g/mL)	X_1	X_2	Φ_1^{liquid}	Φ_1^{vapor}	Φ_2^{liquid}	Φ_2^{vapor}	$K_1=\phi_1^{liquid}/\phi_1^{vapor}$	$K_2=\phi_2^{liquid}/\phi_2^{vapor}$	Y_1	Y_2	Y_1+y_2
7.03	0.2	0.750	0.25	0.9279	0.6937	0.0008	0.0508	1.338	0.0157	1.004	0.0040	1.008
8.18	0.3	0.880	0.12	0.7159	0.6459	0.0013	0.0150	1.108	0.0867	0.975	0.0104	1.000
8.69	0.4	0.983	0.017	0.6265	0.6239	0.0052	0.0072	1.004	0.7222	0.9869	0.0123	1.000
9.67	0.6	0.985	0.015	0.5811	0.5822	0.0043	0.0038	0.9981	1.1316	0.9831	0.0170	1.000
11.4	0.7	0.987	0.013	0.5170	0.5189	0.0036	0.0030	0.9963	1.2000	0.9833	0.0156	1.000

T=50°C

P MPa	**ρ(g/mL)**	**X_1**	**X_2**	**Φ_1^{liquid}**	**Φ_1^{vapor}**	**Φ_2^{liquid}**	**Φ_2^{vapor}**	**$K_1=\phi_1^{liquid}/\phi_1^{vapor}$**	**$K_2=\phi_2^{liquid}/\phi_2^{vapor}$**	**Y_1**	**Y_2**	**Y_1+y_2**
7.93	0.2	0.688	0.312	0.9964	0.6918	0.00098	0.0501	1.440	0.0196	0.9907	0.0061	1.000
9.18	0.3	0.878	0.122	0.7284	0.6475	0.0020	0.0212	1.125	0.0943	0.9878	0.0115	1.000
10.13	0.4	0.950	0.050	0.6318	0.6173	0.0041	0.0081	1.023	0.5062	0.9719	0.0253	1.000
12.26	0.6	0.972	0.028	0.5495	0.5507	0.0046	0.0043	0.9978	1.070	0.9699	0.0299	1.000
15	0.7	0.975	0.025	0.4824	0.4861	0.0040	0.0032	0.9924	1.250	0.9676	0.0400	1.000

T=60°

P MPa	**ρ(g/mL)**	**X_1**	**X_2**	**Φ_1^{liquid}**	**Φ_1^{vapor}**	**Φ_2^{liquid}**	**Φ_2^{vapor}**	**$K_1=\phi_1^{liquid}/\phi_1^{vapor}$**	**$K_2=\phi_2^{liquid}/\phi_2^{vapor}$**	**Y_1**	**Y_2**	**Y_1+y_2**
8.2	0.2	0.600	0.400	1.156	0.7133	0.0013	0.0689	1.621	0.0189	0.9726	0.0077	1.000
10.2	0.3	0.750	0.250	0.8497	0.6545	0.0015	0.0207	1.298	0.0725	0.9735	0.0181	1.000
11.6	0.4	0.870	0.130	0.6816	0.6183	0.0026	0.0090	1.102	0.2889	0.9587	0.0376	1.000
14.9	0.6	0.942	0.058	0.5437	0.5433	0.0043	0.0043	1.001	1.000	0.9429	0.0580	1.000
18.6	0.7	0.955	0.045	0.4741	0.4812	0.0044	0.0035	0.9852	1.257	0.9409	0.0600	1.000

APPENDIX L: ISCO-EXTRACTION INSTRUCTIONS

1) All valves should initially be in the CLOSED positon.

2) Preheat the extracted to the desired temperature.

3) Keep the chiller ON overnight.

4) Set the pump to the desired pressure and press the RUN key to start the pump.

5) When you need to refill the pump, open the INLET VLAVE A n the “accel cont” key.

6) Press REFILL. Once cylinder if full close the CO_2 tank.

7) Let pump A pressurize to the desired pressure before opening the pump OUTLET VALVE A.

8) Open the SUPPLY VALVE and allow the chamber pressure to rise to extraction pressure.

9) Once equilibrated, (volume flow rate reaches approximately 0.00 mL/min), open the EXTRACT valve. Supercritical fluid will continually flow through the extraction cartridge and out of the restrictor outlet.

10) Typically, a period of 15-30 minutes is an excellent rule of thumb for supercritical fluid extraction time.

11) <u>DEPRESSURIZING</u>

12) Close both extract and supply valves before opening up the vent valve.

13) Allow the pressure to reach atmospheric pressure before removing the cartridge.

14) Press the STOP key on the controller.

15) OBTAINING THE VOLUME FLOW RATE

16) Set the pump to the desired pressure.

17) Open the supply valve and allow the chamber pressure to rise to the extraction pressure.

   a. Record the initial volume

   b. Record the initial time.

18) Once equilibrated (volume flow rate reaches approximately 0.00 mL/min), Open the EXTRACT valve

   a. Record the volume

   b. Record the time.

19) Rule of thumb for extraction time is 15-30 minutes.

20) Volume flow rate = $\frac{Initial\ Volume - Final\ Volume}{\Delta t}$

APPENDIX M: COOL CLEAN TECHNOLOGIES CHILAIRE PROCESS DESCRIPTION

1) CO_2 gas is provided from a self-regulated CO_2 tank at 300 psi.
2) Clean (<10 ppm water, <1 ppm oil, no particles 10 microns) compressed air is provided at 150 psi, up to 100 cfm.
3) CO_2 and clean dry air (CDA) are supplied to ChilAire Amp.
4) The ChilAire amp contains Two Haskel AAD-5 air amplifiers plumbed in series. These use high pressure air to compress (by action of bidirectional asymmetrical pneumatic cylinders) the CO_2 continuously.
5) The outlet pressure is monitored by a pressure switch which cycles the CO_2 until it reaches 900 psi, at this pressure it will release the CO_2 to a hose leading to the ChilAire fuse.
6) At this point, the CO_2 is at a higher temperature gas due to the compression.
7) The ChilAire Fuse 4000 series contains a R134a refrigeration system which cools a shell and tube heat exchanger.
8) The heated high pressure (900 psi) CO_2 is fed through the shell and tube heat exchanger to cool down to 45°F which is liquid.
9) The liquid is then fed into a manifold while still in the heat exchanger to spread into 4 solenoid valves.

10) Each valve is fed to 0.062” diameter capillary tube which is then split into 2 separate restrictor capillary tubes which range in diameter and length in order to increase or decrease overall mass flow between 80 lb/hour to 160 lb/hour.

11) The 8 capillaries are then connected to 2 meters of 0.03” capillary tubes which is fed through an additional manifold to allow for coaxial air and CO_2 lines.

12) At the end of the coaxial line a Coanda nozzle releases both CO_2 and the CDA.

13) The CDA is released solely to help project the CO_2 more uniformly.

APPENDIX N: OUTLET VELOCITY AT INLET TEMPERATURE OF 0°C

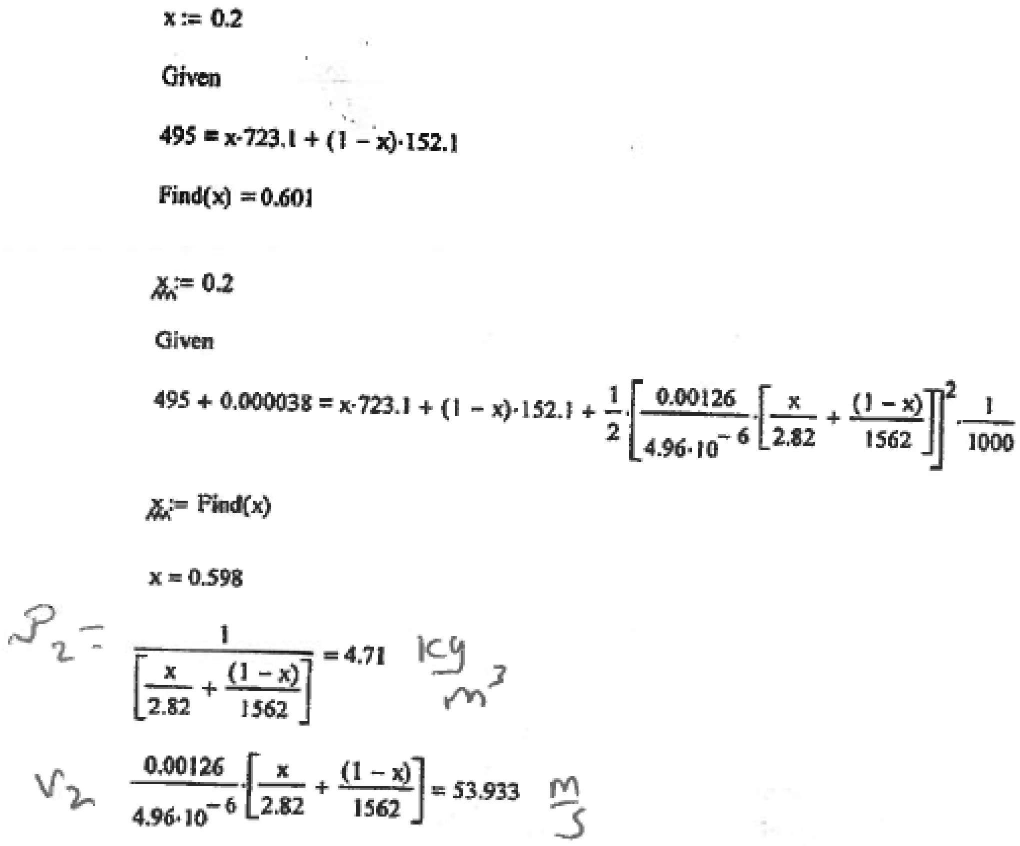

$x := 0.2$

Given

$495 = x\cdot 723.1 + (1 - x)\cdot 152.1$

$\text{Find}(x) = 0.601$

$x := 0.2$

Given

$$495 + 0.000038 = x\cdot 723.1 + (1 - x)\cdot 152.1 + \frac{1}{2}\cdot\left[\frac{0.00126}{4.96\cdot 10^{-6}}\cdot\left[\frac{x}{2.82} + \frac{(1 - x)}{1562}\right]\right]^2\cdot\frac{1}{1000}$$

$x := \text{Find}(x)$

$x = 0.598$

$$\rho_2 = \frac{1}{\left[\frac{x}{2.82} + \frac{(1 - x)}{1562}\right]} = 4.71 \quad \frac{Kg}{m^3}$$

$$V_2 \quad \frac{0.00126}{4.96\cdot 10^{-6}}\cdot\left[\frac{x}{2.82} + \frac{(1 - x)}{1562}\right] = 53.933 \quad \frac{m}{s}$$

APPENDIX O: OUTLET VELOCITY AT INLET TEMPERATURE OF 10°C

$x := 0.2$

Given

$495 = x \cdot 723.1 + (1 - x) \cdot 152.1$

$\mathrm{Find}(x) = 0.601$

$x := 0.2$

Given

$$520.4 + 0.000044 = x \cdot 723.1 + (1 - x) \cdot 152.1 + \frac{1}{2} \cdot \left[\frac{0.00126}{4.96 \cdot 10^{-6}} \cdot \left[\frac{x}{2.82} + \frac{(1 - x)}{1562}\right]\right]^2 \cdot \frac{1}{1000}$$

$x := \mathrm{Find}(x)$

$x = 0.642$

$$\rho_2 = \frac{1}{\left[\frac{x}{2.82} + \frac{(1 - x)}{1562}\right]} = 4.388 \ \frac{kg}{m^3}$$

$$V_2 = \frac{0.00126}{4.96 \cdot 10^{-6}} \cdot \left[\frac{x}{2.82} + \frac{(1 - x)}{1562}\right] = 57.898 \ \frac{m}{s}$$

APPENDIX P: OUTLET VELOCITY AT INLET TEMPERATURE OF 20°C

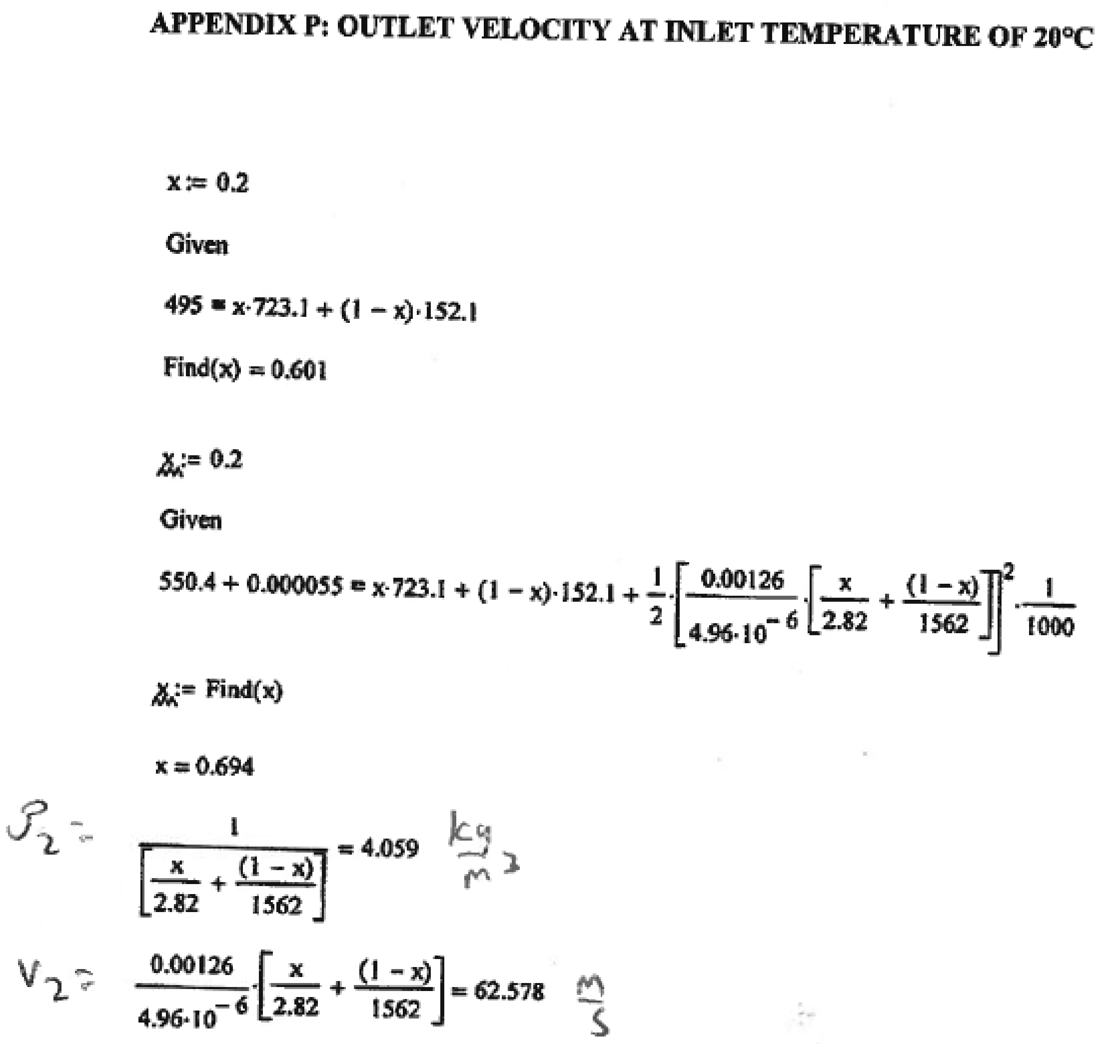

APPENDIX P: OUTLET VELOCITY AT INLET TEMPERATURE OF 20°C

$x := 0.2$

Given

$495 = x \cdot 723.1 + (1 - x) \cdot 152.1$

$\text{Find}(x) = 0.601$

$x := 0.2$

Given

$$550.4 + 0.000055 = x \cdot 723.1 + (1 - x) \cdot 152.1 + \frac{1}{2} \cdot \left[\frac{0.00126}{4.96 \cdot 10^{-6}} \cdot \left[\frac{x}{2.82} + \frac{(1 - x)}{1562} \right] \right]^2 \cdot \frac{1}{1000}$$

$x := \text{Find}(x)$

$x = 0.694$

$$\rho_2 = \frac{1}{\left[\frac{x}{2.82} + \frac{(1 - x)}{1562} \right]} = 4.059 \ \frac{kg}{m^3}$$

$$V_2 = \frac{0.00126}{4.96 \cdot 10^{-6}} \cdot \left[\frac{x}{2.82} + \frac{(1 - x)}{1562} \right] = 62.578 \ \frac{m}{s}$$

APPENDIX Q: OUTLET VELOCITY AT INLET TEMPERATURE OF 30°C

$x := 0.2$

Given

$$495 = x\cdot 723.1 + (1 - x)\cdot 152.1$$

$\text{Find}(x) = 0.601$

$x := 0.2$

Given

$$602.5 + 0.000094 = x\cdot 723.1 + (1 - x)\cdot 152.1 + \frac{1}{2}\cdot\left[\frac{0.00126}{4.96\cdot 10^{-6}}\cdot\left[\frac{x}{2.82} + \frac{(1 - x)}{1562}\right]\right]^{2}\cdot\frac{1}{1000}$$

$x := \text{Find}(x)$

$x = 0.784$

$$\rho_2 = \frac{1}{\left[\frac{x}{2.82} + \frac{(1 - x)}{1562}\right]} = 3.593 \ \frac{\text{kg}}{\text{m}^3}$$

$$V_2 = \frac{0.00126}{4.96\cdot 10^{-6}}\cdot\left[\frac{x}{2.82} + \frac{(1 - x)}{1562}\right] = 70.697 \ \frac{\text{m}}{\text{s}}$$

APPENDIX R: EVAPORATION RATE

Table R.1: Evaporation rate over four days for mineral oil

Time in hours	Mass of sample – Mass of dry dust= mass of oil (mg)	Mass of oil / initial mass
0	0.4500	1.0000
24	0.3922	0.8716
48	0.3675	0.8167
72	0.3655	0.8122
96	0.3569	0.7931

Table R.2: Evaporation rate over four days for tea-tree oil

Time in hours	Mass of sample – Mass of dry dust= mass of oil (mg)	Mass of oil / initial mass
0	0.4500	1.0000
24	0.2755	0.6122
48	0.1761	0.3911
72	0.1455	0.3230
96	0.1425	0.3167

Tea tree oil $C_{10}H_{18}O$; $\rho = 0.878$ g/mL

Table R.3: Evaporation rate over four days for cedar wood oil

Time in hours	Mass of sample – Mass of dry dust= mass of oil (mg)	Mass of oil / initial mass
0	0.4500	1.0000
24	0.3607	0.8016
48	0.2916	0.6480
72	0.2737	0.0682
96	0.2665	0.5922

Hinoki oil $C_{10}H_{16}$; ρ=0.8821 g/mL

Table R.4: Evaporation rate over four days for hinoki oil

Time in hours	Mass of sample – Mass of dry dust= mass of oil (mg)	Mass of oil / initial mass
0	0.4500	1.0000
24	0.2994	0.6653
48	0.2864	0.6364
72	0.2798	0.6218
96	0.2798	0.6218

Hinoki oil $C_{10}H_{16}$; ρ=0.8821 g/mL

APPENDIX S: ELISA PROTOCOL FOR *FEL D 1*

10 uL of antibody mAb 6F9 was mixed with 10 mL of 50 mM carbonate-bicarbonate buffer. Rows A and B were then given 100 uL of this mixture. This was then incubated overnight at 4°C. Each well was then washed 3 times with PBS-0.05% Tween 20 (PBS-T). 100 uL of 1% BSA, PBS-T was then put into each well and incubated at room temperature for 30 minutes. Next, double dilutions of the Universal Allergen Standard (UAS) was used to make a control curve ranging from 100 – 0.2 ng/mL of Fel d 1: 20 uL of UAS was pipetted into 180 uL of 1% BSA, PBS-T into wells A1 and B1 on the ELISA plate. After mixing, 100 uL of this was transferred across the plate into 100 uL of 1% BSA, PBS-T diluent to make 10 serial doubling dilutions. Wells A11, B11, A12 and B12 contained only 1% BSA, PBS-T as blanks. House dust extract samples were added in wells C1, D1, E1 and F1 with 100 uL diluted allergens across the plate. This sat for 1 hour.

Wells were then washed 3 times with PBS-T. 10 uL of biotinylated antibody were mixed with 10 mL of 1% BSA, PBS-T. 100 uL of this mixture was then added to the well plate. This sat for 1 hour at room temperature. Wells were then washed with 3 times with PBS-T. 10 uL of streptavidin-peroxidase were mixed with 10 mL of 1% BSA, PBS-T. 100 uL of this mixture was then added to the well plate and incubated for 30 minutes at room temperature.

Wells were then washed 3 times with PBS-T. 10 uL of H_2O_2 were mixed with 10 mL of 1mM ABTS in 70 mM citrate phosphate buffer. 100 uL of this mixture was then added to the well plate. After 20 minutes, the plate was then read at an absorbance of 405 nm.

APPENDIX T: ELISA PROTOCOL FOR DER P 1

1) Dilute mAb 5H8 1:1000 in 50mM Carbonate-Bicarbonate buffer pH 9.6.
    a. Mix 10 μL mAb 5H8 in 10 mL buffer (adjust as needed) and vortex to mix.
2) Coat wells of polystyrene microtiter (NUNC #439454) with 100μL of mAb mixture pure well.
    a. Number of rows to be determined by experiment but allow rows A and B for standard.
3) Incubate overnight at 4°C.
4) Wash wells 3x with PBS-T.
5) Incubate wells with 100 μL 1% BSA PBS-T for min. 30 min at Room Temperature (RT).
6) Wash wells 3x with PBS-T.
7) Add diluted allergen standard and/or samples to specified wells and incubate for 1 hour at RT.
    a. Standards
        i. Make control curve of standard using doubling dilutions. Use rows A and B for standards.
        ii. Add 180 μL 1%BSA PBS-T in wells A1 and B1.
        iii. Add 100 μL 1% BSA PBS-T in wells 2 – 10 rows A and B.

        iv. Add 200 μL 1% BSA PBS-T in wells 11 and 12 rows A and B (blanks).
        v. Pipet 20 μL of allergen standard (Der p1 2500 ng/mL) into wells A1 and B1. Mix.
        vi. Do doubling dilutions by transferring 100 μL from A1 to A2, followed by 100 μL from A2 to A3, and so forth continuing to A10 and repeating with row B. Mix between each transfer.
        vii. Final concentration of A10 and B10 will ~0.49 ng/mL Der p1.
    b. Samples
        i. Samples typically diluted from 1/10 to 1/80 (adjust as needed).
        ii. Add 180 μL diluents in well 1 and 100 μL in wells 2 – 4 (or further if needed).
        iii. Add 20 μL of sample to well 1 then transfer 100 μL to well 2 resulting in a double dilution.

8) Wash wells 3x with PBS-T.

9) Incubate wells with 100 μL of Biotinylated Anti-group mAb 4C1 (diluted 1:1000 mAb 4C1:1% BSA PBS-T, e.g. 10 μL:10 mL, adjust as needed) for 1 hour at RT.

10) Wash wells 3x with PBS-T.

11) Incubate wells with 100 μL Streptavidin-Peroxidase (diluted 1:1000 0.25 mg/mL S-P in 1% BSA PBS-T) for 30 min at RT.

12) Wash wells 3x with PBS-T.

13) Add 100 μL of 1mM ABTS in 70mM Citrate Phosphate buffer pH 4.2 containing a 1:1000 dilution of 30% H_2O_2. Assay will not develop without addition of H_2O_2.

14) Read the plate at a wavelength of 405 nm and absorbance of highest standard is between 2.0 – 2.4.

    a. Absorbance readings are directly proportional to quantity of Der p1 and values correspond to respective control curves.
    b. To stop the reaction and save the plate, add 100uL of 2mM Sodium Azide.

APPENDIX U: PLATE READER INSTRUCTIONS

1) Manually turn on the “MULTISKAN FC” by THERMO SCIENTIFIC FROM THE back. (There you will find the on-off button)
2) Turn on the laptop and type in password “MMGROUP” (It is not case sensitive)
3) Push the “PLATE IN/OUT” on the scanner and put 96 well plate in. Rows A and B are your standards. Rows C-H are your samples. Place the plate in so that “A1” is shown on the scanner. The lower drawer will automatically open for you.
4) Push the “PLATE IN/OUT” on the scanner to allow the scanner to automatically pull the plate back in. (FYI: You also have the option of opening and closing the plate from within the program on the laptop)
5) On the laptop, there is an icon called “SKANIT FOR MULTISKAN” Click on it.
6) You will be asked for a password but ignore it and press the icon “LOGIN”.
7) On the bottom of the next screen you should see “MULTISKAN FC(196)-357-900976-CONNECTED. This ensures that you are connected.
8) Click “START NEW”. Start a new session.
9) Your protocol should be set to do the following. Photometric, Pause, shake1, platein1, plateout2. This should be under your “protocol” tab. If not, program it.
10) Save your session. Get in the habit of saving your data on a thumb drive.
11) Once you are done, turn off both the scanner and laptop. NEVER LEAVE ON OVERNIGHT

APPENDIX V: ELISA PLATE READER ABSORBANCE

Table V.1: Plate reader 1

Value	1	2	3	4	5	6	7	8	9	10	11	12
A	3.0203	2.8603	1.8719	1.0877	0.7361	0.4630	0.2649	0.2517	0.2159	0.1603	0.0376	0.0396
B	2.9268	1.9777	1.3399	0.7711	0.4850	0.3894	0.2017	0.1998	0.1855	0.1913	0.0407	0.0390
C	2.7325	2.5163	2.7382	2.8493	2.7741	2.1099	1.2027	1.1235	0.7008	0.5370	0.0385	0.0396
D	2.9372	2.6917	3.0472	3.0110	2.7705	2.4589	1.4365	1.2184	0.7416	0.6640	0.0397	0.0383
E	2.7199	3.0769	3.0032	2.9221	2.9811	2.8403	2.1560	2.1948	1.6848	1.6139	0.0399	0.0383
F	3.1109	2.9742	3.2579	3.1409	3.1907	2.8679	2.1098	2.3049	1.8768	1.7857	0.0411	0.0412
G	0.1305	0.1178	0.1207	0.1212	0.1231	0.1141	0.0992	0.1026	0.0951	0.0979	0.0452	0.0383
H	0.1239	0.1230	0.1267	0.1188	0.1272	0.1211	0.0992	0.0951	0.0980	0.1037	0.0372	0.0346

Table V.2: Plater reader 2

	1	**2**	**3**	**4**	**5**	**6**	**7**	**8**	**9**	**10**	**11**	**12**
A	2.977	2.817	1.871	1.078	0.734	0.466	0.264	0.251	0.215	0.16	0.033	0.034
B	2.893	1.975	1.339	0.773	0.489	0.388	0.202	0.2	0.184	0.191	0.035	0.033
C	2.705	2.494	2.724	2.81	2.734	2.098	1.203	1.122	0.701	0.537	0.035	0.036
D	2.885	2.661	3	2.948	2.741	2.441	1.433	1.221	0.741	0.664	0.036	0.033
E	2.69	3.022	2.987	2.88	2.931	2.802	2.147	2.184	1.678	1.606	0.035	0.033
F	3.049	2.927	3.194	3.083	3.143	2.81	2.104	2.29	1.867	1.779	0.036	0.034
G	0.19	0.167	0.176	0.178	0.183	0.166	0.157	0.154	0.14	0.14	0.034	0.033
H	0.18	0.177	0.184	0.17	0.186	0.177	0.152	0.145	0.145	0.158	0.032	0.03

APPENDIX W: INDOOR BIOTECHNOLOGIES DUST SAMPLE EXTRACTION PRODCEDURE

1) SIEVE DUST THROUGH A No.45 mesh screen, 35µm diameter (VWR No. 57332146) to remove large particles and fibers.
2) Weigh 100 mg (±5mg) dust into a 75mm x 12 mm plastic test tube (Sarstedt No. 55.476). If less than 100mg we will take out 10 mg for extraction.
3) Add 2.0 mL PBS-T (0.05% Tween 20 in phosphate buffered saline, pH 7.4) to a sample weighing 100 mg. For samples between 10 mg and 100 mg add the proportional amount needed. The amount in dust in mg is multiplied by 20 to give the appropriate volume of buffer in µL needed. Samples <10 mg are labeled as “Not enough Sample” and not processed.
4) Resuspend using a vortex mixer (Vortex-Genie, Fisher Scientific).
5) Mix end over end for 2 hours on a laboratory rocker (Labquake Shakers, Fisher Scientific, Cat# 13-687-17) at room temperature.
6) Centrifuge 20 minutes at 2,500 rpm 4°C.
7) Remove supernatant (approximately 1.5 mL) with a Pasteur pipette for measurement of antigen. Discard dust pellet
8) Store extract (supernatant) at -20°C in a freezer vial with sample number or relevant code clearly labeled for future analysis of allergen content

APPENDIX X: MASS SAMPLES IN MG SENT TO INBIO ON DRY DUST SAMPLE SET 1

CW=CEDARWOOD; H = HINOKI; DD= DRY DUST D= N-DECANE T= TEA TREE OIL; DI=DRY ICE

Sample	Mass sent to InBio (mg)
CW1	100.0
CW2	104.5
CW3	94.8
H1	105.8
H2	90.5
H3	85.6 (1,172 µL PBS-T)
DD1	77.8 (1,556 µL PBS-T)
DD2	92.9
DD3	99.0
DI1	53.6 (1,072 µL PBST-T)
DI2	103.2
DI3	104.5
T1	78.5 (1,560 µL PBST-T)
T2	95.0
T3	92.2
D1	103.2
D2	90.9
D3	71.6 (1,432 µL PBST-T)

APPENDIX Y: MASS SAMPLES IN MG SENT TO INBIO ON DRY DUST SAMPLE SET 2

DD= N-DECANE; T= TEA TREE OIL; D= DRY DUST SAMPLES

Sample	Mass sent to InBio (mg)
DD1	100
DD2	105.6
DD3	103.5
T1	102.6
T2	105.4
T3	100.6
D1	101.4
D2	97.8
D3	92.7